Properties governing the flow of solution and air through crushed ore for heap leaching

Stefan Robertson

Thesis Presented for the Degree of

DOCTOR OF PHILOSOPHY

Department of Chemical Engineering

UNIVERSITY OF CAPE TOWN

April 2024

Supervisor: Jochen Petersen

Co-supervisor: Petrus van Staden

DECLARATION

I declare that this thesis is my own unaided work, both in concept and execution and that apart from the normal guidance from my supervisors, I received no further assistance. No part of this thesis has been submitted in the past or is being submitted for a degree at this or any other University.

I confirm that I have been granted permission by the University of Cape Town's Doctoral Degrees Board to include the following publications in my PhD thesis, and where co-authorship is involved, my co-authors have agreed that I may include these publications. All the papers were written and published during the time that I was registered for my PhD:

Robertson, S.W., van Staden, P.J., Cherkaev, A., Petersen, J. *'Properties governing the flow of solution through crushed ore for heap leaching'*, Hydrometallurgy 208 (2022) 105811.

Robertson, S.W., Basson, P., van Staden, P.J., Petersen, J. *'Properties governing the flow of solution and air through crushed ore for heap leaching: Part II unsaturated dual-phase flow'*, Hydrometallurgy 215 (2023) 105990.

Robertson, S.W., Basson, P., Brill, S., van Staden, P.J., Petersen, J. '*Properties governing the flow of solution through crushed ore for heap leaching: Part III – Low permeability Ores'*, Hydrometallurgy, 224 (2024) 106247.

ACKNOWLEDGEMENTS

I wish to thank my supervisor Prof Jochen Petersen for his guidance throughout the PhD.

I wish to thank my co-supervisor Dr Petrus van Staden for his mentorship in the field of heap leaching over a period of about 2 decades.

I wish to thank my current manager, Petrus Basson for his encouragement, ideas and mentorship in the field of heap leaching and tank bioleaching over more than a decade.

I wish to thank the current CEO of Mintek, Dr Molefi Motuku, who encouraged me to start the PhD and for Mintek to provide funding, in line with a broader policy of encouraging post-graduate study of Mintek employees.

I wish to thank my father, Guy Trevor Robertson who has been encouraging me to start a PhD for many years now.

I wish to thank Amado Guzman and Hydrogeosense for introducing me to the field of geomechanical laboratory testing.

ABSTRACT

Heap leaching is used extensively for the processing of low-grade copper and gold ores. Heap leaching of low-grade ores is often restricted by the hydrology of the bed, which limits the rate of dissolution of the target mineral. If the ore has low permeability, it may lead to underperformance or even project failure.

Although much research has been published on the flow of solution and air through sand, little has been published on the hydrology of coarser rocks. Physical and hydraulic testing of rocks and agglomerates is often incorporated as a part of heap leach design, however, much still relies on experiential rules. Over the past decade, the author has performed physical and hydraulic testing of a large number of ore samples considered for heap leaching. The tests included uni-axial compression tests, hydrodynamic column tests and leach column tests. The data were reviewed to develop relationships between the hydrology and the physical properties of the ore.

Compressibility of the agglomerates under load was found to increase with silt + clay (-75 µm) content as high contents of silt and clay result in the destruction of porosity under load. The residual moisture held up in the bed after draining under gravity was found to be proportional to the surface area calculated from the PSD, assuming the bed is a collection of spheres. The residual moisture was also proportional to the sand content (-4.75 mm), as a result of the domination of capillary forces over gravity forces at lower particle diameters and smaller interstitial spaces. The pressure drop versus flow relationship during saturated flow was modelled with a modified form of the Carman-Kozeny equation, whereby the particle radius is replaced with a hydraulic radius. The ratio between the experimentally

determined hydraulic radius and the hydraulic radius calculated from the PSD surface area was used to calculate the tortuosity. Since the minimum particle size of the PSD is not exactly known, minimum diameters of 0.002 mm, 0.02 mm and 0.2 mm were used to calculate the PSD surface area. A value of 0.2 mm was found to provide the most physically realistic tortuosity values of between 1.48 and 4.44.

In modelling multi-phase flow, it was found that the hydraulic conductivity function (HCF), relating the hydraulic conductivity to the degree of saturation, can be modelled with traditional capillary models such as Brooks-Corey (BC) and van Genuchten-Mualem (VGM), but only at moisture contents lower than 0.3 m^3/m^3 on average. Furthermore, it was found that the HCF can be modelled as a discontinuous J-curve, with the hydraulic conductivity equal to the saturated hydraulic conductivity (K_s) above the air-entry point, rather than a continuous J-curve with a fitted K_s value, as recommended by other authors. Previous authors have also suggested that the discontinuity represents a transition between capillary- and gravity-controlled flow. However, this author proposes that the discontinuity is caused rather by the presence of “dead voids”, which fill up at higher moisture contents without generating additional flow channels. The point of discontinuity was found to correspond to the air-entry value obtained independently from the air conductivity curves. The experiential rule of a maximum void saturation of 65% for heap aeration appears to correspond on average with the experimental data.

Poor permeability was shown to be caused by a high fines content, resulting in a high steady-state moisture hold-up, which causes the bed to operate close to saturation. The problem of low permeability was addressed by either desliming (removal of the fines by wet screening), or by agglomeration (binding the fines together) with a cementitious binder. Fines removal by desliming was shown to reduce the steady-state moisture hold-up, resulting in the bed operating further away from saturation and increasing the maximum solution application rate. Agglomeration with ordinary Portland Cement modified with additives resulted in fine particles binding together as lumps or coatings onto coarser rocks. These bonds were not destroyed after prolonged exposure to dilute sulphuric acid, due to the pozzolanic properties of the additives (*e.g.* fly ash), which cause cementitious Ca-bonds to be substituted with more stable Al- or Mg-bonds. Agglomeration with cementitious binder was also found to reduce slumping in leach column tests. This resulted in a higher bed porosity, higher limits on the solution application rate and higher copper dissolution rates. Agglomeration with modified cement may therefore provide a novel, cost-effective method for the treatment of low-permeability ores in acid medium (*e.g.* copper, uranium and nickel), since cement agglomeration has only been applied commercially in alkali medium (*e.g.* cyanide solutions for gold ores) to date. Desliming is less attractive due to the high losses of the target metal to the fines.

TABLE OF CONTENTS

LIST OF FIGURES

LIST OF TABLES

ACRONYMS AND ABBREVIATIONS

ACF	Air conductivity function
BC	Brooks-Corey
BSE	Back-scatter detector
CCD	Counter current decantation
DMS	Dense media separation
DRC	Democratic Republic of Congo
EDX	Energy dispersive X-ray detection
ENRC	Eurasian Natural Resources Corporation
HCF	Hydraulic conductivity function
GGBFS	Ground granulated blast furnace slag
GGS	Gates-Gaudin-Schumann
NAC	Net acid consumption
OPC	Ordinary Portland cement
PSD	Particle size distribution
SCM	Supplementary cementitious materials
SEK	Société d'Exploitation de Kipoi
SEM	Scanning electron microscope
TAC	Total acid consumption
XRD	X-ray diffraction analysis
VGM	Van Genuchten-Mualem
WRC	Water retention curve

LIST OF SYMBOLS

A		constant
A	m^2	surface area of column

A_i	m^2/m^3	surface area per unit volume
a		constant
B		constant
B_o		Bond number
b, q		fitting constant
C		constant
C_c		compression coefficient
c_i		is the mass fraction of particles of average diameter d_i.
D_{min}	m	minimum particle diameter
D_{max}	m	maximum particle diameter
D	m	particle diameter
D_c	cm	diameter of the channel
D_p	m	particle diameter for bed of single uniform diameter
d_i	m	particle diameter for bed with range of particle diameters
e		volume voids / volume solids
h	m	capillary head
h_c	m	air entry head
K_a	cm/s	air conductivity
k_a	darcy	air permeability
K_w	cm/s	hydraulic conductivity of solution
K_s	cm/s	saturated hydraulic conductivity
K_r		relative solution conductivity
K_g	cm/s	air conductivity
$K_{g\,max}$	cm/s	maximum air conductivity, air conductivity at residual moisture
l	m	characteristic length
l, m, n, n_p, n_g		fitting constants
M_1, M_2		first and second moments of the particle size distribution
ΔL	m	length of bed
$m_n(D)$	$(kg\ m^{-4})$	*mass distribution function*
n_n (D)	(m^{-4})	size distribution function
$p(D)$	(m^{-1})	mass fraction function
$P(D)$		weight proportion of particles with diameter less than D
ΔP	Pa	pressure drop over bed
Q	m^3/s	volumetric flow through the bed
r_H	m	hydraulic radius
S	m^3/m^3	degree of saturation
S_e		effective saturation
$S_{e\,max}$		effective saturation at air entry point
S_g		relative degree of gaseous saturation
U_i	m/s	interstitial velocity

U_s	m/s	superficial velocity
α		fitting constant
β		particle shape factor
γ		fitting constant
δ	kPa	stress
ε	m^3/m^3	bed porosity, voidage
λ		fitting constants
θ	m^3/m^3	moisture content
θ_r	m^3/m^3	residual moisture content
θ_s	m^3/m^3	saturated moisture content
θ_{aep}	m^3/m^3	air entry point
θ_{max}	m^3/m^3	moisture content at $S_{e\ max}$
μ	kg/m/s	viscosity
ρ	kg/m^3	density
ρ_b	kg/m^3	total loaded bulk density
ρ_s	kg/m^3	solids density
σ	dynes/cm	surface tension
τ		tortuosity

1. INTRODUCTION

Heap leaching accounts for approximately 17% of global gold production and 21% of global copper production (Marsden *et al.*, 2017; Basov, 2015). It is the only economic technology available to extract value metals from low-grade ores; however, the slow rate of recovery is a major drawback, and in most cases is related to heap permeability (Petersen, 2016). In the case of chalcopyrite-containing ores, the refractory nature of the mineral may also lead to slow recovery rates. Heap leaching is commonly applied to recover copper, gold and uranium from low-grade ores. It comprises the stacking of coarsely crushed ore on an impermeable pad and irrigating with a chemical leach solution for an extended period of time to dissolve the target metal(s). The leach solution is applied on the top of the heap with sprinklers or drippers, and trickles through the ore bed through channels and pores. The pregnant leach solution (PLS) is collected from the base of the heap. Advantages include low capital and operational costs, simple design, a rapid construction phase, low energy and water requirements, and fast capital pay-back (Kappes, 2002). It may be applied to large or small operations and can be used in conjunction with a tank leach circuit to provide greater flexibility (John, 2011). A combination of declining ore grades (Figure 1), water supply issues, stricter environmental regulations and perceived investment risks, have resulted in mining companies seeking to reduce costs and increase performance. For large low-grade deposits, such as Haib (Namibia), it is currently uneconomical to treat the ore by milling and flotation, and heap leaching is being considered (Deep South Resources Inc., 2020).

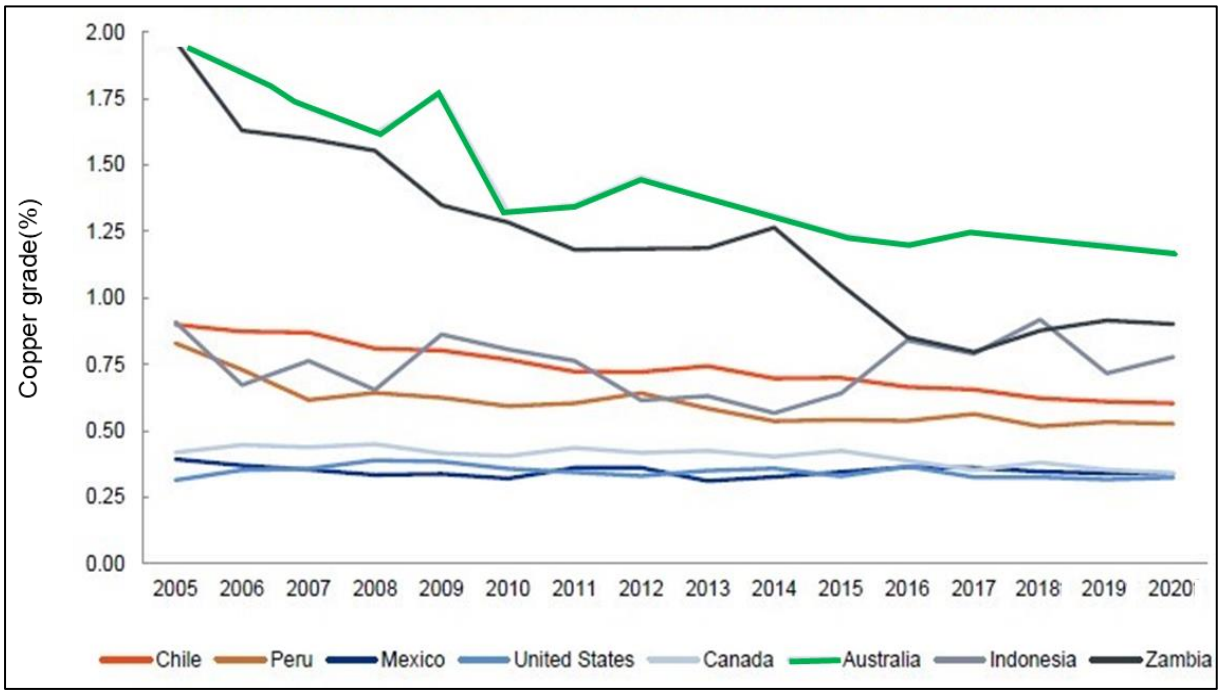

Figure 1. Average copper grades mined by country, 2005-2020 (AME, 2018)

As a result of the above-mentioned factors, heap leaching has experienced impressive growth over the last decades, with precious metal operations benefitting the most from the technology (Figure 2). For example, in 2015 there were 235 active major heap leach operations in the world, as well as 39 projects in development and 133 in evaluation phase (Basov, 2015). In 2014 about 150 major gold / silver mines world-wide used heap leach technology and recovered about 15 million troy ounces of gold (Basov, 2015). This constitutes approximately 17% of global gold production (approximately 89 million troy ounces according to the U.S. Geological Survey data). According to Marsden and Botz (2017), approximately 3.9 million metric tonnes of copper (or 21% of annual production) is from heap leaching. Low-grade ores, waste rock and refractory gold tailings are also a potentially significant revenue stream for both larger and smaller scale companies. Heap leaching has also been applied commercially to gold and silver tailings by utilising an agglomeration binder (Mclelland, 1986).

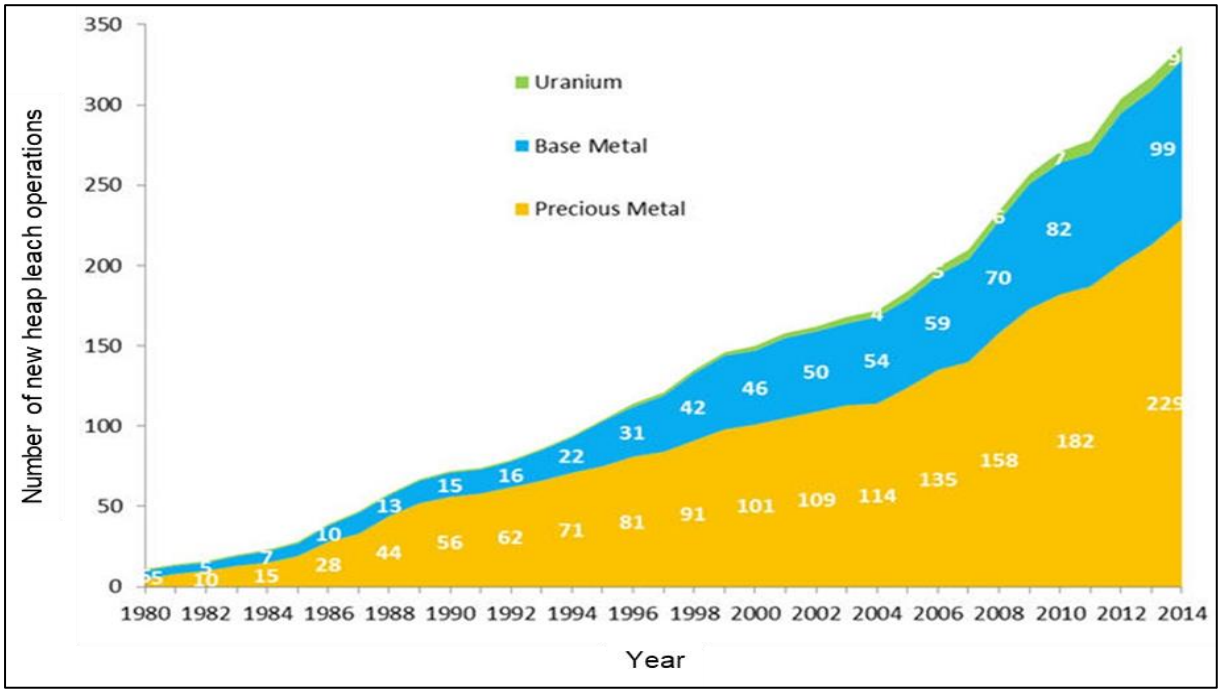

Figure 2. Start-up of currently operating major heap leach mines (Basov, 2015)

The heap hydraulics is often the most important factor that determines the rate of leaching (McBride *et al.*, 2015; Miao *et al*., 2017). Poor solution permeability may limit the rate at which valuable metals can be flushed from the heap, whereas poor solution contact may result in uneven wetting and incomplete extraction, even over extended leach cycles. A relatively high bulk density has been correlated with poorer heap leach performance, combined with segregation and stratification. It has been observed that solution passes through sparsely distributed channels, leaving solids immersed in immobile solution governed by diffusion, and that a portion of the ore could be left without contact with leach solution (van Staden, 2019).

Bouffard and West-Sells (2009) have shown that during scale-up from columns to cribs, high metal recovery was correlated to a low percentage of the solution retained in stagnant form, and that the proportion of stagnant solution was proportional to the percentage fines and the lack of structural support (*e.g.* column walls) in the heap, the latter translating into a higher bed density. Agglomerated material, compared with run-of-mine and crushed ores, was more uniformly sized, with lower bulk density and a lower proportion of stagnant solution. Good solution transport out of the packed bed was attributed to the absence of stagnant zones. Furthermore, certain mineralogical aspects, such as the presence of acid-consuming gangues and clay minerals, may also act as rate-limiting factors in copper heap leaching (Toro *et al.*, 2021).

The need exists for a low-cost process to treat low-grade ores, wastes and small deposits, or deposits in perceived high-risk investment regimes with poor infrastructure (Kappes, 2002). Heap leaching is often used as a low-cost process option for such ores, but in many cases it cannot be applied if the ore has poor solution permeability (Robertson *et al.*, 2013; Lupo, 2011). The presence of clays is a problem in several African heap leach operations, resulting in poor permeability. The problem is currently addressed by screening out fines, resulting in significant metal losses.

Whereas cement may be used as an agglomeration binder to improve permeability in gold (alkaline leach systems), there is currently no such binder (except H_2SO_4) available for commercial use in acidic leach systems. Hence there is a need to develop an acid-resistant binder for use in acidic heap leach systems such as the leaching of copper, nickel laterite and uranium ores. The binder is typically used in an agglomeration step and binds together the fine and coarse particles, creating more void space for solution flow and hence improved solution permeability. Development of such a binder will allow (1) processing of untreatable ores at lower metal losses; (2) higher solids throughput at lower capital and operating costs; (3) lower financial and technical risk; (4) higher metal recovery, and (5) higher revenue flow.

With the depletion of copper oxide resources, the treatment of secondary copper sulphide ores has also become more important (Neira *et al.*, 2021). Such ores typically require the supply of air to the heap as an oxidant, regardless of whether bacterial-assisted leaching or acidic chloride leaching is employed. The supply of air to the heap is often a limiting factor which governs the rate of metal dissolution and can cause poor performance. A better understanding of the fundamentals that govern the supply of air in heaps is necessary to improve the engineering design of the aeration systems to unlock low-grade copper sulphide ores.

Over the years, a number of heap leach projects have experienced problems with poor solution permeability, e.g. Benkala (Whiterow, 2013), Cerro Verde (Galdos *et al.*, 2013) and Chuquicamata (Ramírez *et al.*, 2019). A number of heap leach operations have experienced problems with aeration limitation, such as Terrafame, Finland (Arpalahti and Lundström, 2019); NICICO, Iran (Robertson *et al.*, 2007) and Carlin, Nevada (Logan *et al.*, 2007).

In light of the above, an understanding of the hydrology is essential during heap leach design and it is necessary to perform physical and hydraulic testing of the crushed ores and agglomerates. Physical

and hydraulic test protocols have been developed to measure the amenability of the ores and agglomerates to percolation leaching. These typically include compression tests to determine the bulk density profiles during compaction, as well as hydrodynamic column tests, which measure the moisture hold-up and degree of void saturation as a function of irrigation rate (Keller *et al.*, 2022; Cherkaev, 2019; Scheffel *et al.*, 2016; Pyper *et al.*, 2015; Guzman *et al.*, 2013; Milczarek *et al.*, 2013; Ilankoon, 2012; Ilankoon and Neethling, 2012; Lupo, 2011; Afewu, 2009; Guzman *et al.*, 2008).

Over the past decade, hydraulic and physical tests were performed by the author on a large number of ore samples considered for heap leaching. These tests are reviewed in Chapter 4, and were mostly part of metallurgical test work programmes for mining companies, which included heap leach amenability, pre-feasibility and bankable feasibility test work.

The data was reviewed to evaluate the effect of parameters such as bulk density and particle size distribution (PSD) on the hydraulic and physical properties of the bed. This study aims to provide further insight into the hydrology as it relates to the physical conditions prevailing in the ore bed, such as the porosity, moisture hold-up, bulk density and particle size distribution (PSD). This was done by reviewing models describing the effect of physical properties on the hydraulic conductivity through packed beds, heaps, aggregates and soils. The models were modified and fitted to the range of hydraulic data generated from a large set of samples in order to establish a theoretical basis for further fundamental study of flow through ore piles during heap leaching.

The results are presented in three parts:

- Part I studies the effect of physical properties, including particle size distribution, bulk density and bed porosity on the residual moisture content in the bed after drain-down, as well as on the saturated hydraulic conductivity (K_s). The saturated hydraulic conductivity – pressure drop relationship was modelled with packed bed theory, replacing the particle diameter with a hydraulic radius and using a modified version of the Kozeny-Carman equation. The residual moisture in the bed was explained with the Bond number (B_o), describing the importance of gravitational forces compared to surface tension forces.
- Part II measured the unsaturated and saturated hydraulic conductivity through the bed in hydrodynamic column tests. The data was expressed in terms of the hydraulic conductivity function (HCF), which describes the non-linear relationship of the relative hydraulic conductivity (K_r) and the dimensionless effective saturation (S_e) of the bed. The air conductivity function (ACF), representing the air conductivity (K_g) against the relative degree of gaseous saturation (S_g) was also derived for the hydrodynamic column tests. These relationships are typically modelled with the Brooks-Corey and van Genuchten-Mualem models in traditional soil science, and the aim was to see if these could be applied to coarser rocks and agglomerates in heap leach applications.
- Part III studies the physical properties and hydrodynamics of low-permeability ores, particularly a micaceous copper stockpile material, in order to identify the physical parameters such as high fines content and high moisture hold-up which contribute to poor permeabiltiy. A number of interventions such as desliming and agglomeration with a binder was also tested in order to improve the

permeability of incompetent ores. The effect of these interventions on the hydrodynamics and copper dissolution rates are studied systematically using compression tests, hydrodynamic column tests and, finally, leach column tests.

2. LITERATURE REVIEW

2.1. Physical and hydraulic testing protocols

Although physical and hydraulic testing of porous materials has been studied extensively, direct testing of crushed ores and agglomerates for heap leaching has been reported to a much lesser extent.

Recent advances in hydraulic characterisation of ores for heap leaching has improved the understanding of the physical parameters necessary for heap design. These typically include uni-axial or bi-axial compression tests to determine the change in bulk density as a function of mechanical load (Milczarek *et al.*, 2013; Robertson *et al.*, 2013; Lupo, 2011). Instrumented 1 D column tests were also performed to determine the moisture hold-up profile and degree of saturation as a function of irrigation rate, as well as the residual moisture after drain-down (Afewu, 2009; Guzman *et al.*, 2013; Ilankoon and Neethling, 2013; Cherkaev, 2019; Ilankoon, 2021). Although heaps are intended to operate under unsaturated conditions, the saturated hydraulic conductivity (K_s) is also measured to indicate the combination of compression and irrigation rate at which the bed will become saturated (Guzman *et al.*, 2008; Pyper *et al.*, 2015).

Milczerak *et al.* (2013) performed bi-axial compression tests and saturated hydraulic conductivity measurements on agglomerates with a crush size of 100% - 25 mm. He correlated K_s to the percentage -150 µm material of the post-leach PSD using a power law relationship. He also correlated K_s to a PSD indicator (defined as the ratio of >0.6 mm material to < 0.15 mm material) of the pre-leach PSD. Keller *et al.* (2022) recommended a PSD indicator of >4 (ratio of mass percentage +4.75 mm to -0.15 mm material) for an ore blend ratio to have sufficient permeability.

Milzcerak *et al.*, (2013) found that relative changes in bulk density during compression was most pronounced in well-graded samples (*i.e*. which have a good representation of all grain sizes). Poorly graded (*i.e.* the soil grains are approximately of the same size) showed the least consolidation. He did not find a good correlation between K_s and surface area (A_i) as calculated by equation (1) below, where ρ_s is the particle density and c_i is the mass fraction of particles of average diameter d_i. It is possible that this may be related to the difficulty in accurately quantifying the lowest average diameter, d_i, when solving equation 1, as the lowest d_i typically specified in such a case is the lowest laboratory screen used. Furthermore, the formula in equation 1 is an approximation of the integral, described more completely in section 2.3.

$$A_i = \frac{6}{\rho_s}\sum\frac{c_i}{d_i} \quad (1)$$

Guzman *et al.* 2008 found K_s to decrease with increasing bulk density according to a power law, with exponents of between -4 and -12.

Cherkaev (2019) observed a strong dependency between residual liquid content and PSD under low irrigation flow rates. It was proposed that variation in liquid hold-up can be accounted for by assuming the solution encircles all ore particles, except for ultra-fines that either remain attached to larger particles or are suspended in the liquid phase. Thus, for the major portion of the ore mass, the liquid content must be proportional to the total area of solids in the packing, calculated from a Gates-Gaudin-Schumann fit. Assuming the bed is comprised of spheres, he calculated PSD surface areas for minimum particle diameters (D_{min}) of 0.13 mm, 0.27 mm and 0.53 mm, with 0.27 mm providing the best fit. The experimental results provided good agreement with this hypothesis, and it was further validated with data from literature and industry. It was proposed that a wide pore in the solid matrix would generally conduct the liquid with ease but will not be able to retain a high liquid content due to relatively low capillary force. In contrast, a narrow pore would retain more liquid, but has lower hydraulic conductivity near saturation.

Ilankoon and Neethling (2013) found the residual moisture content to increase with decreasing mean particle diameter; however, their experiments were limited to +4 mm particles and therefore do not accurately represent a heap leach scenario.

A summary of heap leach design criteria proposed by various authors is provided in Table 1.

Scheffel (2017) recommends that the ore should not have more than 10% to 14% -150 µm material and not more than 40% -5 mm material to be suitable for heap leaching. The change in bulk density exerted by the weight of the ore at the bottom of a pile, stacked to a specified height, is commonly measured. At a compression equivalent to the maximum stacking height, the ore bed should maintain a bulk density of below 1.9 t/m^3 (equivalent to a porosity greater than 0.3 m^3/m^3) for the bed to maintain sufficient void volume for solution to flow (Guzman *et al.*, 2013; Milczarek *et al.*, 2013; Robertson *et al.*, 2013; Lupo, 2011; Guzman *et al.*, 2008; Garcia and Jorgensen, 1997). Higher compactions will result in insufficient voidage available for solution flow, resulting in ponding or channelling.

The saturated hydraulic conductivity (K_s) should be at least 100 x the target “unsaturated” application rate for the sample to be suitable for percolation leaching *e.g.* 1000 L/m^2/h for a nominal “unsaturated” application rate of 10 L/m^2/h (Keller *et al.*, 2022; Pyper *et al.,* 2015; Robertson *et al.*, 2013; Guzman *et al.*, 2013; Milczarek *et al.*, 2012; Guzman *et al.*, 2008). For aerated heaps the bed should have an air permeability of at least 100 darcys (Milczarek *et al.*, 2013) and the degree of void saturation during percolation should not exceed 60% to 65%, above which the heaps will not conduct air (Guzman, 2012; Milczarek *et al.*, 2013). For non-aerated heaps, the degree of saturation should not exceed 85% to maintain slope stability (Robertson *et al.*, 2013; Milczarek *et al.*, 2012).

Due to changes that occur in the bed because of fines generation from decrepitation and precipitation, it is further recommended that hydraulic and physical testing be extended to include both feed agglomerates and column leach residues. It is also essential that a particle size distribution be performed in conjunction with the hydraulic characterisation. In order to minimise changes in the

structure of the residues, the author used a method whereby the residues are removed wet from the column, and then transferred directly to the hydrodynamic column or compression cell. The wet residue may then be further compacted by hammering with a rubber mallet on the side of the column or cell.

Table 1. Heap leach design criteria

Parameter	Units	Target Value	Source
Bulk density (ρ)	t/m^3	< 1.9 (dry basis)	Robertson *et al.,* 2013
Bed porosity (ε)	m^3/m^3	> 0.3	Robertson *et al.,* 2013 Guzman *et al.*, 2013
Saturated hydraulic conductivity (K_s)	L/m^2/h	> 100 × target irrigation rate, *i.e.* > 1000 L/m^2/h for a nominal irrigation rate of 10 L/m^2/h	Robertson *et al.,* 2013 Milczerak *et al.*, 2013
Saturated hydraulic conductivity (K_s)	L/m^2/h	> 1000 L/m^2/h for non-clay ores, > 10 000 L/m^2/h for high clay ores	Pyper *et al.*, 2015
Mobile : immobile moisture	w/w	1 : 5 to 1 : 10	Bouffard and Dixon, 2001
Moisture drained from saturation : residual moisture	w/w	1 : 1	Robertson *et al.,* 2013
Air conductivity (K_a)	cm/s	> 10^{-3}	Guzman *et al.*, 2013
Air permeability (k_a)	darcy	> 100	Milczerak *et al.*, 2013
Degree of saturation at target application rate	%	< 60% to 65% for aerated heaps, < 85% for non-aerated heaps	Robertson *et al.,* 2013 Milczerak *et al.*, 2012
PSD criteria		< 10% to 14% -150 µm < 40% -5 mm	Scheffel, 2017
PSD criteria		< 10% to 15% -75 µm	Garcia and Jorgensen, 1997

2.2. Packed bed models

Lizama (2009) proposes that an aerated, percolating column charged with ore is analogous to a packed bed tower reactor. Ergun (1949) derived the following pressure drop equation for packed beds, which includes a viscous and a kinetic energy loss term, where D_c is the diameter of the channel, r_H is the hydraulic radius, U_i is the interstitial velocity, ρ is the density of the liquid, μ is the dynamic viscosity of the liquid, ΔP is the pressure drop over the bed, and ΔL is the length of the bed:

$$\frac{\Delta P}{\Delta L} = \frac{32\mu U_i}{D_c^2} + \frac{1}{2}\frac{\rho {U_i}^2}{D_c} = \frac{2\mu U_i}{r_H^2} + \frac{1}{8}\frac{\rho {U_i}^2}{r_H} \quad (2)$$

Ergun's model describes the bed as a combination of cylindrical channels with a combined volume equal to the total bed porosity available for solution flow. The hydraulic radius is defined as the ratio of the total volume fraction available for flow (ε) divided by the exposed surface area (A_i):

$$r_H = \frac{\varepsilon}{A_i} \quad (3)$$

For heap leach applications, where low Reynolds numbers prevail, the second order term of the velocity becomes negligibly small and the Ergun equation reduces to the Carman-Kozeny equation (Carman, 1937):

$$\frac{\Delta P}{\Delta L} = \frac{2\mu U_i}{r_H^2} = \frac{2\mu U_i A_i^2}{\varepsilon^2} \tag{4}$$

The Ergun equation (2) and the Carman-Kozeny equation (4) have been applied extensively to packed beds of single diameter spheres (and other packing shapes). However, application to beds of crushed ore containing particles with a range of shapes and sizes has been limited.

McDonald *et al.* (1991) derived a modified form of the Carman-Kozeny equation for a bed comprising a range of spherical particle sizes by replacing the hydraulic radius with terms related to the PSD, where U_s is the superficial velocity, $ß$ is a particle shape factor (typically 2-3), τ is the tortuosity (typically 1.44 to 2; Clennel, 1997), and M_1 and M_2 are the first and second moments of the particle size distribution, respectively:

$$\frac{\Delta P}{\Delta L} = \beta\, \tau^2 \mu \frac{(1-\varepsilon)^2}{\varepsilon^3} \left(\frac{M_1}{M_2}\right)^2 U_s \tag{5}$$

The pressure drop –flow relationship is also expressed with Darcy's equation (6), where Q is the volumetric flowrate and A the cross-sectional surface area. $\Delta P/\Delta L$ is eliminated by equating Darcy's equation (6) with the Carman-Kozeny equation (4), and Q/A is replaced by U_i from equation (7) to obtain equation 8. U_i cancels out, ε/A_i is replaced by r_H, and 8 is rearranged to obtain equation (9) relating the hydraulic radius to the saturated hydraulic conductivity (K_s).

$$\frac{\Delta P}{\Delta L} = \frac{\rho g}{K_s}\frac{Q}{A} = \frac{\rho g}{K_s}\frac{U_i}{\tau^2}\varepsilon \tag{6}$$

$$U_i = \frac{Q}{A}\frac{\tau^2}{\varepsilon} \tag{7}$$

$$\frac{\Delta P}{\Delta L} = \frac{\rho g}{K_s}\frac{U_i}{\tau^2}\varepsilon = \frac{2\mu U_i A_i^2}{\varepsilon^2} \tag{8}$$

$$r_H = \tau\sqrt{\frac{K_s 2\mu}{\rho g \varepsilon}} \tag{9}$$

2.3. Determination of surface area

Since the particles are coarse, traditional adsorption-based methods such as Brunauer-Emmet-Teller (BET) could not be applied. Ghasemi and Cwirzen (2017) found good agreement between surface areas measured by the Blaine test and calculated using a spherical approximation for a number of materials, including cement (CEM III / B 42.5 N), marble, limestone and quartz. However, these measurements were also limited to fine materials.

For a particle size distribution comprising spheres of different diameters, the total surface area per unit volume, A_i (m^{-1}), can be calculated from the size distribution function, $n_n(D)$, which is defined such that

$n_n(D)\,dD$ is the total number of particles per unit volume with sizes in the domain [D, $D+dD$] (Zender, 2017):

$$A_i = \int_0^\infty \pi D^2\, n_n(D) dD \tag{10}$$

The mass of particles per unit volume in the domain [D, $D+dD$] is defined by $m_n(D)\,dD$ (kg m^{-3}) and ρ_s (kg m^{-3}) is the true solids density (assumed constant):

$$m_n(\mathrm{D})\mathrm{dD} = \frac{\pi D^3}{6}\rho_s\, n_n(D) dD \tag{11}$$

The dimensionless mass fraction of all the particles that occur in the domain [$D+dD$], is defined by $p(D)\,dD$, where ρ_b (kg/m^3) is the total loaded bulk density, $p(D)$ has dimensions (m^{-1}), and ρ_s (kg m^{-3}) is the solids density:

$$\mathrm{p(D)dD} = \frac{\frac{\pi D^3}{6}\rho_s\, n_n(D) dD}{\rho_b} \tag{12}$$

Re-arranging:

$$n_n(\mathrm{D}) = \frac{p(D)\rho_b}{\frac{\pi}{6}\rho_s D^3} = \frac{6}{\pi}(1-\varepsilon)\frac{p(D)}{D^3} \tag{13}$$

Substituting (13) into (10), re-arranging, and recognising that $\rho_b/\rho_s = (1-\varepsilon)$, yields the following expression for the surface area per unit volume:

$$A_i = 6(1-\varepsilon)\int_0^\infty \frac{p(D)}{D} dD \tag{14}$$

In the context of heap leaching, particle size distributions are often represented by the Gates-Gaudin-Schumann (GGS) distribution (*e.g.* Cherkaev, 2019), where D_{max} is the top-size of the particles, λ is the distribution parameter and $P(D)$ denotes the weight proportion of particles with a size less than D:

$$\mathrm{P(D)} = \left(\frac{D}{D_{max}}\right)^{\lambda} = a(D)^{\lambda} \tag{15}$$

$$\mathrm{p(D)} = \frac{dP(D)}{dD} = \lambda\, a(D)^{\lambda-1} \tag{16a}$$

Substituting equation 16a into equation 14, the surface area may be calculated as follows from the GGS distribution, where D_{min} is the minimum particle size:

$$A_i = 6(1-\varepsilon)\left[\frac{a\lambda D^{\lambda-1}}{\lambda-1}\right]_{D_{min}}^{D_{max}} \tag{16b}$$

Alternatively, the function $P(D)$ may be represented by a second order polynomial, where A, B and C are constants:

$$\mathrm{P(D)} = A(D)^2 + B(D) + C \tag{17}$$

$$p(\mathrm{D}) = \frac{dP(D)}{dD} = 2A(D) + B \tag{18}$$

$$A_i = 6(1-\varepsilon)[2A(D) + Bln(D)]_{D_{min}}^{D_{max}} \quad (19)$$

In practice, it was found that a combination of a power and a polynomial provided the best fit for P(D). The area is then calculated as a summation of the two integrals, where D_i is the diameter below which the power law is used, and above which the 2nd order polymonial is used:

$$A_i = 6(1-\varepsilon)\left(\left[\frac{a\Lambda D^{\Lambda-1}}{\Lambda-1}\right]_{D_{min}}^{D_i} + [2A(D) + Bln(D)]_{D_i}^{D_{max}}\right) \quad (20)$$

If D_{min} represents the actual physical minimum particle diameter, then equation 20 will be appropriate, however, if D_{min} represents the particle size below which particles will cluster together to form lumps, then the mass of these lumps are given as follows, where n is the number of lumps:

$$\text{Mass of lumps} = \text{n}\frac{\pi D_{min}^3}{6}\rho_s = P(D_{min})\rho_b \quad (21)$$

$$\text{n} = \frac{P(D_{min})\rho_b}{\frac{\pi D_{min}^3}{6}\rho_s} \quad (22)$$

$$\text{Area of lumps} = \text{n}\pi D_{min}^2 = 6\frac{P(D_{min})}{D_{min}}\frac{\rho_b}{\rho_s} = 6(1-\varepsilon)\frac{P(D_{min})}{D_{min}} \quad (23)$$

Adding equation 23 to 20 yields:

$$A_i = 6(1-\varepsilon)\left(\left[\frac{a\Lambda D^{\Lambda-1}}{\Lambda-1}\right]_{D_{min}}^{D_i} + [2A(D) + Bln(D)]_{D_i}^{D_{max}} + \frac{P(D_{min})}{D_{min}}\right) + \quad (24)$$

2.4. Soil science models of multi-phase flow

The water retention curve (WRC) and the hydraulic conductivity function (HCF), which are rooted in pore-scale capillary and viscous flows, often form part of analytical and numerical models for flow and transport in unsaturated porous media. The WRC describes the relationship between soil matric potential (capillary head), h (m), and the soil water content, θ (m^3/m^3). The soil water content is typically represented as dimensionless effective saturation, S_e (equation 25a), or degree of saturation, S (equation 25b), where θ_s and θ_r are the soil saturated and residual volumetric contents, respectively (Assouline and Or, 2013).

$$S_e = \left(\frac{\theta-\theta_r}{\theta_s-\theta_r}\right) \quad (25a)$$

$$S = \left(\frac{\theta}{\theta_s}\right) \quad (25b)$$

The HCF takes on a form similar to Darcy's law. However, the unsaturated condition, unlike Darcy's law, gives rise to a highly nonlinear function that varies with θ or h. The HCF is often expressed in terms of the relative hydraulic conductivity (K_r) which is scaled by dividing the hydraulic conductivity (K_w) of the solution by the saturated hydraulic conductivity, K_s (equation 26).

$$K_r = \frac{K_w}{K_s} \quad (26)$$

Hydraulic properties of unsaturated soils have been modelled by authors such as Burdine (1953) and Mualem (1976), who attribute to the soil a single unimodal pore size distribution governed by capillary action. Burdine's model (1953) defines the relative solution conductivity (K_r) in terms of the ratio between the square of the mean hydraulic radius (r_H) of the unsaturated soil at effective saturation (S_e) to the square of the mean hydraulic radius of the soil at full saturation (S_e = 1). Applying the capillary law ($r_H = C / h$), Burdine derived equation 27 (Table 2), where h is the capillary pressure, γ is the pore-size interaction term, and b and q are constants. For the Burdine model, γ = 2, b = 2 and q = 1. Mualem (1976) replaced the pore configuration with a pair of capillary elements whose lengths are proportional to their respective radii, and by comparison of 45 soils, he found γ = 0.5 to provide the best fit when using measured K_s values as matching point. The Mualem model, also described by equation 27, has γ = 0.5, b = 1 and q = 2.

Brooks and Corey (BC) (1964) observed that for a large number of experimental data sets, the WRC can be represented by equation 28 (Table 2). The dimensionless number λ is referred to as the pore-size distribution index and is usually in the range of 0.3 to 10 (Kosugi *et al.*, 2002). The BC function is discontinuous, and has a distinct air-entry head, h_c, above which the soil is assumed to be saturated. Brooks and Corey (1964) substituted equation 28 into Mualem's formula in order to derive the HCF (equation 29), where n_p is a fitting parameter ($n_p = (2 + 3\lambda) / \lambda$). The BC model has been found to work well for relatively coarse-textured soils exhibiting a well-defined air-entry value and a J-shaped retention curve. However, the model may give relatively poor fits for soils with S-shaped retention data such as finer-textured soils and undisturbed field soils (Kosugi *et al.*, 2002).

Table 2. Summary of correlations used

	Burdine	**Mualem**
HCF	$K_r = S_e^{\gamma}\left[\frac{\int_0^{S_e}\frac{dS_e}{h^b}}{\int_0^1\frac{dS_e}{h^b}}\right]^q$ (27)	
	γ = 2, b = 2, q = 1	γ = 0.5, b = 1, q = 2
	Brooks-Corey (BC)	**Van Genuchten-Mualem (VGM)**
WRC	$S_e = \left(\frac{h_c}{h}\right)^{\lambda}$, h < h$_c$ $S_e = 1$, h ≥ h$_c$ (28)	$S_e = [1 + (\alpha h)^n]^{-m}$ (31)
HCF	$K_r = (S_e)^{n_p}$ (29)	$K_r = S_e^{\gamma}\left[1 - \left(1 - S_e^{\frac{1}{m}}\right)^m\right]^2$ (32)
ACF	$K_g = K_{g\,max}(S_g)^{n_g}$ (30)	$K_g = K_{g\,max}(1 - S_g)^{\gamma}\left[1 - S_g^{\frac{1}{m}}\right]^{2m}$ (33)

A continuous WRC function (equation 31) was also proposed by van Genuchten (1980), where m and n are fitting parameters, and α corresponds approximately to the inverse of the air entry value. Van

Genuchten (1980) further proposed the relationship of $m = 1 - 1 / n$ ($n > 1$, $0 < m < 1$) and substituted equation 31 into Mualem's formula (equation 27) to derive the van Genuchten-Mualem (VGM) HCF (equation 32). The VGM function has an inflection point and has been found to perform well on soils characterised by an S-shaped retention curve. However, the model cannot accurately describe retention characteristics for soils with distinct air-entry regions (Kosugi *et al.*, 2002).

The VGM model was further adapted by Parker *et al.* (1987) to describe the air conductivity function (ACF) (equation 33), where K_g is the air conductivity, and $K_{g\,max}$ is the air conductivity when only residual moisture is present (corresponding to $S_g = 0$). S_g is the relative degree of gaseous saturation, as defined by equation 34, and θ_{aep} is the air entry point or the maximum solution moisture content (corresponding to $S_g = 1$), at which the air conductivity drops off completely as the bed becomes saturated. It is also proposed that above the air entry point continuous air channels disappear, as well as free surface solution flow.

$$S_g = \left(\frac{\theta - \theta_r}{\theta_{aep} - \theta_r}\right) \tag{34}$$

Whereas much research has been published on the unsaturated hydrology of sand, little published material is available for coarser rocks and agglomerates. Lupo (2011) claimed that, to his knowledge, no measured WRCs have been reported for +10 mm run-of-mine ore heaps or waste rock in the laboratory, and that WRCs have been performed only on fine-grained soils and coarse-grained soils and gravels. Moreover, direct measurement of the HCF is seldom performed, rather the HCF is often calculated from the WRC using the measured K_s.

However, Newman *et al.* (1997) had in fact measured WRCs and K_s on sampled waste rock using large pressure plates and the WRC was used to predict the HCF. The samples were 10% to 50% -4.75 mm and 100% -50 mm. The HCFs indicate that rock samples with high fines content have a high unsaturated hydraulic conductivity, whereas samples with low fines content drained rapidly under negative pore-water pressures and therefore experienced a rapid decrease in hydraulic conductivity. O'Kane (2000) performed column studies and numerical modelling and proposed that in unsaturated, multi-layered systems, liquid water may be transported preferentially through fine-grained material, since it has a higher matric suction. Once the K_s of the fine-grained fraction is exceeded, essentially all flow is through the coarser fraction, which has a higher K_s but lower matric suction.

Afewu (2009) performed WRC and HCF measurements with soil suction sensors in column tests on a copper oxide ore (-10 mm). Although both BC and VGM models fitted the data, different values of K_s were predicted for the two models. Afewu (2009) recommended that the measured K_s should not be used to scale the HCF. Luckner et al. (1989) pointed out that K_s values measured in the field under a slightly positive water pressure are generally dominated by soil properties and may have little relation to the hydraulic conductivity in the unsaturated water content range. Hence it was recommended that K_s be made a fitting parameter, or a measured unsaturated hydraulic conductivity value in the relative wet range should be selected as a matching point for the conductivity function.

Mohanty *et al.* (1997) suggested that because of its large variability, K_s is not a good physical parameter for fitting or scaling of HCFs of field soils. In spite of this, K_s is still popularly used as a matching point in most hydrology studies since it can be more easily measured and may lead to extreme underpredictions or overpredictions of related fitting parameters. It was suggested that closed-form functions such as VGM are accurate for unimodal pore size distributions but are inaccurate close to saturation for multimodal pore-size distributions, due to a disruption of the otherwise smooth pore-size distribution at or near the larger pores. Also, gravity flow dominates through the larger pores near saturation.

Guzman *et al.* (2008) indicated that the hydraulic conductivity changes gradually near full saturation and then decreases rapidly as saturation becomes smaller than about 67%. It was proposed that the inflection point of the hydraulic conductivity curve is associated with the partitioning of the total porosity into micro (intra-agglomerate) and macro (inter-agglomerate) porosity. A number of researchers (*e.g.* Gerke and van Genuchten, 1993) have developed bimodal or multimodal soil models incorporating sums of a number of VGM-type functions, or piece-wise continuous functions (Russo, 1988). These functions, however, became less accurate at midrange soil-water suctions. It was suggested that the VGM-type functions should be used only at low moisture contents (higher suctions) where capillary flow dominates, in conjunction with other more appropriate models where gravity flow dominates.

If the flow is modelled as a combination of two VGM-type functions, one would however expect the transition from fine to coarse material to correspond with an increase in flowrate. However, in the present study the bed is not multi-layered but agglomerated to produce a more homogeneous packing and the data shows a single continuous capillary function, followed by a flattening off of the HCF curve, rather than an upward trend. This appears to contradict representation of the HCF function as a combination of multiple VGM-types representing fine-grained and coarse-grained zones (Gerke and van Genuchten, 1993).

Flow and transport in structured porous media are frequently described using dual porosity models. Such an approach assumes that the medium consists of two regions, one associated with the macropore or fracture network and the other with a less permeable pore system of soil aggregates or rock matrix blocks (Gerke and van Genuchten, 1993). In the example in Figure 3, the bed is divided into a fracture (coarse) fraction and a fines (matrix) fraction. Each fraction is modelled separately with a VGM equation (32). The overall hydraulic conductivity is a summation of the hydraulic conductivities in each phase, multiplied by its volume fraction. Gerke and van Genuchten's (1993) parameters for the fines and coarse fractions were used, but the volume fraction of coarse and fines material was specified as 50% each. At low moisture content, liquid is transported preferentially through fine-grained material, since it has a higher matric suction until the K_s of the fine-grained fraction is exceeded (O'Kane, 2000). Once the fines fraction is filled up, solution starts to flow through the coarse fraction. Hence K is governed by the fines fraction at low moisture contents and by the coarse fraction at higher moisture contents. In Figure 3, the overall hydraulic conductivity keeps increasing at higher S_e as the curve is governed by the VGM-shape of the coarse fraction. For comparison, the results of a real sample (MSTH) was plotted on the same graph. The real data shows neither the low K values at lower S_e

indicative of preferential flow through fines (Figure 3), nor the strong upwards trend in *K* as S_e tends to 1 (Figure 4).

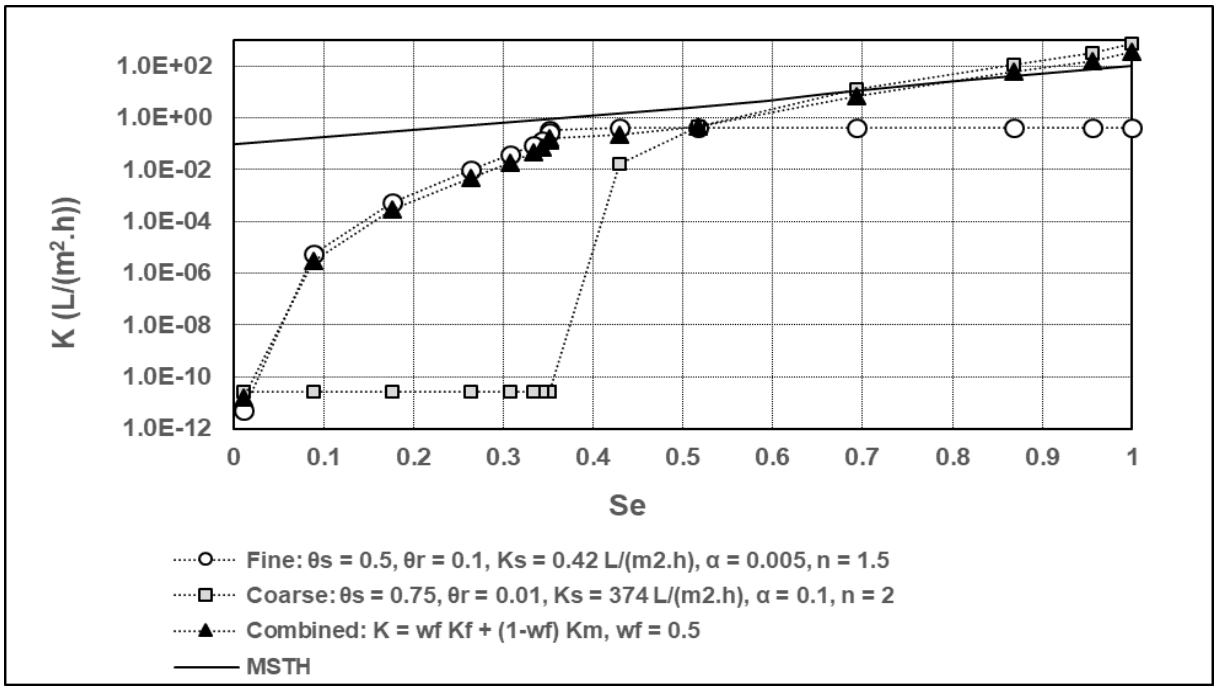

Figure 3. Dual porosity model (Logarithmic scale on y-axis)

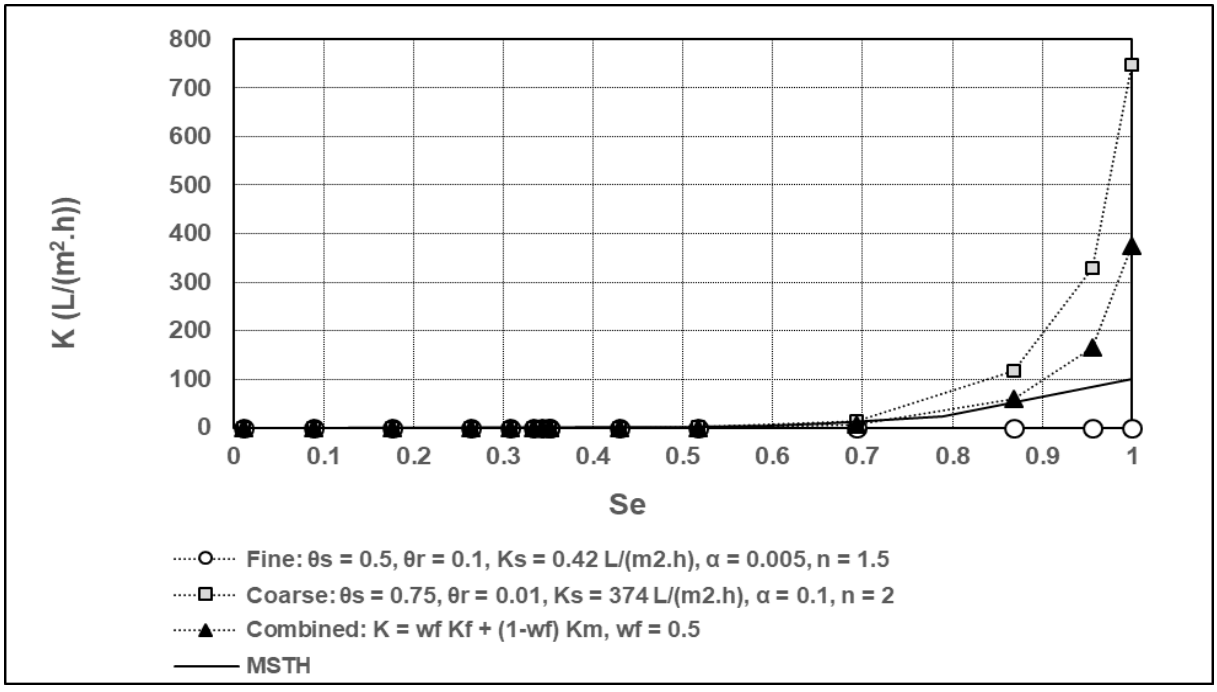

Figure 4. Dual porosity model (Linear scale on y-axis)

2.5. Flow of gas in packed beds (with residual immobile liquid phase)

For gaseous flow in packed beds with a residual immobile liquid phase and low gaseous Reynold's number, the Carman-Kozeny equation (35) can be used, where U_i is the interstitial velocity of gas flowing through the bed, μ is the dynamic viscosity of the gas, ΔP is the pressure drop over the bed, ΔL is the length of the bed, ε_g is the gaseous void fraction, A_i is the exposed wetted surface area, and r_H is the hydraulic radius ($r_H = \varepsilon_g / A_i$). In this case, the flow through the bed is gaseous, compared with the saturated flow of solution proposed in equation (4):

$$\frac{\Delta P}{\Delta L} = \frac{2\mu U_i}{r_H^2} = \frac{2\mu U_i A_i^2}{{\varepsilon_g}^2} \tag{35}$$

Similarly, the pressure drop – flow relationship for gaseous flow through the bed is also expressed by Darcy's equation (36), where K_g (cm/s) is the air conductivity. Q/A in equation (36) is replaced by the superficial gaseous velocity (U_s). The superficial velocity (U_s) is related to the interstitial velocity (U_i) by equation (37). U_s is replaced by U_i in equation (36), yielding equation (38), where τ is the tortuosity:

$$\frac{\Delta P}{\Delta L} = \frac{\rho g}{K_g}\frac{Q}{A} = \frac{\rho g}{K_g} U_s \tag{36}$$

$$U_s = U_i \frac{\varepsilon_g}{\tau^2} \tag{37}$$

$$\frac{\Delta P}{\Delta L} = \frac{\rho g}{K_g} U_i \frac{\varepsilon_g}{\tau^2} \tag{38}$$

$\Delta P/\Delta L$ may be eliminated by equating Darcy's law (38) with the Carman-Kozeny equation (35), and re-arranging to make r_H the subject of the formula:

$$r_H = \tau \sqrt{\frac{K_g\, 2\mu}{\rho g \varepsilon_g}} \tag{39}$$

For the case where the bed contains only the stagnant moisture ($S_g = 0$), $K_g = K_{g\,max}$. $K_{g\,max}$ is determined from a solution of the air permeability curve (equation 33) by plotting K_g against S_g, and reading off K_g at the point where S_g equals zero. The methodology of fitting the air permeability curve is described in section 5.2.1.

2.6. Low permeability ores

Most of the ore samples reviewed by the author over the past decade were able to conduct solution in hydrodynamic column tests without pretreatment such as desliming or agglomeration with binder. The presence of high amounts of clay is typically associated with low permeability. Hence there is a need to study samples with low permeability which are not suited for percolation leaching, and to develop a cost-effective pretreatment method to make them suitable for this process. Currently, a number of approaches are taken to address low permeability in heap leach plants. These include:

- Screening out and discarding fines (Dhawan *et al.*, 2013), *e.g.* the Kabolela, ENRC (Eurasian Natural Resources Corporation) and Kipoi operations (SEK) (Société d'Exploitation de Kipoi, 95% owned by Tiger Resources Limited) (Kruger, 2017) in the DRC.
- Screening out fines and using a combined heap leach and tank leach circuit (John, 2011), *e.g*. Kipoi, DRC (Kruger, 2017) and Mimbula, Zambia (Moxicoresources, 2020) (Figure 4).
- Agglomeration with binders such as acid (copper ores) or cement (gold ores) (Kappes, 2002; Dhawan *et al.*, 2013).
- Using other leaching systems such as cribs, ponds and vats (John, 2011).
- Blending in more competent ores with the low-permeability, clay-bearing ores *e.g*. Benkala, Kazakstan (Keller *et al.*, 2022; Whiterow, 2003; Kappes, 2002).
- Installing retaining walls, horizontal drains and vertical dewatering wells, *e.g.* Cerro Verde, Peru (Galdos *et al.*, 2013); Chuquicamata, Chile (Ramirez *et al.*, 2019).

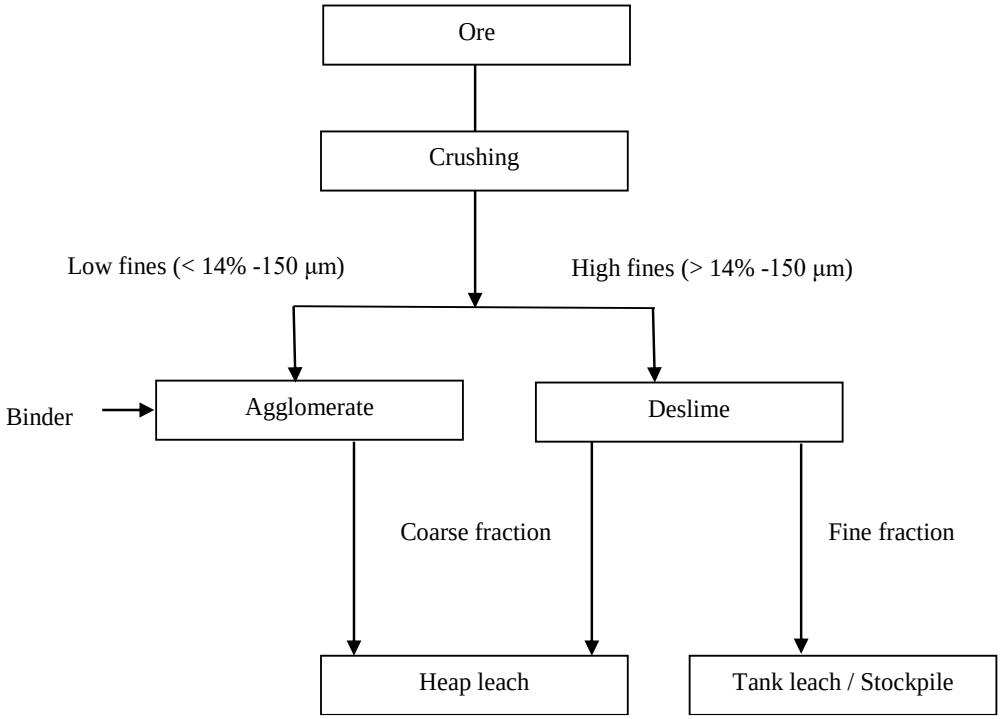

Figure 5. Process options for heap leaching of clay-rich Kipoi ore

Some operations such as Kabolela (ENRC), located in the Katanga province of the DRC, contain both copper and cobalt. The current practice is to screen out the fines <0.6 mm and stockpile them, which represents about 26% of the copper. The Kipoi (SEK) operation is located near Lubumbashi, also in the Katanga province of the DRC. The first phase of the project focused on the production of dense media separation (DMS) concentrate, whereas the second phase focused on heap leaching of the DMS reject material (the so-called DMS floats), as well as ores from satellite deposits. Phase 3 of the operation involved the construction of an agitated tank leach plant and counter-current decantation (CCD) circuit (van Staden *et al.*, 2017, Kruger, 2017). In the case of the Kabolela operation, screening out of fines

results in significant copper and cobalt losses if the fines cannot be treated. However, construction of a tank leach plant for Kipoi (and planned for the Mimbula (Moxico Resources) project) will result in increased capital cost and financial risk, especially in the case of small companies with highly geared balance sheets.

An agglomeration binder will allow whole ore acidic heap leaching of incompetent copper, copper / cobalt, laterite and uranium ores. It will also reduce capital and operational costs, financial and technical risk, and result in higher metal recovery, and higher revenue flow, as suggested in Table 3.

Table 3. Examples of potential revenue increase from improved copper recovery

Project	Production (tpa Cu)	Fines Loss (%)	Revenue [1] (M US $ / a)	Revenue [2] (M US $ / a)	Increase (%)
Benkala (Frontier Mining)	20 000	40 [3]	72	120	67
Mimbula oxide (Moxico)	5 000 [3]	40	18	30	67
Mimbula stockpile (Moxico)	5 000 [3]	60	12	30	150
Kabolela (ENRC)	5 000 [3]	20	24	30	25
Kileba (SEK)	25 000	15	128	150	18
Kipoi North (SEK)	25 000	15	128	150	18

Notes:

1. *Fines removal (by screening)*
2. *Agglomeration binder*
3. *Estimation*
4. *A copper price of US $ 6000 / tonne and uniform copper distribution in the ore were assumed. The contribution to revenue from cobalt recovery was ignored for the sake of simplicity.*

Problems in air permeability have been addressed as follows:

- Introduction of air at heights above the phreatic layer (Menacho and Cifuentes, 2013).
- Introduction of multiple air lifts (Arpalahti and Lundström, 2019).
- Optimisation of aeration spacing (Reyes, 2007).
- Use of a coarser crush size (Logan *et al.*, 2007).
- Use of rest cycles (Rautenbach, 2015).
- Optimisation of ratio between irrigation and aeration rates (Dew *et al.*, 2011).

Disadvantages of the current treatment options include the following:

- The current method of fines removal to treat ores with high clay content and poor permeability, results in significant copper and cobalt losses if the fines are stockpiled (*e.g*. Kabolela, DRC).
- The construction of a tank leach plant for treatment of the fines results in increased capital cost and financial risk, especially in the case of small companies with highly geared balance sheets (*e.g.* Kipoi, DRC).
- Blending in more competent rock with low-permeability ore (*e.g.* Benkala, Kazakhstan) will result in substantial additional mining and crushing costs.

- Geotechnical solutions such as the installation of horizontal drains and vertical dewatering wells, will result in short-circuiting of leach solution, with areas of poor permeability receiving less contact with the lixiviant (*e.g.* Cerro Verde, Peru).
- The current application of cement as an agglomeration binder is limited to gold ores and no commercial binder (except sulphuric acid) is currently employed for copper ores.
- Alternative technologies for copper and laterite ores (*e.g.* whole ore tank leaching, whole ore pressure leaching and smelting) are highly capital intensive and cannot be applied to low-grade ores, or in perceived high-risk investment regimes with poor infrastructure.
- Existing forced aeration systems are limited in supplying air to heaps with high fines content. Air bypasses regions of low permeability and high moisture content, even if laboratory results indicate that air permeability can be achieved. Air permeabilities in heaps are not easily measured and geomechanical criteria are often based on “rules of thumb” or “experiential rules”, such as the requirement to maintain a degree of void saturation of below 60% to 65% for forced aeration. Such experiential rules are quoted by authors such as Robertson *et al.*, (2013) and Milzcerak *et al.* (2012) without providing more fundamental studies.
- Changes in hydrodynamics during scale-up are usually not quantified and often results in poorer performance in the field than in the laboratory.
- The use of a coarser crush size to improve aeration (Logan *et al.*, 2007) results in poorer mineral liberation with less mineral area exposed to the leach solution.
- The use of irrigation and rest cycles (Rautenbach, 2015; Logan *et al.*, 2007) results in a reduced rate of acid supply, which may be detrimental if the ore contains acid-consuming gangue minerals which require acidification to reduce the pH to the required regime (e.g. pH 1.3 to 2.2) before bioleaching can begin.

2.7. Agglomeration with cement / binder

Agglomeration with cement is commonly used for gold and silver heap leach operations (performed in alkali medium). Crushed ore agglomeration has been successfully utilised as a pretreatment step and has two major aims: (1) to allow thorough application of leach solution and “kick start” the leach process, and (2) the application of leach solution or binder allows fine particles to coalesce onto larger rock particles and reduce segregation (Wang *et al.*, 2021; Ghorbani *et al.*, 2015; Dhawan *et al.*, 2013). However, apart from sulphuric acid (H_2SO_4), there is currently no commercially available binder for heap leaching in acid medium (*e.g.* copper, uranium and nickel ores), although a number of materials have been tested. This may also be the result of high cost, high consumption and lack of acid-tolerant and microbial-resistant binders (Ghorbani *et al.*, 2015).

For example, inorganic binders (*e.g.* clays, lime, iron(II) sulphate, silicic acid and calcium sulphate) and organic binders (*e.g.* agar, cellulose, gelatin, lignin and starch) were found to deteriorate under acidic conditions (Lewandowski *et al.*, 2009). Polymeric binders (*e.g.* polyvinyl acetate, polyethylene oxide resins, Extract-Ore 9560 and Extract-Ore 9760) performed better, but have not found widespread

application, possibly due to the high cost of organic materials. Lime, molasses and wood fibres were found to have insufficient strength (Bouffard, 2008). Geopolymerisation of alumina-silicates was tested by Chen *et al.* (2020), but very high dosages (50 to 100 kg/t ore) are required. The use of stucco similarly required high dosages (30 to 50 kg/t) (Kodali *et al.*, 2011).

Lewandowski and Kawatra (2009) and Kawatra, *et al*. (2006) describe five categories of agglomeration binding:
(1) Solid bridges formed by sintering, partial melting, chemical reactions, hardening binders, recrystallization and during drying;
(2) Adhesion and cohesion forces occurring at solid-liquid interfaces when highly viscous binders are employed;
(3) Surface tension and capillary forces formed by liquid bridges;
(4) Attraction forces between solid particles due to molecular, electric and magnetic forces;
(5) Entanglement of particles leading to interlocking bonds.

Cements are adhesive substances capable of uniting fragments or masses of solid matter to a compact whole (Lea, 1956). Ordinary Portland Cement (OPC) is created by heating limestone and clay, or other materials to a temperature of about 1450°C. Partial fusion occurs, and nodules of clinker are produced and mixed with calcium sulfate and finely ground to make cement. Clinker usually has a composition of about 67 % CaO, 22 % SiO_2, 5 % Al_2O_3, 3 % Fe_2O_3 and 3 % other compounds. It typically contains four major phases: alite, belite, aluminate and ferrite. Hardening results from reactions between major and minor phases and water (Taylor, 1997).

Common cement types are classified in Table 4 based on composition (Grieve, 2009). Portland cement is defined as CEM I and is composed of 100 % clinker. Production of Portland clinkers is energy intensive and additives of natural and artificial materials that are able to react with lime to produce a cementitious product are used (Snellings, *et al*., 2012). Portland composite cements CEM II A-M and B-M are composed of clinker, fly ash, limestone and ground granulated blast furnace slag (GGBFS). Blast furnace cement (CEM III) occurs as three types – A, B and C. Each contains GGBFS and clinker in varying proportions. Pozzolanic cements (CEM IV) A and B contain fly ash and clinker, and finally composite cements (CEM V A) contain fly ash, GGBFS and clinker.

The reaction when cement is mixed with water is called hydration and results in setting and hardening of the cement paste (Saleh and Eskander, 2020). Hardening results from various chemical reactions between the calcium aluminates and silicates present and water.

Robertson and co-workers (2020, 2022a and 2023a) have recently shown that OPC, modified with additives such as fly ash and furnace slag, can be used as an agglomeration binder for heap leaching in acid medium. Test work was performed on low-permeability micaceous stockpile material (MSTH), which was agglomerated with various dosages (0 kg/t, 1 kg/t, 3 kg/t and 10 kg/t) of pozzolanic or composite cement and water, followed by curing for 2 or 28 days. At binder additions of 10 kg/t, the compressed samples maintained the targets of >30% porosity and >1000 L/m^2/h saturated hydraulic conductivity at a compression equivalent to a 6 m lift height. The samples also experienced minimal

slumping in leach columns in the presence of 8 g/L H_2SO_4, whereas without binder the samples slumped excessively, leading to ponding.

Hence in Part III of this test work programme, pozzolanic and modified cements were investigated as agglomeration binders for low-permeability ores, which are heap leached in acid medium. The effect of agglomeration with binder on the physical and hydraulic properties was investigated with uni-axial compression tests, hydrodynamic column tests and leach column tests.

Table 4. Cement classifications (Grieve, 2009)

Main types	Types of common cement		Clinker	Blast Furnace slag	Silica fume	Pozzolana		Fly ash			Limestone	
						Natural	Natural calcined	Siliceous	Calcareous	Burnt shale		
			K	S	D	P	Q	V	W	T	L	LL
CEM I	Portland cement	CEM I	95-100	-	-	-	-	-	-	-	-	-
CEM II	Portland-slag cement	CEM II A-S	80-94	6-20	-	-	-	-	-	-	-	-
		CEM II B-S	65-79	21-35	-	-	-	-	-	-	-	-
	Portland-silica fume cement	CEM II A-D	90-94	-	6-10	-	-	-	-	-	-	-
	Portland-pozzolana cement	CEM II A-P	80-94	-	-	6-20	-	-	-	-	-	-
		CEM II B-P	65-79	-	-	21-35	-	-	-	-	-	-
		CEM II A-Q	80-94	-	-	-	6-20	-	-	-	-	-
		CEM II B-Q	65-79	-	-	-	21-35	-	-	-	-	-
	Portland-fly ash cement	CEM II A-V	80-94	-	-	-	-	6-20	-	-	-	-
		CEM II B-V	65-79	-	-	-	-	21-35	-	-	-	-
		CEM II A-W	80-94	-	-	-	-	-	6-20	-	-	-
		CEM II B-W	65-79	-	-	-	-	-	21-35	-	-	-
	Portland-burnt shale cement	CEM II A-T	80-94	-	-	-	-		-	6-20	-	-
		CEM II B-T	65-79	-	-	-	-	-	-	21-35	-	-
	Portland-limestone cement	CEM II A-L	80-94	-	-	-	-	-	-	-	6-20	-
		CEM II B-L	65-79	-	-	-	-	-	-	-	21-35	-
		CEM II A-LL	80-94	-	-	-	-	-	-	-		6-20
		CEM II B-LL	65-79	-	-	-	-	-	-	-	-	21-35
	Portland -composite cement	CEM II A-M	80-94	6-20								
		CEM II B-M	65-79	21-35								
CEM III	Blastfurnace cement	CEM IV A	65-89	36-65	-	-	-	-	-	-	-	-
		CEM IV B	45-64	66-80	-	-	-	-	-	-	-	-
		CEM IV C	5-19	81-95								
CEM IV	Pozzolanic cement	CEM IV A	65-89	-	11-35					-	-	-
		CEM IV B	45-64	-	36-55					-	-	-
CEM V	Composite cement	CEM V A	40-64	18-30	-	18-30			-	-	-	-
		CEM V B	20-39	31-50	-	31-50			-	-	-	-

3. PROBLEM STATEMENT AND OBJECTIVES

3.1. Importance of hydrodynamics during heap leach design

Very little has been published to date on the hydrology of coarse rocks and heap leach agglomerates. The data generated by the author over the past decade therefore presents an opportunity to improve the understanding of heap leach hydraulics. Currently the design of irrigation and aeration systems relies to a large extent on geomechanical criteria and rules of thumb. The author wishes to provide a more fundamental background to these experiential rules and guidelines.

The need also exists to better understand and engineer aeration systems for the supply of air to microbially-assisted and acidic chloride leach systems of secondary copper sulphide ores, and to define regimes of limitation with respect to air and solution flow. Air permeability in ore beds can be related to the availability of macro-pores and void spaces not filled with solution. This is determined by parameters such as bulk density (compaction), irrigation rate and fines content. For example, increased compaction reduces void space, whereas increased irrigation rate and fines content increase the moisture hold-up, which also reduces the gaseous porosity. The ratio between larger and smaller voids is also important, as well as the interconnectivity between voids. For example, larger voids may create more gaseous porosity, but if they are poorly connected this will not increase air flow. Irrigation-rest cycles may also be employed to improve aeration, due to reduced moisture hold-up and higher gas-liquid mass transfer area during the resting cycle.

Another factor which is not clearly understood and is often overlooked is the increase in non-homogeneity during scale-up, which, combined with higher bulk density often results in poorer performance in the field. This is discussed in greater detail by Bouffard and West-Sells (2009) and Robertson (2017). For example, metallurgical column tests are often performed at lower “as placed” bulk densities of the order of 1.3 t/m^3, whereas bulk densities in the field are often in the order of 1.6 to 1.8 t/m^3.

Most heap leach models do not take into account changes in hydrodynamics during scale-up, but simply assume uniform flows of air and solution in order to solve mineral dissolution kinetics. An example is Bartlett (1998) who models the bed as a vertical front moving through the ore bed at constant velocity and constant liquid hold-up. Bennet *et al*. (2012), Cariaga *et al.* (2015), Simunek and van Genuchten (2008) and Robertson *et al.* (2013) use Richard’s equation to describe the change in liquid hold-up with flowrate. McBride *et al.* (2006) also uses Richard’s equation, but divide the bed into regions of different permeability. These models tend to overestimate the leach kinetics, solution and air transport and contact in the bed. Uniform flow models may be suited to column tests and heaps containing competent material with low clay content. Non-homogeneity was not addressed as part of this research, as it is more relevant on a larger scale, and the test work was limited to the laboratory scale. In practice there are areas of poor solution contact, which may explain the longer leach times that are often required in the field as compared to column tests. Non-homogeneity was addressed by Bouffard and Dixon (2001), de Andrade Lima (2006) and Roberson (2017, 2019), who modelled the bed as comprising mobile and

immobile regions. Miller (2003) and Dixon and Petersen (2003) modelled the bed as governed by diffusional “macro-particles” interspersed with advective flow channels. During scale-up, an increase in non-homogeneity may be addressed by increasing the width between the flow channels. Van Staden (2018, 2019) suggests that changes during scale-up may be attributed to dripper spacing or bulk density but not to segregation or stratification effects.

The moisture hold-up and residual moisture in the heap leach operation are important to quantify, as they determine not only the ease of handling of the residues but also the losses of moisture to the residues. Water that is lost to the residues needs to be replaced by supplying fresh water to the circuit. In water-scarce regions, such as Arizona (USA) and the Atacama desert (Chile), this can become an important cost factor, especially as granting of water permits becomes more stringent and mining operations compete with other uses such as agriculture. In water-rich areas such as the DRC, high moisture contents are undesirable, and can result in poor permeability, as well as handling problems such as blockage of the conveyor belts. Hence an understanding of the moisture hold-up and residual moisture is critical to the operation of the heaps. The residual moisture hold-up is normally associated with the fines content as the fines have larger surface area to which the water can adhere.

An example where an additive was claimed to improve copper dissolutions and reduce residual moisture hold-up in copper heap leach operations by reducing the surface tension of the lixiviant, is the LixTRA™ surfactant manufactured by BASF. It is claimed that the additive reduces the droplet contact angle, which increases the wetting area of the mineral surface, improves interstitial lixiviant flow through the ore and increases the rate of copper recovery. It also claims to improve capillary action, allowing the lixiviant to penetrate deeper within the fractures of the ore, thereby improving copper dissolution (BASF Mining Solutions, 2024). Although the author expects these effects to be offset by the long leach times employed in heap leaching, it nonetheless provides an example of the importance of hydrodynamics in heap leaching.

3.2. Application of packed bed and soil science models

Both packed bed models (*e.g.* Lizama, 2009) and unsaturated soil science models have been used to describe heap leach hydrology. The validity of these models requires further investigation. For example, traditional capillary flow models such as BC and VGM (*e.g.* Afewu, 2009; Newman *et al.,* 1997) have been developed for sand and not gravel. This is highlighted by the discontinuity in the hydraulic conductivity function (HCF) with respect to K_s, which has been mentioned by several authors. These authors propose that a fitted parameter instead of K_s should be used when modelling the unsaturated portion of the HCF. The author aims to address this aspect in more detail.

Most authors propose a dual-porosity system, with transition from a capillary flow regime to a gravity-controlled flow regime at high saturations, accounting for the discontinuity in the hydraulic conductivity function. Although the presence of diffusional flow regimes and advective flow regimes have been demonstrated during scale-up (*e.g*. Bouffard and West-Sells, 2009), the “dual porosity” theory is often

used as a blanket explanation for hydrodynamic behaviour, even on a smaller 1-D scale, where it is not necessary valid.

3.3. Treatment of low-permeability ores

On a practical level, the need exists for a low-cost process to treat low-grade ores, wastes and small deposits, or deposits in perceived high-risk investment regimes with poor infrastructure. Heap leaching is often used as a low-cost process option for such ores, but in many cases it cannot be applied if the ore has poor solution permeability due to the presence of fines or clays. In such cases the stacked ore cannot conduct the percolating solution which supplies the leach reagent and drains the leached metals from the base of the heap.

Cement has found wide-spread application as an agglomeration binder in gold heap leaching operations, contributing to the growth in gold heap leaching world-wide, especially in West Africa. The OH-bonds associated with ordinary Portland cement break down in acid. However, modification with silicate additives (*e.g.* fly ash, furnace slag or silica fume) with pozzolanic activity converts OH-bonds to silicate bonds, which are stronger and more acid resistant. The application of an acid-proof silicate binder for copper ores is novel, as to date no binder has been successfully applied commercially for acidic heap leaching of ores (apart from acid).

Most research to date has focused on polymer binders, which do not maintain strength. The development of different forms of acid-resistant cement (such as perlite, potassium silicate, sodium silicate, modified Portland cement and alkali-activated cements) has therefore made it possible also to evaluate these materials for acid heap leaching. Supplementary cementitious materials (SCM) such as fly ash, furnace slag and silica fume have been shown to strengthen ordinary Portland cement (OPS) and change the chemical bonds by pozzolanic activity to make it more acid proof (Lothenbach *et al.*, 2011).

It is proposed that the permeability of clay-containing ores may be improved with an acid-proof binder such as sodium silicate, modified Portland cement or alkali-activated cements. The use of cement for acid leaching is counter-intuitive. However, it has merit as it is expected that the additional acid consumption brought about by the binder will be small, and the binder will work as long as the bonds are not destroyed during the acidic leaching. The binder joins together the coarse and fine particles, creating “macro-particles”, and thus increases the overall void space available for solution percolation. This improves the solution and air permeability of the heap and reduces fines segregation and non-homogeneous flow. This in turn results in faster overall metal dissolution rates, and shorter leach cycles, resulting in lower capital and operating costs.

In addition, alkali-activated cements have been manufactured from the SCM waste materials alone, thereby reducing CO_2 emissions associated with the manufacture of OPC. The alkali-activated cement was also used as low-cost building materials for low-cost housing while at the same time providing an avenue to recycle industrial wastes. The potential application of such materials as an agglomeration

binder for acidic heap leaching is therefore broad. Notwithstanding, this has not been tested to date. It also presents an opportunity to develop stronger cements for gold (alkali) heap leaching.

3.4. Objectives

The objectives of the current research may be summarised as follows:

- Provide a better fundamental understanding of the “rules of thumb” applied to hydrodynamic testing of ores and agglomerates for heap leach design (as summarized in Table 1). For example, Scheffel’s (2017) recommendation that the ore should not have more than 10% to 14% -150 µm material, was evaluated by plotting the compressibility of various ores and agglomerates against the PSD. The experiential rule that the bed should not contain more than 60% to 65% saturation in order to be suitable for forced aeration was evaluated by comparing the air entry point (determined from the ACF), against the percentage of the bed voidage that is available for solution flow (determined from the inflection point of the HCF).
- Develop correlations to describe relationships between saturated hydraulic conductivity (measured in both compression and hydrodynamic column tests) and pressure drop based on packed bed theory such as the Ergun and Kozeny-Carman equations. Also evaluate existing correlations such as Brooks-Corey and van Genuchten-Mualem in describing the HCF and ACF which is widely used in soil science models but has been applied in a few instances to coarse rocks and agglomerates in heap leaching. The effect of physical properties of the bed, such as PSD, porosity and distribution of porosity are incorporated in these correleations, for example the particle size is replaced with a hydraulic diameter in the Kozeny-Carman equation. The distribution of porosity is incorporated in the van Genuchten-Mualem equation as it defines the point of discontinuity in the HCF.
- Interventions including desliming and agglomeration with binder was investigated in order to improve permeability and allow percolation of low-permeability ores. It was also intended to demonstrate the causes of low permeability as it relates to physical parameters such as porosity and fines content, and its effect on hydrodynamic properties such as the steady-state moisture content during irrigation. An attempt was also made to evaluate the technical and economic feasibility of the above-mentioned interventions, in order to arrive at a cost-effective intervention for treating low-permeability ores.

4. EXPERIMENTAL

4.1. Selection of test samples

A list of samples used in the test work is provided in Appendices A, B and C, typically comprising drill cores from various copper, uranium and gold deposits that were supplied to Mintek for metallurgical test work. A large number of samples are from Africa or South America (Chile). The aim was to perform

heap leach amenability test work, which in many cases proceeded to pre-feasibility and bankable feasibility testing.

In most cases, test work typically included both uni-axial compression tests, hydrodynamic column tests and metallurgical column tests. In this thesis, the metallurgical column test results are excluded, except for the micaceous copper stockpile material, where the effect of desliming and agglomeration with a cementitious binder was investigated in a systematic way, comprising compression tests, followed by hydrodynamic column tests, short (1 m) metallurgical leach column test, and tall (4 m) column leach tests. For most of the other samples tested, crush sizes and curing acid additions were specified by the client or metallurgical consultant, or based on the particle size distribution. For example, incompetent samples were crushed to a coarser top size.

In some cases, the curing additions were determined by acid consumption measurements performed on milled head samples, or on acid-soak curing acid optimization tests not described here. For example, for acid-soluble copper ores the curing acid addition is typically 30% of the total net acid consumption. Samples included a Chilean copper porphyry, a Congolese sedimentary dolomite hosted copper oxide, a Spanish vein-type uranium ore, a Namibian sedimentary sandstone hosted copper oxide, transition and sulphidel and a Zambian sedimentary hosted copper oxide, mixed, sulphide and stockpile etc. Different crush sizes were used, as indicated in Appendices A, B and C.

4.2. Sample preparation

The samples were crushed to various top sizes between 1.7 mm and 50 mm with a jaw crusher (Figure 6a), and particle size distributions (PSDs) were performed by screening batch-wise using a Rhologan sieve shaker (Figure 6b). Head and leached residue samples were submitted for chemical analysis and were first crushed to -1.7 mm with a cone crusher (Figure 7a) and split into representative sub-samples with a rotary splitter (Figure 7b). The samples were further pulverised with a laboratory sample pulveriser, prior to chemical assay.

Figure 6a) Jaw crusher and b) Rhologan shaker

Figure 7a) Cone crusher and b) rotary splitter

In the case where desliming was performed, the sample was first scrubbed in a 1 m diameter, 0.26 m long trommel scrubber (Figure 8). The scrubber was fitted with a Watt- and tachometer and 4 lifter bars, 100 mm high. The scrubber was loaded to 20% of its volume with a slurry containing 50% solids, at a residence time of 10 minutes. Desliming was performed by wet screening the sample over a sieve (*e.g.* 75 µm, 150 µm or 212 µm) placed in a Rhologan shaker. The oversize was dried and agglomerated while rolling on a plastic sheet and adding 98% H_2SO_4 (6 to 22 kg/t) and tap water (Rand Water Board) (Figures 9 and 10), except for gold ores, which were agglomerated with the addition of cement and water only.

Figure 8. Trommel scrubber

Whole ore samples were agglomerated with cementitious binder by first blending the dry ore and the dry binder (1 kg/t, 3 kg/t or 10 kg/t) on a plastic sheet. For taller (4 m) leach columns, a cement mixer was used. Tap water (Rand Water Board) was then sprayed onto the sample while rolling on the plastic sheet until agglomeration was complete as judged by visual inspection (Figure 11). The agglomerates were allowed to cure for 2 or 28 days in an enclosed plastic bag. Three types of binders were used, as summarised in Table 5. All three contain fly ash, a pozzolanic material which generates calcium hydroxide when mixed with cement and water, which in turn reacts with calcium silicate hydrate to form calcium silicate. This differs from the hydration of OPC, which reacts with water to form calcium hydroxide and calcium silicate hydrate. Two binder types also contain slag (a byproduct of iron production). Slag is not a pozzolan like fly ash but is a non-metallic hydraulic cement which consumes calcium hydroxide in its hydration products (Goguen, 2020). According to the producer, slag increases durability and workability, as well as providing protection against chloride and sulphate attack (Afrisam, 2021). According to the classification of Table 4, Cement A can be classified as pozzolanic cement (CEM IV A), containing clinker and fly ash. Cements B and C can be classified as composite cement (CEM V), containing clinker, fly ash and furnace slag.

Table 5. Summary of binders

Binder	Description	Commercial Name
Cement A	64% OPC, modified with 36% fly ash (42.5 N)	Lafarge Buildcrete
Cement B	38% OPC, modified with a 50:50 mixture of fly ash and slag (32.5 N)	Afrisam Starbuild
Cement C	50% OPC, modified with a 50:50 mixture of fly ash and slag (42.5 N)	Afrisam All Purpose

Figure 9. Micaceous stockpile material agglomerates (+75 µm)

Figure 10. Micaceous stockpile material agglomerates (+212 µm)

Figure 11. Micaceous stockpile material agglomerates (10 kg/t cement C)

4.3. Uni-axial compression tests

The uni-axial compression test (stacking test (ST)) is an indicator procedure which determines whether a particular ore sample will support percolation leaching (Robertson *et al.*, 2013). Since the sample requirement is small (typically 6 kg to 10 kg) and the test duration is short, the ST can be used to compare parameters such as crush size, agglomeration moisture, curing acid addition and stacking height as part of variability testing. The results of the ST are normally interpreted in light of the PSD, for example to compare the amenability of different lithologies to percolation leaching.

Compression tests were performed to assess the behaviour of the ores and agglomerates under load according to the methods described by Robertson *et al.* (2013), Guzman (2012) and Lupo (2011). The agglomerates were loaded into a 150 mm ID or 200 mm ID test cell (Figures 12 and 13).

The stacking test is performed by mechanically increasing the confining load in a test cell to determine the effect of heap height on the bulk density and the hydraulic conductivity of the ore. The compressed sample represents a unit volume of ore located at the bottom of the heap. Besides qualifying the ability of a sample to support a percolation leaching process, the ST helps to identify the maximum lift / heap height that the sample might support. The load exerted by the ram is converted to an equivalent stacking height by taking into account the bulk density of the ore and area of the test cell. The ram therefore simulates the weight exerted by a mass of material on a unit are of the heap. The parameters measured include the bulk density profile, porosity profile and air conductivity profile as a function of stacking height (load).

After compression to the maximum load (typically representing a 6 m stacking height), the load is released. The cell is then saturated with water and the saturated hydraulic conductivity is measured by passing solution upward through the bed while maintaining a constant solution head (Milzcerak *et al.*, 2013). Finally, the cell is allowed to drain and the residual moisture is determined by drying the solids at atmospheric conditions and recording the masses of the wet and dry solids. The ratio between drained and residual moisture is determined.

It was found that in the case of high fines-containing ores, the agglomeration process forms large clay lumps, resulting in an initially low “as placed” bulk density in the cell. This would then underpredict the bulk density profile and overpredict the strength of clay- and silt-containing agglomerates. During wetting, the fines turn into a viscous sludge which enables consolidation of larger particles under the weight of the bed. Non-saturated flow channels may be occluded in the process. Rapid ore wetting and subsequent collapse occurs as the solution flows under gravity into the agglomerated ore, rapidly increasing saturation and weakening capillary and direct contact forces that keep particles together. Rapid saturation may also loosen fine particles from the agglomerated surface and break down the structure, in addition to chemical decrepitation (Arellano *et al.*, 2022). If the material is non-saturated, an increase in load compacts the mass and increases shear strength. However, increasing moisture content results in increasing pore pressure and has a buoying effect, reducing the friction and shear strength. As most of the slumping normally occurs during initial wetting, it was decided to modify the procedure in the case of the very high silt- and clay-containing micaceous copper oxide stockpile

material (MSTH), by pre-wetting the agglomerates by irrigation with 5 g/L H_2SO_4 for 24 hours, followed by draining for an additional 24 hours.

Figure 12. Uni-axial compression test apparatus

Figure 13. Apparatus for measuring saturated hydraulic conductivity

4.4. Hydrodynamic column tests

Test methods for determination of hydraulic properties are described by Cherkaev (2019), Ilankoon (2012), Ilankoon and Neethling (2012) and Guzman *et al.* (2008). Changes in the mass of the bed due to changes in irrigation flux were recorded continuously by placing the column on an electronic balance (Afewu, 2009) or by supporting the column on a load cell coupled to a data logger (Cherkaev, 2019; Ilankoon and Neethling, 2012). The apparatus used for the work reported here comprises a 15 or 20 cm diameter column (75 cm tall), loaded with agglomerates at a uniform target bulk density (based on the compression test profile) and irrigated at incremental solution application rates (Figure 14).

The hydrodynamic column (HCT) relies on the density profile derived from the stacking test to select the bulk density value required to properly represent the desired lift / heap height. The column (15-cm or 20-cm diameter, 75 m or 100 cm tall) is loaded with agglomerates at a uniform target bulk density and is irrigated at incremental solution application rates (Robertson *et al.*, 2013). From the solution balance tracked throughout the duration of the test follows the hydraulic conductivity and solution content (*i.e.* degree of saturation). Also obtained from the HCT test are the air conductivity, the drain down curve, and total, micro- and macro-porosity. In other words, the HCT provides all the necessary hydrodynamics required to simulate the solution and air movement through a heap. From the more practical point of view, the HCT answers the key question for the design of a heap – the degree of saturation resulting from a given application rate. Experience shows that for copper oxide leaching the maximum liquid saturation should be kept below 85% and ideally under 65% to accommodate the natural variability associated with the heap stacking process. Leaching of a sulphide ore requires that the degree of saturation remains below 60% to ensure that forced (or natural) aeration can be properly implemented.

By design a sample subjected to a HCT represents a unit volume of ore located at the bottom of the lift – the portion of the heap which experiences the most stringent conditions since it is exposed to the maximum lithostatic load and the maximum degree of liquid saturation along the heap profile. If the hydraulic performance of this portion of the heap/lift is adequate, it is reasonable to conclude that the rest of the heap/lift profile will perform just as well or better (Robertson *et al.*, 2013).

The column is irrigated at incremental rates until ponding occurs. The column is then allowed to saturate, and the saturated hydraulic conductivity is measured. Finally, the column is allowed to drain for 2 to 3 days and the residual moisture content is determined by drying the solids and recording the wet and dry masses.

The air permeability is determined at each solution irrigation rate according to the method described by Milczarek *et al.* (2013). At each solution irrigation rate, once steady state has been reached, air is injected at the bottom of the column. The pressure drop over the column is then recorded for several air fluxes, and the pressure drop - flow relationship is used to calculate the air permeability.

Figure 14. Hydrodynamic column apparatus

4.5. Metallurgical leach column tests

Column leach tests are typically performed as part of a heap leach design programme. These include short (1 m) column tests (typically 97 mm, 160 mm, 200 mm or 320 mm ID) where parameters such as crush size, lixiviant acid strength, irrigation rate and curing acid addition may be optimised. Variability tests may be performed to compare the behaviour of different ore lithologies. The heap leach columns represent a cross-section of a commercial heap and simulates the effect of drip irrigation / percolation leaching on the ores and agglomerates. Parameters measured in the short column test programme include reagent consumption and final metal dissolution. This is typically followed by taller (4 m to 6 m tall) columns, representing the height of a single lift of a commercial heap. These are often performed in closed cycle, and provide a more accurate indication of the leach kinetics. It is also important that the taller columns often develop a pH or reagent profile down the length of the bed, resulting in the formation of precipitates and limitations in the supply of reagents (*e.g.* acid), whereas in the shorter columns, there is often an excess of reagent.

Column leach tests were performed on the micaceous ore type in jacketed polypropylene columns controlled at 25°C in both Mintek's short (Figure 15) and tall column facility (Figure 16). Experimental conditions are summarised in Table 6. Typical agglomerate moisture contents are 3% to 7%, whereas the Micaceous Stockpile material had higher initial moisture contents of 11.4% to 12.2%. This can be explained by the very high fines content of the material, which would normally exclude it from being

considered for heap leaching without some sort of pre-treatment. The columns were irrigated in open circuit with dilute sulphuric acid (8-15 g/L). Parameters recorded daily were: (a) feed and drainage pH, (b) feed and drainage redox potential (vs. Ag/AgCl, 3 M KCl), (c) mass, volume, temperature and SG of feed solution, (d) mass, volume, temperature and SG of drainage, (e) daily PLS [Cu] and [Fe] by atomic absorption spectroscopy (AAS), [Fe^{2+}] and [H_2SO_4] by titration.

Slumping of the ore in the column was measured at regular intervals as the decrease in height of the ore bed. The degree of saturation and moisture hold-up of the columns were calculated from a moisture balance over the duration of the experiment, including the masses and volumes fed, the masses and volumes drained, and the moisture added in agglomeration. Upon completion, irrigation was stopped and the columns were allowed to drain. The final cake moisture was determined by drying the solids at ambient temperature. The moisture content and degree of saturation curves were normalised to fit the final moisture determined from the cake moisture. Dissolution profiles and acid consumption profiles were plotted based on assayed head grades, daily solution volumes and copper analyses by AAS.

Table 6. Summary of leach column test conditions

Test	Particle Size	Column ID	Height	Binder	Mass Loaded [1]	Agglom. Moisture	Curing Time	Irrigation Rate	Lixiviant [H_2SO_4]
	(mm)	(mm)	(m)		(kg)	(%)	(days)	(L/m^2/h)	(g/L)
Test 1	-40	160	1	None	26.8	12.1	28	1.4	8
Test 2	-40	160	1	Cement A, 10 kg/t	26.2	12.2	28	6	8
Test 3	-40	160	1	Cement B, 10 kg/t	26.5	11.4	28	6	8
Test 4	-40	160	1	Cement C, 10 kg/t	26.1	11.4	28	6	8
Test 5	-40	320	4	Cement C, 10 kg/t	419.7	11.8	28	6	8
Test 6	-40+0.075	160	4	98% H_2SO_4, 14.3 kg/t	107.2	12.1 [2]	2	6	8
Test 7	-40+0.212	160	4	98% H_2SO_4, 14.3 kg/t	124.7	5.3 [2]	2	6	8-15 [3]

1. *Dry basis*
2. *Curing acid included*
3. *changed to 15 g/L after day 53*

Final solid residues were dried and pulverised. A flux consisting of sodium peroxide and sodium carbonate was added and the mixture was fused in an open flame, followed by dissolution in 20% HCl and analysis by inductively coupled plasma-optical emission spectroscopy (ICP-OES) for the major elements (Mg, Al, Si, Ca, Ti, V, Cr, Mn, Fe, Co, Ni, Cu, Zn and Pb). Mass balances were performed for Cu and Fe. Dissolution profiles were redrawn based on a recalculated head, which incorporates a 100% copper mass balance (i.e. element out / element in) with respect to both solid and solution phases, and these were presented as the definitive values.

Figure 15. Short (1 m) column leach facility

Figure 16. Tall column leach facility

4.6. Mineralogy

Hand-picked agglomerates from each sample were set in resin and examined using the Carl Zeiss Evo MA15 scanning electron microscope (SEM), run at 20 kV accelerating voltage and equipped with back-scattered (BSE) detector and energy dispersive X-ray (EDX) detector. EDX spectra and BSE (back-scattered electron) images of selected areas were used to determine the semi-quantitative chemistry of selected phases where the relationships between phases in the agglomerates were captured and examined. The emphasis was to examine the bonding agents in the ore / cement mixtures. Quantitative X-ray diffraction (XRD) analysis was performed with the Bruker D8 Advance powder diffractometer, with Lynxeye detector and fixed divergence and slits. The instrument utilises Fe-filtered Co-Kα radiation and was run from 3 to 80° 2Θ with a step size of 0.02° 2Θ and a counting time of 3 seconds per step. The technique has a detection limit of 1 to 3 mass %. Phases were identified with Bruker's DIFFRAC.SUITE Eva software package and quantified using Rietveld refinement and the fundamental parameters approach using the Bruker TOPAS software package.

4.7. Materials

The major gangue minerals of the micaceous stockpile material and the feed-cement mixtures are summarised in Table 7. Feldspar, mica, quartz, amphibole and clay, Mg-deficient kaolinite and Mg-bearing sepiolite, were the most prominent phases identified in each of the stockpile samples in amounts ranging from 7.2% to 36%. Trace to minor amounts of chlorite were also detected. Although smectite and chlorite peaks sometimes overlap on XRD, previous iterations of the mineralogy on this sample incorporating QEMSCAN and based on mineral chemistry did not detect smectite and other swelling clays. No phases from the cements were detected by XRD in these mixtures due to the low concentration of cement in the ore-cement-water mixtures, and possibly due to reaction of these phases with the ore.

Table 7. Phases identified in the cement and ore / cement mixtures (mass %)

Phase	Ideal Composition	Cement A (%)	Cement B (%)	Cement C (%)	Ore (%)	Ore + Cement A (%)	Ore + Cement B (%)	Ore + Cement C (%)
Akermanite	$Ca_2MgSi_2O_7$	-	<1	1.1	-	-	-	-
Serpentine	$Mg_3Si_2O_5(OH)_4$	2.6	2.8	4.6	-	-	-	-
Brownmillerite	$Ca_2(Al,Fe^{3+})_2O_5$	14.4	10.1	13.2	-	-	-	-
Calcite	$CaCO_3$	7.5	10.4	8.7	-	-	-	-
Gypsum	$CaSO_4 \cdot 2H_2O$	5.0	3.3	4.0	-	-	-	-
Hatrurite	Ca_3SiO_5	44.2	31.7	41.6	-	-	-	-
Mullite	$Al_{(4+2x)}Si_{(2-2x)}O_{(10-x)}$	14.1	18.0	13.0	-	-	-	-
Quartz	SiO_2	12.3	23.4	13.7	35.6	32.6	33.1	27.2
Chlorite	$(Mg,Fe^{2+})_5Al(Si_3Al)O_{10}(OH)_8$	-	-	-	5.7	4.5	6.1	4.6
Feldspar	$NaAlSi_3O_8$	-	-	-	14.5	17.0	18.3	22.1
Mica	$KAl_2(Si_3Al)O_{10}(OH,F)_2$	-	-	-	24.3	18.1	23.0	21.0
Amphibole		-	-	-	10.1	16.1	12.4	11.7
Clay	$Al_2Si_2O_5(OH)_4$	-	-	-	9.7	11.6	7.2	13.5

- = not detected

Texturally, all three cement samples are similar (Figure 17). Phases identified include hatrurite, brownmillerite, quartz, feldspar, magnetite and mullite. Mullite is well-rounded / spherical in nature, referred to as a pozzolan. Some of the mullite pozzolans are homogenous with no cracks or inclusions, while others display cracks, inclusions and pores. The mullite incorporates trace amounts of Mg, K, Ca, Ti and Fe. Mullite particles are up to 20 µm in diameter. Hatrurite was detected across all samples. This phase is Ca- and Si-rich and occurs most often with brownmillerite. The particles of hatrurite-brownmillerite are sub-rounded to angular in nature and up to 30 µm in diameter. The brownmillerite comprises up to 12% Fe, ~40% Ca and ~12% Al. Further traces of Mg, Si, Mn and S were also detected in brownmillerite across the samples. Quartz occurs in both angular to sub-rounded particles in association with mullite, up to 20 µm in diameter. The average compositions of phases identified are shown inTable 8.

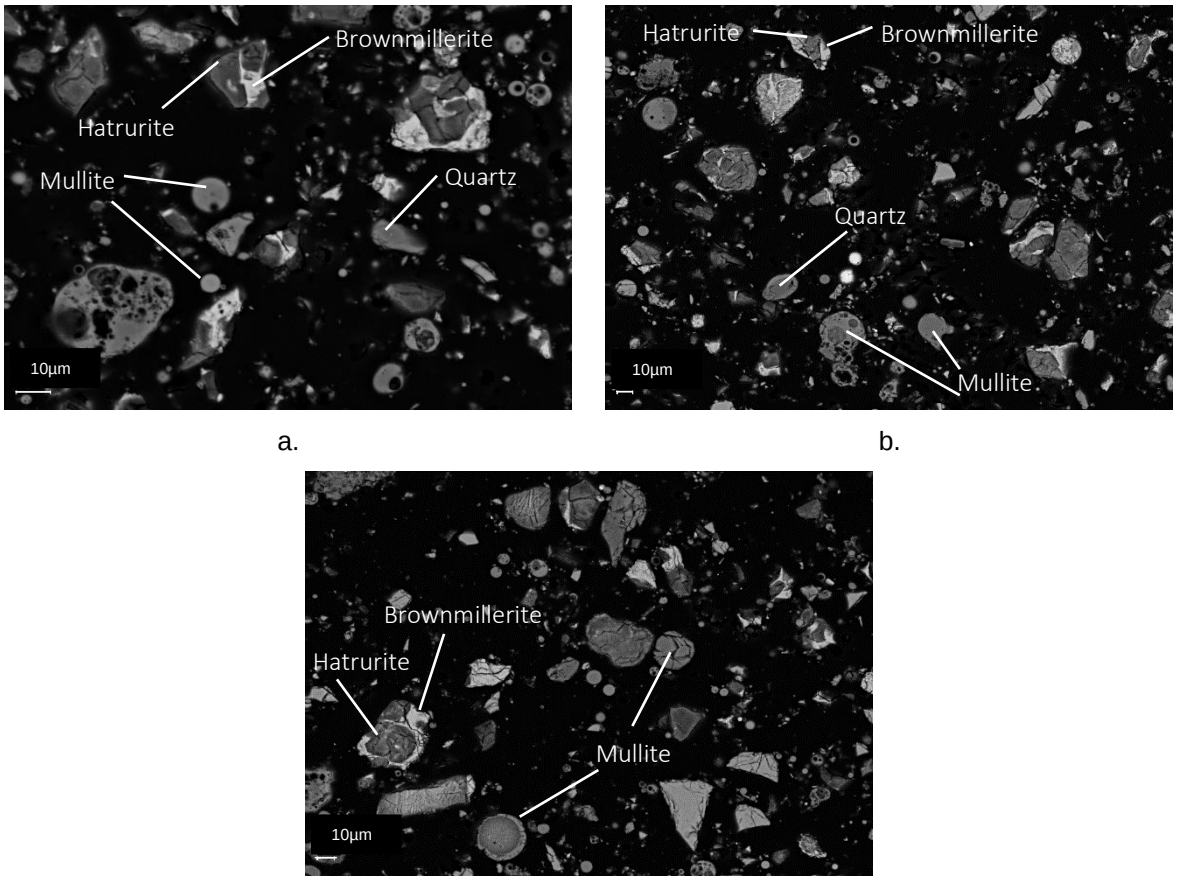

Figure 17. Back-scattered electron images from samples (a) Cement A, (b) Cement C (c) Cement B. Scale bar represents 10 µm on each image.

Table 8. Average compositions (normalised wt. %) of phases in the cement samples, as determined by SEM-EDS. n = number of analyses.

Phase	n	O	Mg	Al	Si	P	S	K	Ca	Ti	Mn	Fe
Anorthite	5	40.8	5.3	8.7	14.2	-	1.0	-	29.5	0.6	0.6	-
Brownmillerite	16	33.5	2.2	10.7	2.8	-	0.5	-	39.1	1.0	1.3	10.1
Mullite	22	48.5	1.2	21.9	23.0	-	-	1.2	2.3	1.3	-	1.7
Hatrurite	21	37.7	1.8	1.6	13.9	0.7	1.6	-	42.0	0.8	0.5	1.3
Quartz	8	53.2	-	1.3	46.2	-	-	-	1.0	-	-	-

The major copper minerals and deportments in the micacous stockpile sample are summarised in Table 9. Copper was primarily present as by mica (58%), malachite (9.6%), wad (13.4%), bornite (6.5%), chalcocite (5.6%), pseudomalachite (3.6%) and chrysocolla / shattuckite (1.6%). Manchisi *et al*. (2019) describes that Zambian copper micas, which would normally not be acid soluble at ambient conditions, can be dissolved in columns if the ore is pretreated with acid curing. However, in the leach columns a substantial proportion of mica must have dissolved to generate the copper dissolutions of above 80%. This is thought to result from a combination of acid curing, together with the long leach times in which the copper mica is in contact with the leach solution compared with a typical stirred tank leach residence time. Although the heap leach results were positive in terms of total recovery, this was offset in the initial test work programme by the poor solution permeabilities, which made heap leaching of this material marginal. However, the high copper dissolutions, combined with the improved permeability obtained with binder makes heap leaching of these and similar mica ores a more attractive option.

Table 9. Copper deportment

Minerals	Mass distribution (%)
Cuprite	0.02
Tenorite	0.02
Malachite	9.60
Chrysocolla/Shattuckite	1.61
Pseudomalachite	3.55
Libethenite	0.06
Cu-Co-Wad	13.38
Brochantite	0.25
Chalcocite	5.62
Covellite	0.02
Bornite	6.49
Chalcopyrite	0.22
Goethite	0.44
Cuchlorite	0.52
Cu Mica	58.19
Total	**100**

5. RESULTS AND DISCUSSION

5.1. Part I – The effect of physical properties such as porosity and particle size distribution on the saturated hydraulic conductivity and residual moisture hold-up

The saturated hydraulic conductivity in the bed was modelled with packed bed theory, utilising a modified version of the Kozeny-Carman equation to model the pressure drop – flow relationship, and replacing the particle diameter with a hydraulic radius. The hydraulic radius is calculated from the total bed porosity, and the surface area of the bed, assuming spherical particles with a range of diameters. The residual moisture is related to particle size distribution, and particularly the percentage of sandy (-4.75 mm) particles in the bed. This is explained by the Bond number (B_o), relating the ratio of capillary to gravitational forces acting on the water droplets.

5.1.1. Particle size analysis

A number of crushed ores were selected which could be fitted with the GGS power relationship (equation 15) and are plotted in Figures 18, 19 and 20 for three top-sizes: -12.5 mm, -25 mm and -50 mm. The GGS approach used by Cherkaev (2019) provided a good fit for the -12.5 mm crush size, but not for the -25 mm and -50 mm crush sizes. In general, the GGS power law provided a poor fit for most of the samples in Appendix A. However, a good fit could be obtained by dividing the curve into 2 parts as indicated in Figure 21. The two parts can then be fitted with a polynomial and a power law, respectively. The surface area can then be calculated by summation of the integrals over the two parts (equation 24). The fitting parameters A and B are provided for the polynomials ($y = Ax^2+Bx+C$) and the parameters a and λ for the power fits ($y = ax^{\lambda}$) in Appendix A. A number of samples in Appendix A fitted well with the GGS distribution (which is a power law), in which case only the parameters a and λ are given.

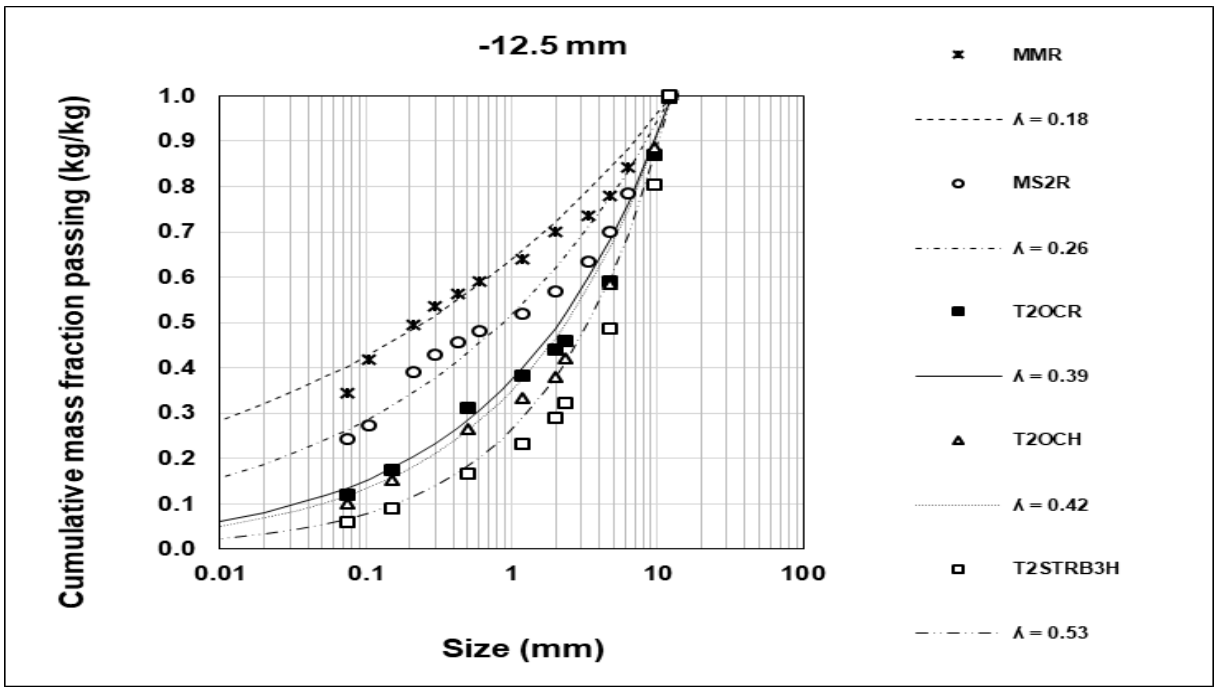

Figure 18. GGS fit -12.5 mm

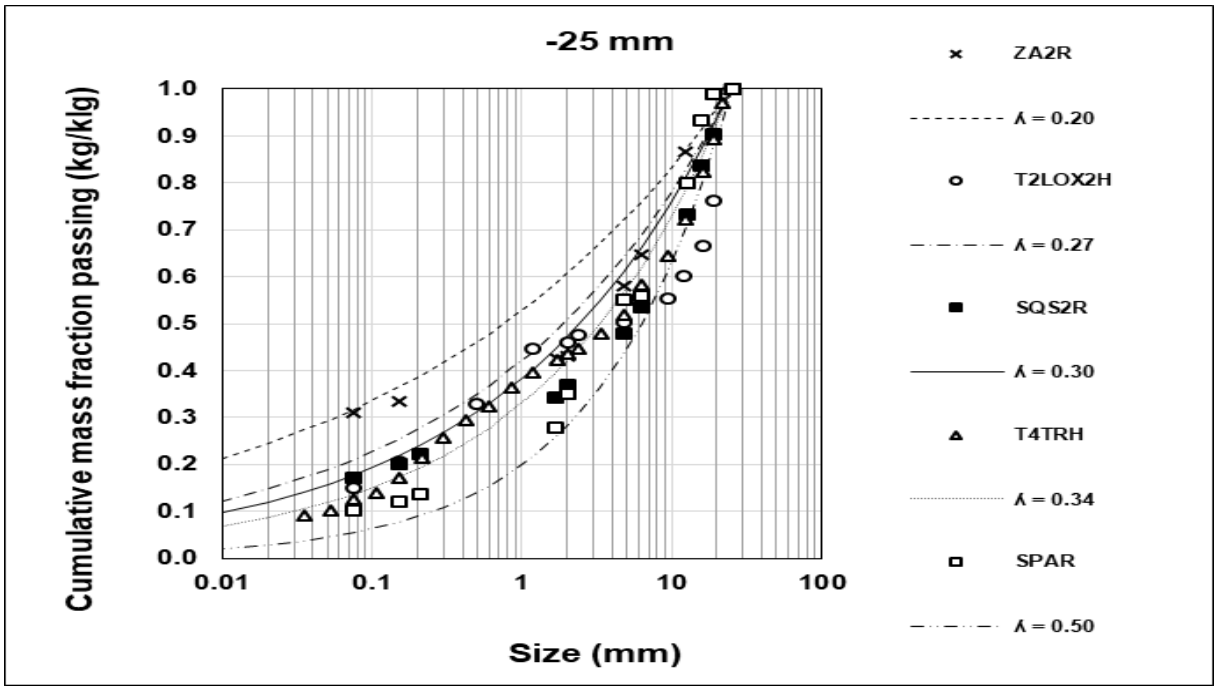

Figure 19. GGS fit -25 mm

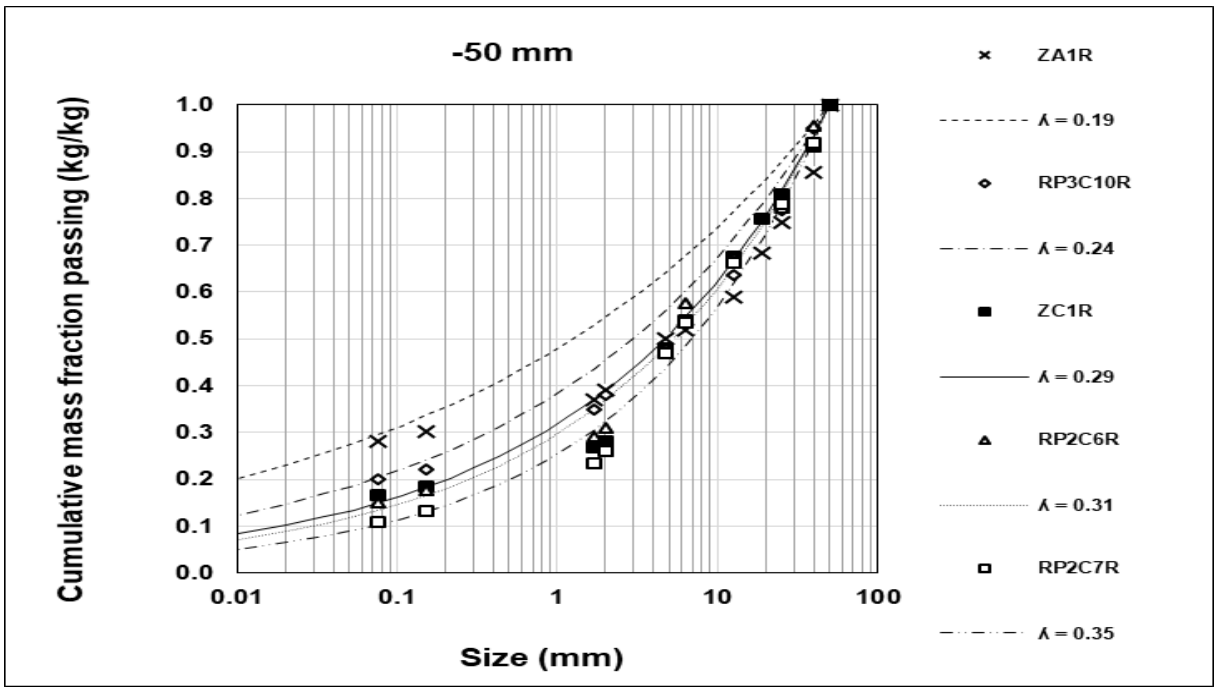

Figure 20. GGS fit -50 mm

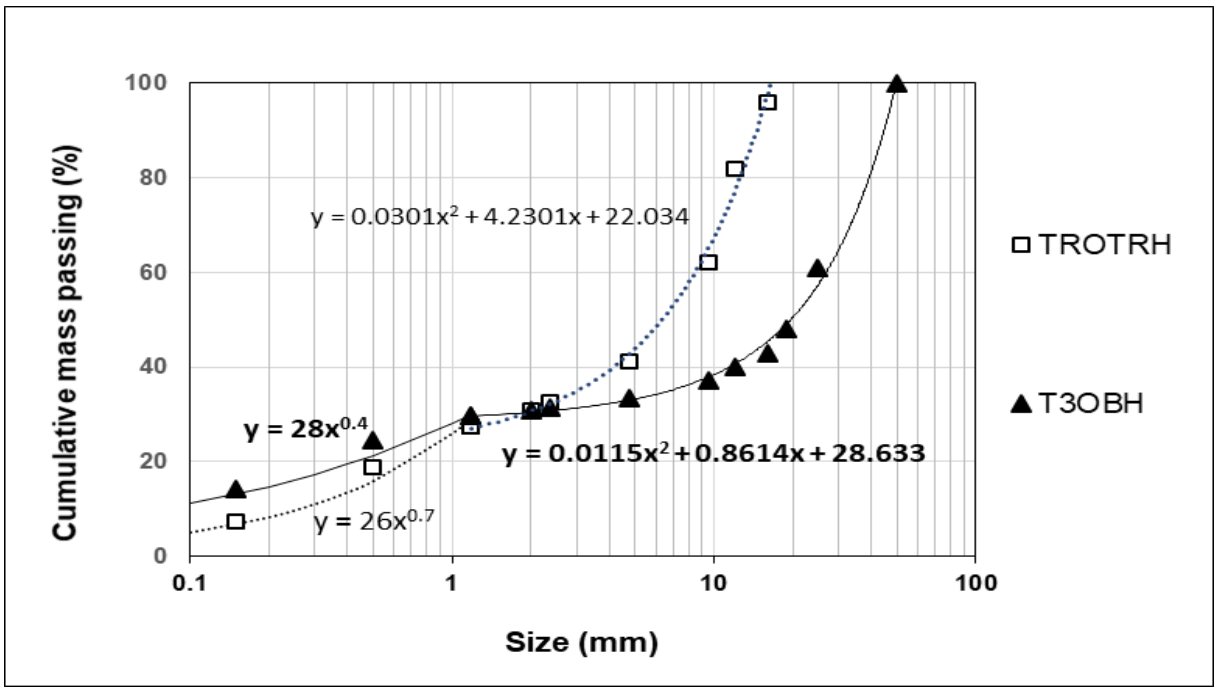

Figure 21. Examples of modelling the PSD with a second order polynomial and power law

5.1.2. Surface area

Surface areas were calculated for all the samples in Appendix A using equation (24). D_{min} is not exactly known since the lowest sieve-size used in the laboratory is typically 35 µm or 75 µm. D_{min} can also not be specified as zero, since the power law is asymptotic to zero. Also λ in equation (16) is in most cases less than one, with the result that the second term in the integral has a positive coefficient and a negative power. Therefore, if D_{min} is specified as zero, this will lead to an infinitely large value for the integral. Therefore is it necessary to specify a value for D_{min}.

Cherkaev (2019) proposed that very small particles will likely stick to larger particles, form lumps, or be suspended in the solution. Hence it is unlikely that very small particle size diameters will contribute individually to the surface area exposed to the liquid.

Warren (2021) also proposes that, at some minimum size, the particles will begin to bind together due to *adherence*, where fine particles stick to mechanical (or in this case larger rock) surfaces; or *agglomeration*, where the compression forces exerted on the solid particles cause them to stick together. During mixing or blending, the smallest particles will often agglomerate together due to bonding forces between molecules of individual particles, electrostatic attraction or capillary forces, for example, where moisture within particles for a liquid bridge and binds them together.

The approach taken in this study was to calculate the surface areas for a range of D_{min}, starting with the lowest value of D_{min} = 0.002 mm (equivalent to the clay fraction) and to study the effect of D_{min} on the calculated parameters such as tortuosity, in order to obtain a physically realistic result.

5.1.3. Hydraulic radius

Equation (9) was used to calculate the hydraulic radius – tortuosity ratios from the measurements of saturated hydraulic conductivity (*Ks*) performed in the compression and hydraulic conductivity tests summarised in Appendix A. The ratio r_H / τ is plotted in Figures 22 (hydrodynamic column tests) and 23 (stacking tests) on the secondary y-axis. The Unified Soil Classification System used in engineering and geology corresponds to US Standard Sieves and defines sand as particles with a diameter between 0.074 and 4.75 mm. ISO 14688 grades sand as fine (0.063 to 0.2 mm), medium (0.2 to 0.63 mm), and coarse (0.63 to 2 mm). The author therefore classified the particle size distributions as clay + silt (-0.075 mm), sand (-2+0.075 mm), very coarse sand (-4.75+2 mm) and gravel (-50+4.75 mm). These are plotted on the primary y-axis as stacked bars. The data has been arranged in order of increasing fines content on the x-axis (irrespective of ore type) for comparison. The ratio r_H / τ appears to correlate visually with the +4.75 mm content, as the hydraulic radius is inversely proportional to the surface area, which increases with fines content. As a result, the primary y-axes of Figures 22 and 23 are inverted to show this relationship visually. For the compression tests (Figure 23) at lower fines content, r_H / τ appears to correlate visually with the +4.75 mm fraction, whereas at higher fines content, r_H / τ appears visually to correlate with the +2 mm fraction.

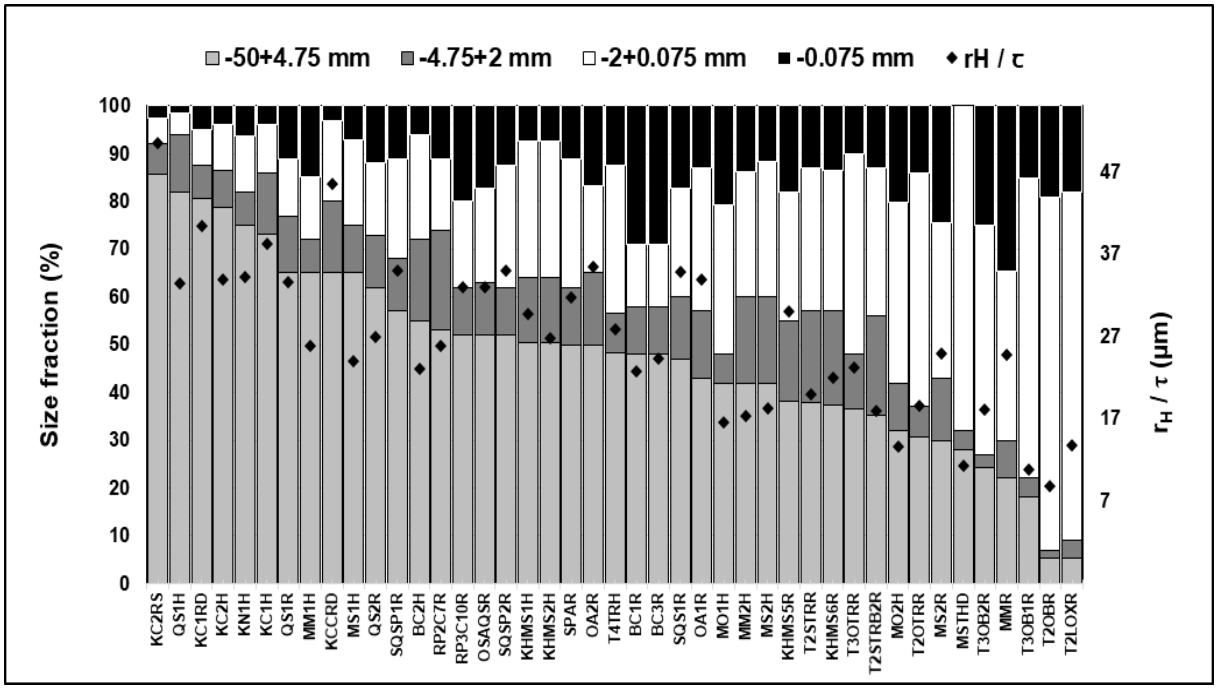

Figure 22. Hydraulic radius as a function of PSD for column test data

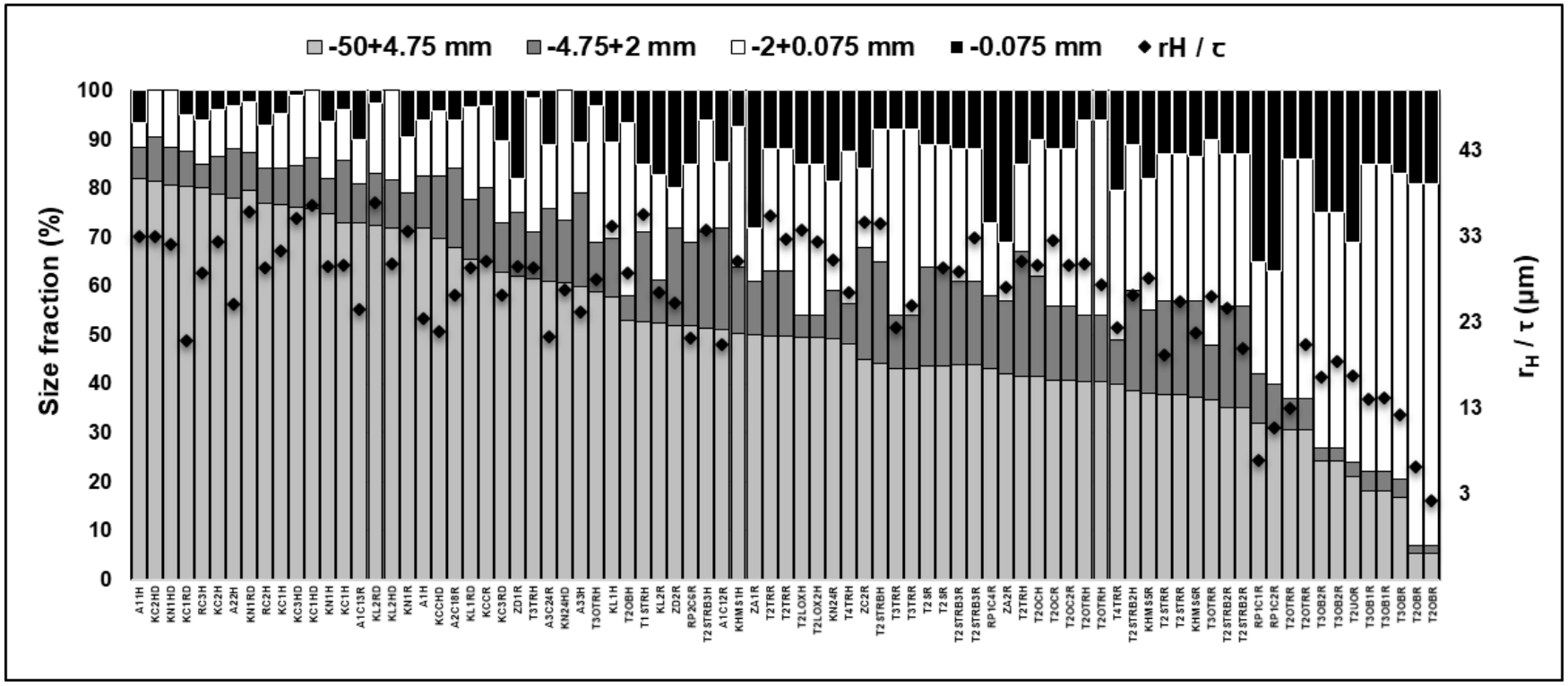

Figure 23. Hydraulic radius as a function of PSD for compression test data

5.1.4. Tortuosity

According to Carman (1937), the tortuosity of fully saturated, uniform, spherical, porous solids is around 2. A tortuosity of 1.4 was also reported by McDonald (1991) for spherical particles. Tortuosities of < 5 were reported by Dullien (1992) for consolidated rocks and soils. Tortuosities of between 1.4 and 2 were reported by Clennel (1997) for unsupported aggregates, and 1.5 for sand by Espinoza-Andaluz *et al.* (2017).

Surface areas for the samples in Appendix A were calculated for a D_{min} between 0.002 mm and 0.2 mm. The theoretical hydraulic radius (r_H) was calculated by dividing the experimentally determined porosity by the calculated surface area. The ratio r_H / τ was also calculated independently from the K_s measurements and equation (9). This relationship is shown in Figures 24 to 26, for D_{min} = 0.002 mm, 0.02 mm and 0.2 mm, respectively. The tortuosities may be calculated from the slopes of the graphs. A least squares fit was performed for each D_{min} with the column and compression test taken as a single set of data (using intercept = 0). However, rather than a single value, one would expect a range of tortuosities within the data set, based on variations in the shapes of the rock, top-size, fines segregation and agglomeration.

For D_{min} = 0.002 mm, the least squares fit yielded a slope (tortuosity) of 0.21. Slopes of 0.2 times and 1.8 times (-80% and +80%) the slope of the linear regression of the full data set, respectively, yield tortuosities of between 0.04 and 0.37 and include 76% of the data points. This range of tortuosities suggests that a D_{min} of 0.002 mm is most likely too small, since this would mean tortuosities below 1, which are physically unrealistic. For a D_{min} of 0.02 mm, the least squares fit gives a slope (tortuosity) of 0.71. Slopes of 0.2 times and 1.8 times (-80% and +80%) the slope of the linear regression, respectively (equivalent to tortuosities of between 0.14 and 1.28), include 79% of the data points. Hence a D_{min} of 0.02 mm also appears physically unrealistic. Finally, a D_{min} of 0.2 mm yields a least squares regression slope of 2.96, and a range of between 1.48 and 4.44 (73% of the data points), if one takes slopes equivalent to 0.5 and 1.5 times (-50% and +50%) the slope of the linear regression. Since τ = 1.4 is the theoretical minimum for an ideal packing of equisized spheres, a D_{min} of 0.2 mm appears the most realistic. It is also similar to the optimal D_{min} of 0.27 mm reported by Cherkaev (2019).

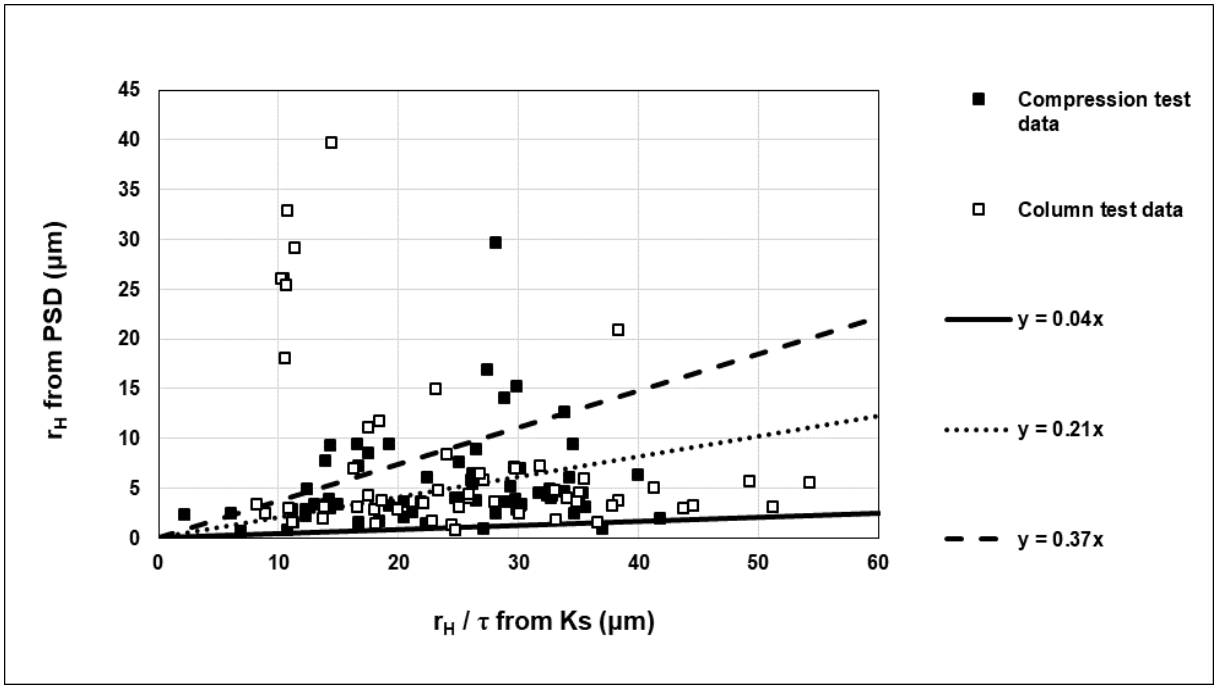

Figure 24. Hydraulic radius from PSD vs. hydraulic radius from Ks (D_{min} = 0.002 mm)

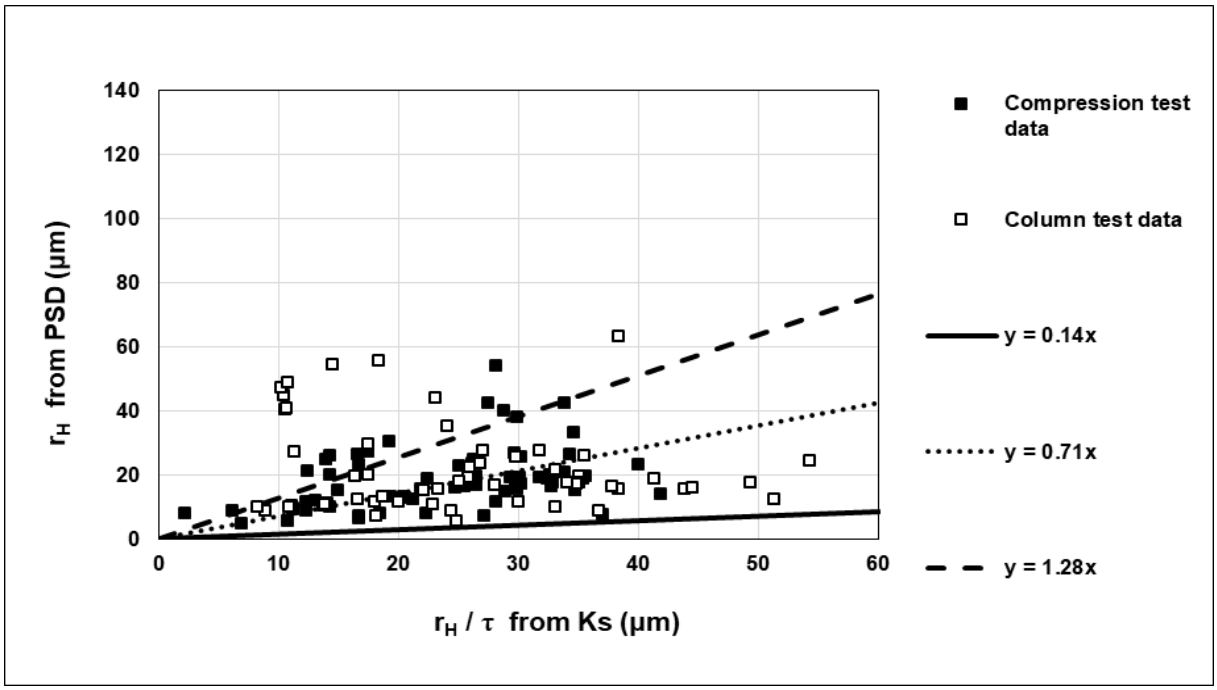

Figure 25. Hydraulic radius from PSD vs. hydraulic radius from Ks (D_{min} = 0.02 mm)

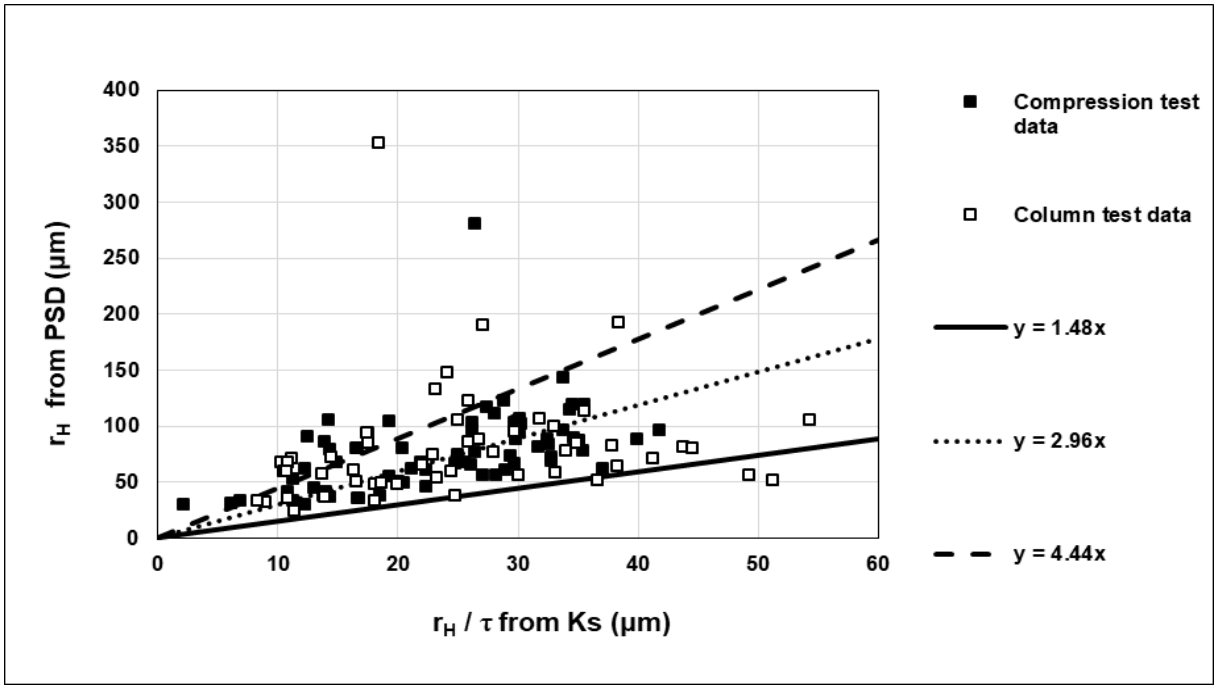

Figure 26. Hydraulic radius from PSD vs. hydraulic radius from Ks (D_{min} = 0.2 mm)

5.1.5. Residual moisture

Values for the residual bed moisture content are presented in Figures 27 and 28 for the data derived from the column tests and compression tests, respectively. The particle size distributions as clay + silt (-0.075 mm), sand (-2+0.075 mm), very coarse sand (-4.75+2 mm) and gravel (-50+4.75 mm) and these are plotted on the primary x-axis as stacked bars (Figures 27 and 28). Plotted on the secondary y-axis is the residual bed moisture content. The data has been arranged in order of increasing fines content (irrespective of ore type) for comparison.

As indicated in Figures 27 and 28, there appears to be a trend of increasing residual moisture content with increasing sand and fines (-4.75 mm) content for both the compression tests and column tests, which is to be expected as finer particles present larger surface areas per unit mass. However, at higher sand and fines contents (> 50% -4.75 mm), the residual moisture appears to correlate more with the -2 mm fraction for the compression tests, the reason for which is not clear. The residual moisture content is important as it determines the water loss to the heap leach residues, which is significant in water-scarce regions such as the Chilean desert. The water losses in a heap leach operation typically comprise the sum of the contributions from evaporation, bleed streams and water contained in the residues. If one assumes current water costs in Chile of between 2 and 6 USD / m^3 and a residual moisture of between 5% and 18%, this will translate to a water loss of between 0.1 and 1.3 USD per tonne of ore treated. In addition, the residual moisture may also contain other valuable elements such as acid, chloride and copper (Lopez, 2021). However, water losses associated with heap leaching is

still lower compared with flotation, where finely-ground flotation tailings contain substantially higher levels of moisture (22% to 35%).

The surface areas (calculated from equation (24)) with D_{min} = 0.2 mm and the residual moisture content data show a linear relationship (Figure 29) for the column tests and to a lesser extent for the compression tests. Also shown are the 90% confidence intervals on the slopes of the linear regression curves. By visual inspection, the column data appears to fit a linear trend better than the compression test data. The column has a perforated base, whereas the compression test cell has a plastic perforated disc lying on top of a steel base with a single central drainage hole. Hence it is possible that the perforated base of the column may have provided a more even and better drainage than the compression cell. This is also borne out by the fact that the compression test data in Figure 28 generally exhibit higher residual moistures per surface area, suggesting that drainage was not as complete as in the columns and may also be the result of compression tests compacting the material and creating more saturated spaces than the columns, retaining more moisture.

Cherkaev (2019) demonstrated a linear relationship between relative moisture content and relative surface area (*i.e.* the ratio between the surface area and water contents and those of a reference sample with a GGS ʎ = 0.75 and D_{max} = 26.5 mm). He found that the relationship between relative specific surface area and the relative water content was almost constant for all blends and for various choices of D_{min}, although his work was limited to a D_{min} of 0.13 mm, 0.27 mm and 0.53 mm (D_{max} / D_{min} = 200, 100 and 50). He proposed that -0.27 mm particles can be classified as the 'critical particle size' below which particles would be agglomerated or suspended, since a D_{min} of 0.27 mm provided the best fit of the three D_{min} values used.

Cherkaev's (2019) approach was also used to determine plots of relative moisture content versus relative surface area (Figure 30). Cherkaev's sample with top size 26.5 mm and GGS ʎ = 0.75, with residual moisture of 0.06 m^3/m^3 was used as reference. The surface areas were calculated for Cherkaev's samples using equation (24), a D_{min} of 0.2 mm, and the values of λ and bulk densities reported by Cherkaev. The surface areas and residual moisture contents were divided by the values of the reference sample to obtain the relative values. Similarly, the relative surface areas and relative residual moistures were determined for the samples in this thesis, using a D_{min} of 0.2 mm, and are plotted in Figure 30. The result is not as linear as the plots obtained using Cherkaev's data (R^2 = 0.52 versus R^2 = 0.96). This is perhaps due to the greater heterogeneity in the sample set in this study, compared with the study of Cherkaev (2019), where samples were reconstituted to fit a GGS particle size distribution with a single top-size. The data in this study comes from many different materials, whereas Cherkaev's sample came from one material, not necessarily close in mineralogy. Furthermore, the nature of particle surfaces and their interaction with solution is determined by contact angle, crystal morphology and shape of particle, which is expected to vary within the various materials.

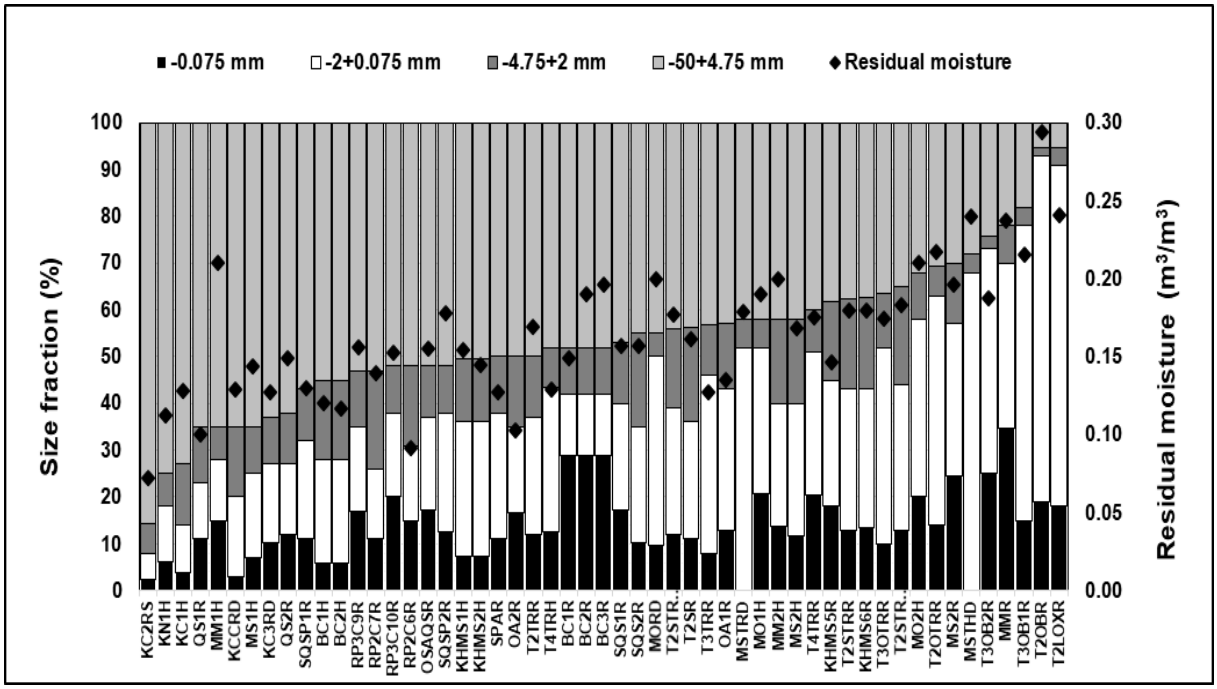

Figure 27. Residual moisture content as a function of PSD for column test data

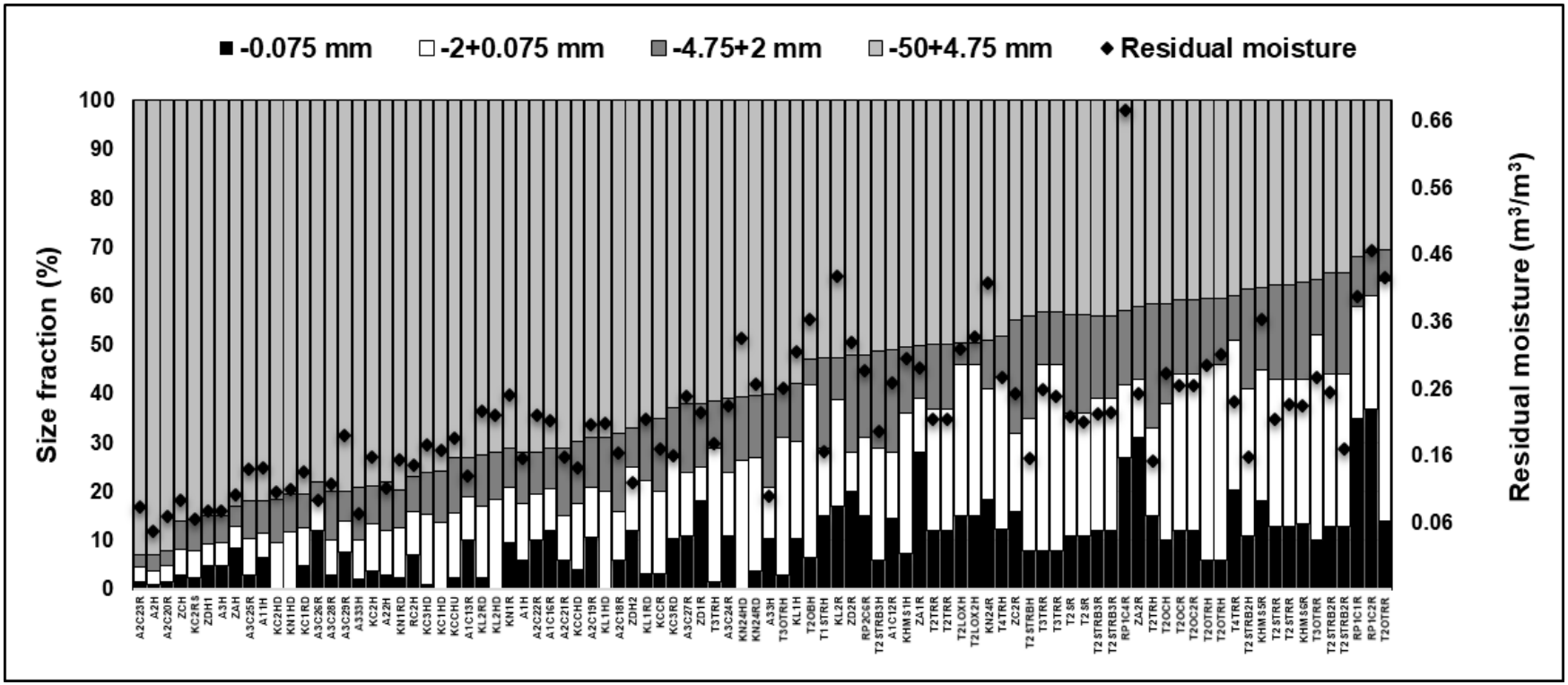

Figure 28. Residual moisture content as a function of PSD for compression test data

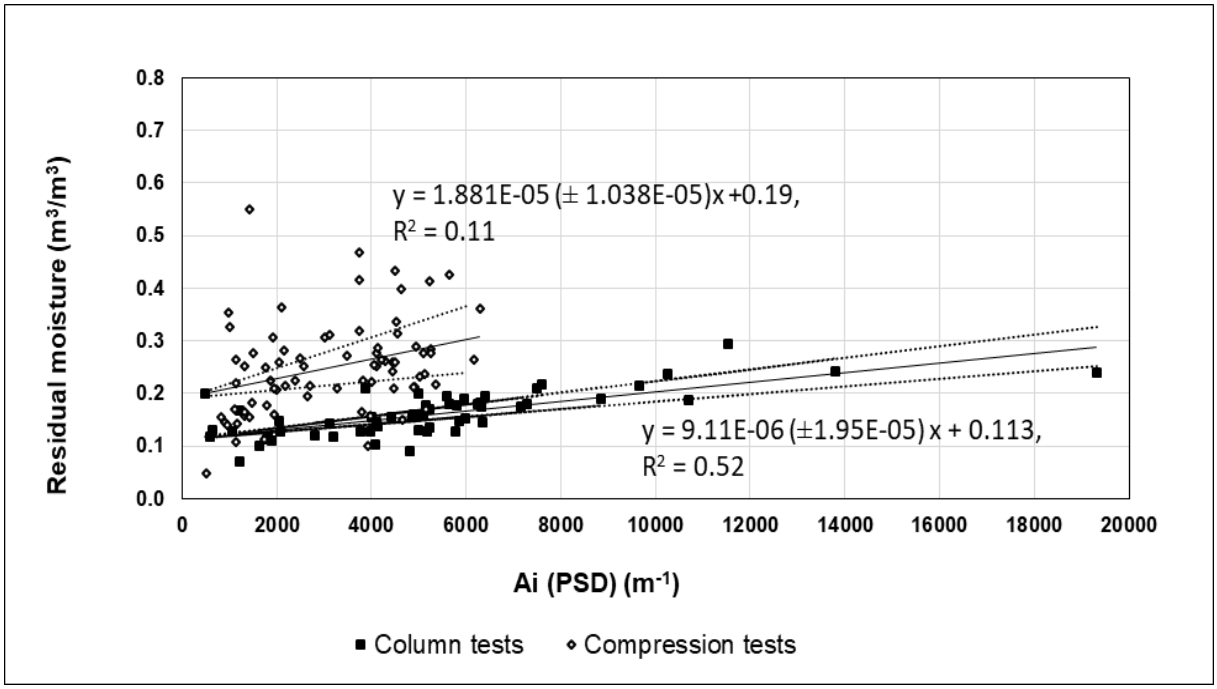

Figure 29. Residual moisture versus surface area (D_{min} = 0.2 mm)

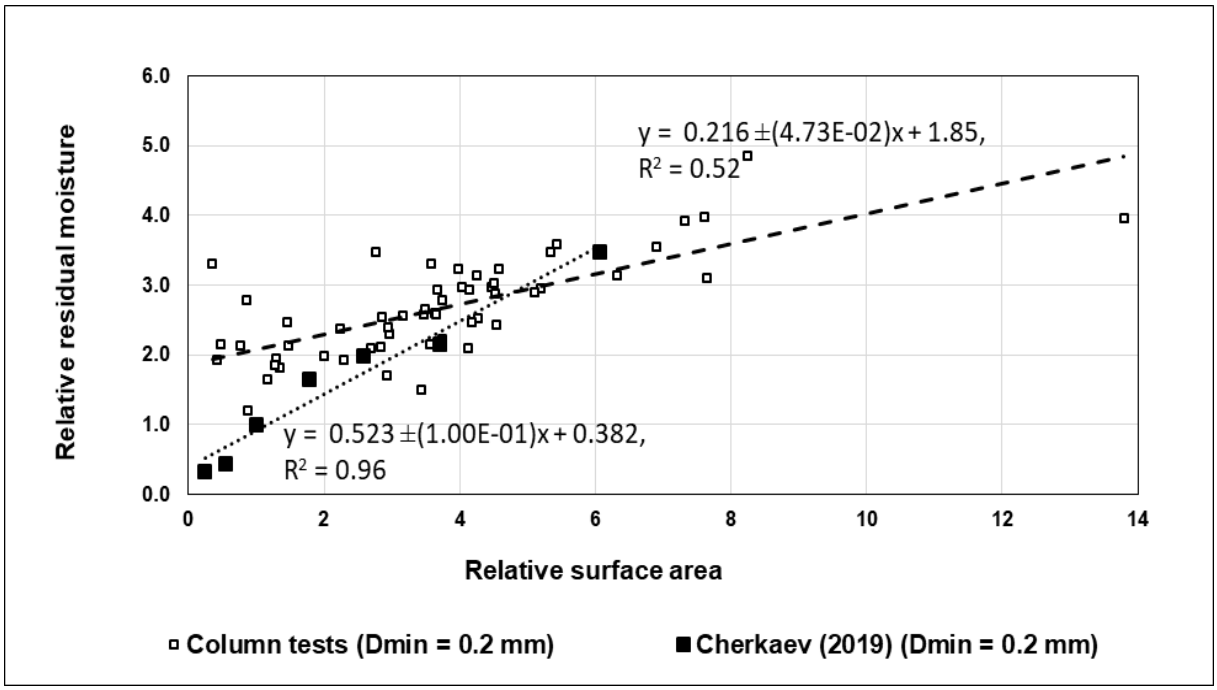

Figure 30. Relative residual moisture versus relative surface area

5.1.6. Bond number

The relationship between residual moisture and PSD can also be interpreted in terms of the Bond number. The ratio between gravity to capillary forces is given by the Bond (B_o) number defined by equation (40). Since the ore particles in a heap cover a range of sizes, the Bond number varies from significantly below 1 to significantly above 1 over the size range, where *l* is the characteristic length. Defining *l* as the hydraulic radius, the Bond number may be expressed in terms of the particle diameter (D_p) for a bed of uniform diameter spheres (Ilankoon *et al.*, 2017, Saez and Carbonell, 1985), where σ is the surface tension of the liquid-air interface and *g* is the gravitational constant:

$$\mathrm{Bo} = \frac{\rho\, g\, l^2}{\sigma} = \frac{\rho\, g\, {D_p}^2 \varepsilon^2}{\sigma(1-\varepsilon)^2} \tag{40}$$

Assuming a bed of spheres of uniform diameter with a porosity of 0.4 m^3/m^3, a water density of 998 kg/m^3 and a surface tension of 0.072 N/m^2 (20ºC), the Bond number equals 1 at a diameter of about 4 mm (Note the maximum porosity of uniform sized spherical cubic packed grains = 0.4764, independent of grain size (Glover, 2023)). A low value (typically less than 1) indicates a regime where surface tension dominates. This corresponds closely to the classification of -4.75 mm used to describe the coarse sand fraction. As the particle diameter increases, the Bond number increases by the square of the particle diameter, implying that gravity forces will rapidly become more dominant with increasing particle diameter, such that the ratio between gravity and surface forces is close to 10 at a particle diameter of 10 mm. At particle diameters below 4 mm, the Bond number will quickly decrease, such that a ratio of close to 0.1 is achieved at 1 mm. Hence the correlation between residual moisture and the proportion of sand fraction can be explained by the dominance of surface forces below 4 mm. The interstitial spaces associated with the smaller particles induces strong capillary action, which retain more moisture.

Hence, in a hypothetical scenario where the bed is bi-modal or segregated into sections comprising primarily sandy (-4.75 mm) particles on the one hand, and coarser particles on the other hand, the sand will present regions of larger surface area and smaller interstitial pore spaces, increasing the moisture in proportion to the -4.75 mm content. This may be applicable, for example, if one views the bed as a “filled skeletal” structure (Zhao *et al.*, 2021), comprising clumps of finer particles filling the voids between coarser rocks. At low fines content, the “skeletal structure” is partially filled, leaving larger intra-particle voids where gravitational forces dominate. At higher fines content, the “skeletal structure” is completely filled, resulting in less large pores, so that capillary forces dominate.

5.2. Part II – Modelling of unsaturated flow through the bed with traditional soil capillary models

The unsaturated flow in the bead, measured in the hydrodynamic column tests, is modelled with traditional soil capillary models such as the van Genuchten-Mualem (VGM) and Brooks Corey (BC), in order to derive the hydraulic conductivity function (HCF), which represents the relative hydraulic conductivity (K_r) against the dimensionless effective saturation (S_e), and the air conductivity function (ACF). It was found that the HCF could be modelled with a modified version of the VGM function, incorporating an inflection point, above which the moisture content kept on increasing without a corresponding increase in hydraulic conductivity. The point of inflection was found to correspond with the air entry point (the point of moisture at which air permeability drops off).

5.2.1. Methodology for fitting the HCF

The hydraulic conductivity functions generated for the hydrodynamic column tests are mostly S-shaped curves if the measured K_s data point is included in the data set (Appendix B). This type of curve cannot be modelled by the conventional BC or VGM functions, except if K_s is made a fitting parameter (Mohanty *et al*., 1997; Luckner *et al*., 1989). However, instead of modelling the data as a continuous S- or J-curve, the author proposes a discontinuous J-curve to be the most realistic. This approach uses either a BC function (equation 41) or a VGM function (equation 42) to fit the data at lower moisture contents, up to $K_r = 1$ at the point of discontinuity (defined as $S_e = S_{e\ max}$). Above the point of discontinuity, K_r is defined as being equal to 1. Two examples of this approach are plotted in Figures 31 and 32, showing both the BC and VGM models for samples KC2RS and EB.

$$K_{r\_BC} = \left(\frac{S_e}{S_{e\ max}}\right)^{n_p} \text{ , } S_e < S_{e\ max} \tag{41}$$

$$K_{r\_VGM} = \left(\frac{S_e}{S_{e\ max}}\right)^{\Upsilon}\left[1-\left(1-\left(\frac{S_e}{S_{e\ max}}\right)^{\frac{1}{m}}\right)^{m}\right]^2 \text{ , } S_e < S_{e\ max} \tag{42}$$

$$K_r = 1 \text{ , } S_e \geq S_{e\ max} \tag{43}$$

The data was fitted as follows: First the experimentally determined values of K_r were plotted against S_e. By visual inspection, the value of $S_{e\ max}$ was then estimated, *i.e.* the point at which the function is expected to cross $K_r = 1$. In the case of the VGM function, Υ was initially set to 0.5. The MS Excel "solver" function was then used to solve either n_p (BC) or m (VGM) by minimising the sum of the square of errors between the actual data points and the calculated data points. The actual value of $S_{e\ max}$ was then read off from the graph and used for the next iteration. Subsequently changing the value of Υ did not markedly improve the fit for the VGM curve, hence $\Upsilon = 0.5$ was kept.

The moisture content keeps on increasing above the point of discontinuity without a further increase in K_r. This suggests the presence of "dead voids" or poorly connected macro-voids, which fill up at higher moisture contents but do not create additional flow channels. Most previous authors ascribe the discontinuity in the HCF curve to a transition to gravity-controlled flow or a transition between micro-

and macro-porosity (Guzman *et al.,* 2008; Russo, 1988; Gerke and van Genuchten, 1993). However, if this was the case, one would expect an upwards trend in K_r *after* the transition to macro-pores (at the point where K_s of the fine-grained fraction is exceeded), since the gravity-controlled portion has a higher K_s. The present data further suggests that the flow is entirely capillary-controlled up to the point of discontinuity, since the data can be described by a single VGM-function. It appears the agglomerates act as a single phase, rather than an interpolation of a sum of VGM-functions. The moisture content corresponding to $S_{e\,max}$ is defined as θ_{max}. (θ_{max} can be derived from $S_{e\,max}$ and equation 25a since θ_r and θ_s are known).

Plotted in Figures 33 and 34 are the air conductivity curves. The modified VGM model (equation 33) was used to fit the air conductivity curves, and $K_{g\,max}$ and θ_{aep} were derived from the data.

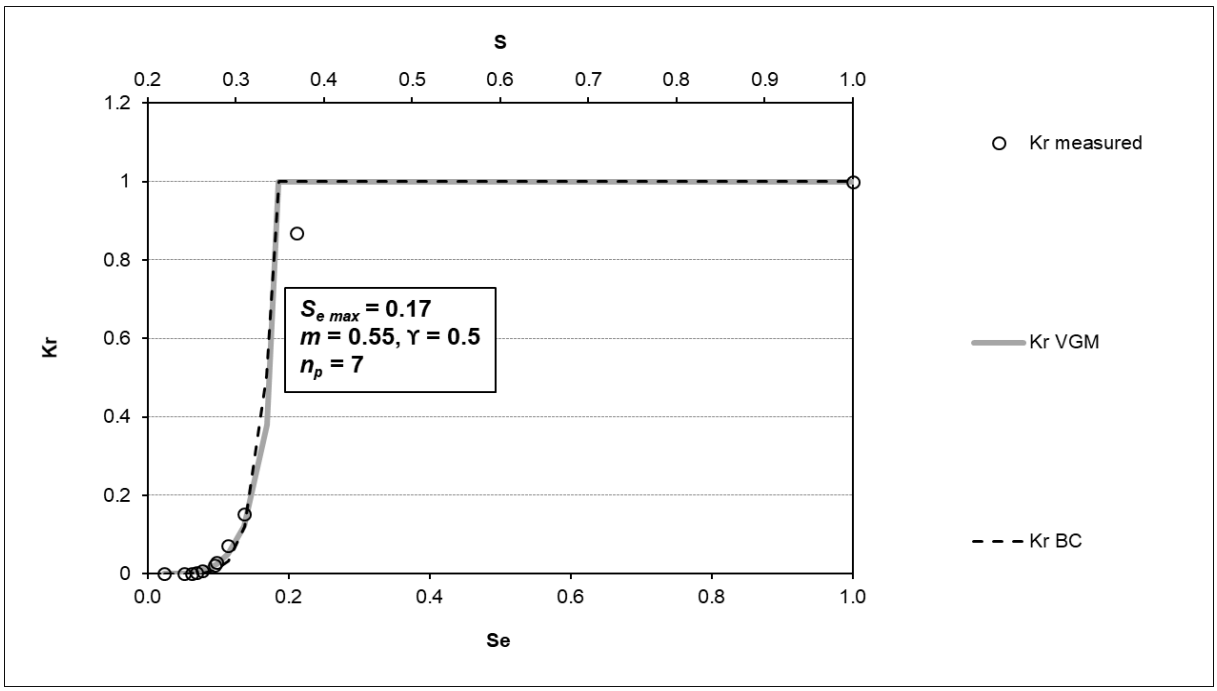

Figure 31. Hydraulic conductivity function (KC2RS)

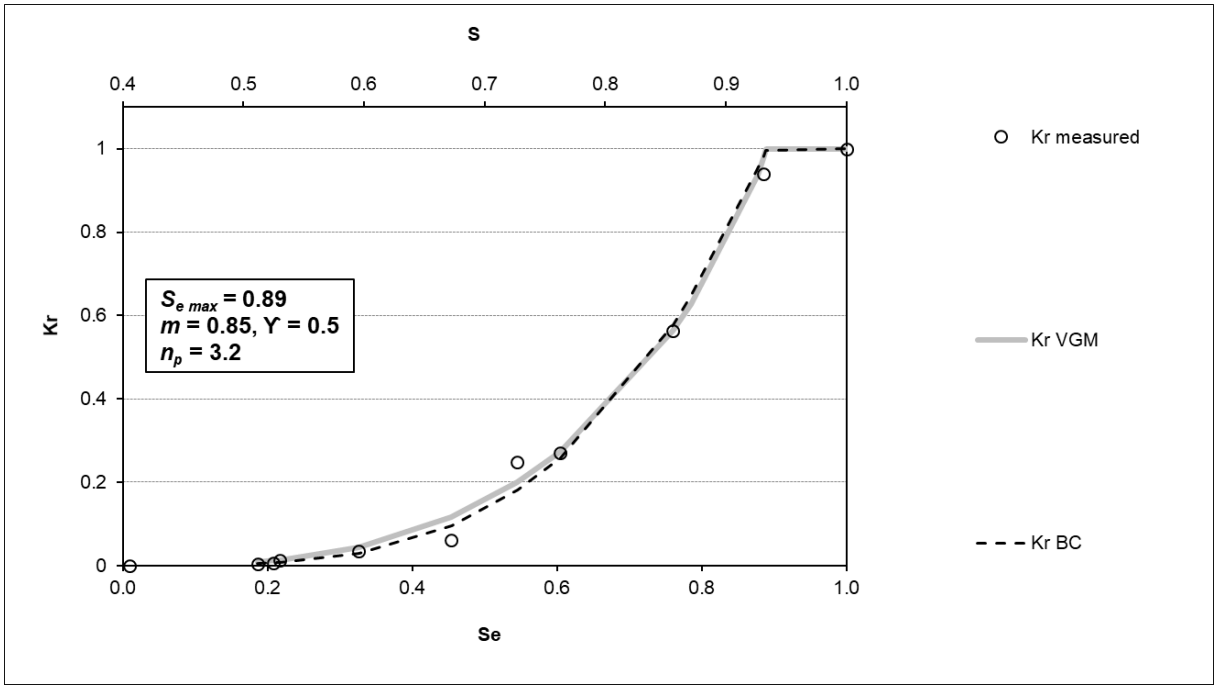

Figure 32. Hydraulic conductivity function (EB)

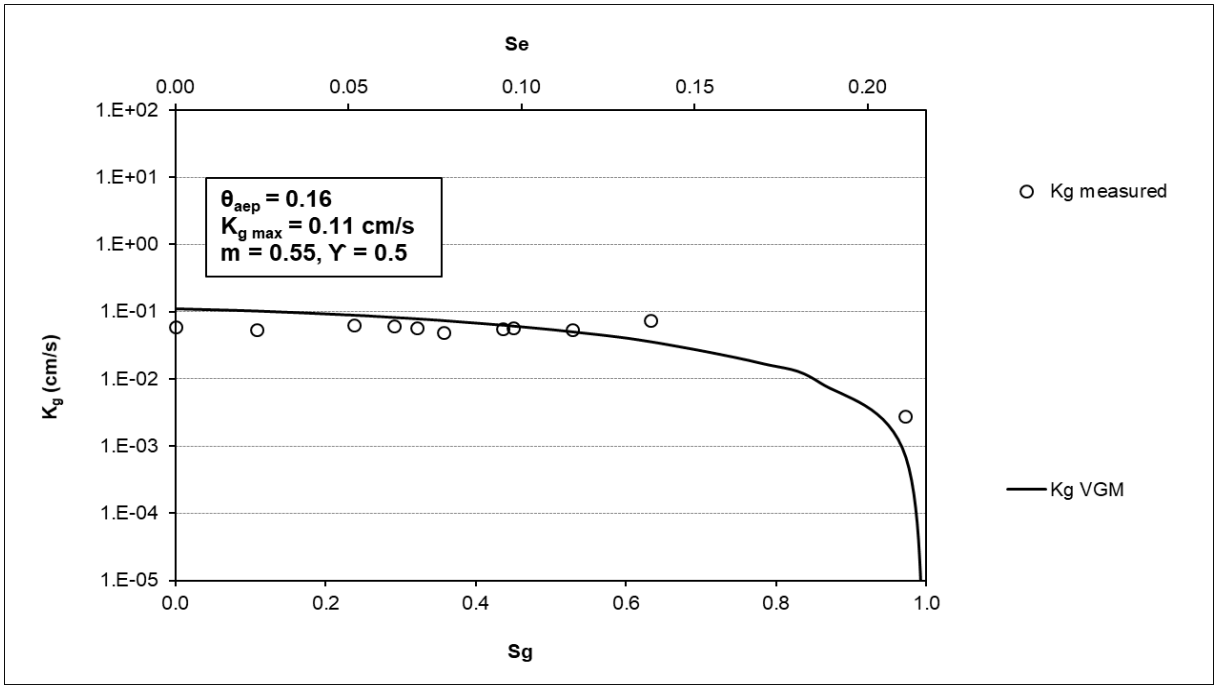

Figure 33. Air conductivity function (KC2RS)

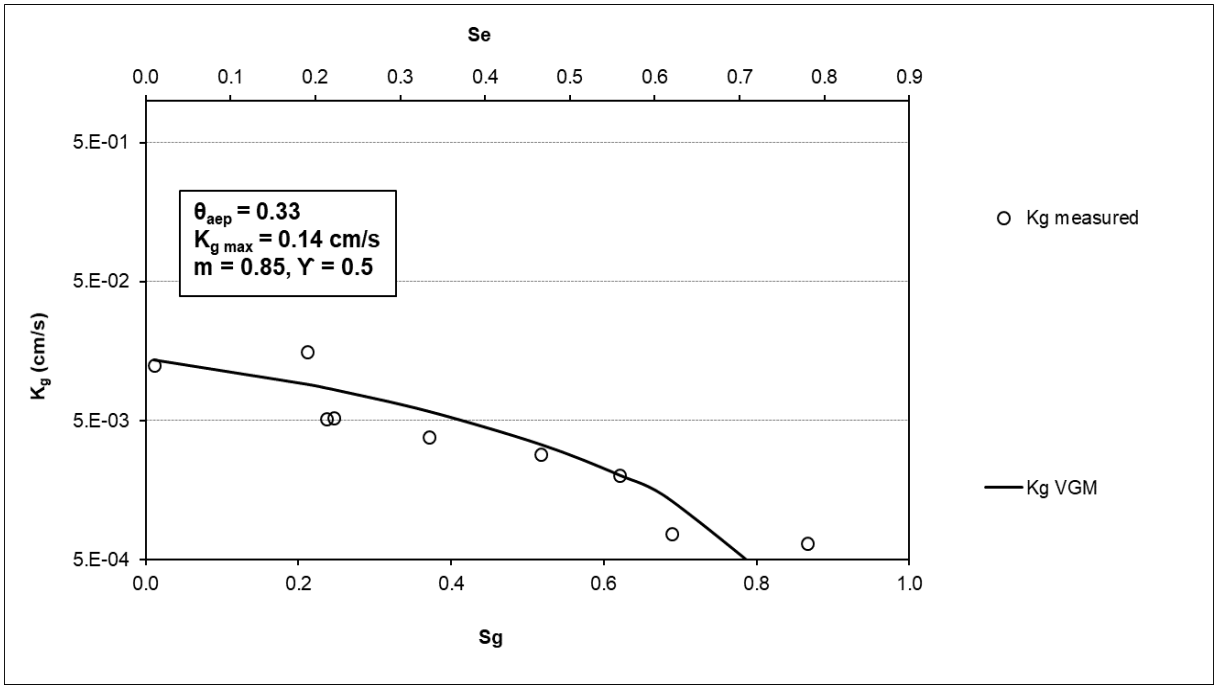

Figure 34. Air conductivity function (EB)

Figures 35, 37 and 38 are plotted in order of increasing fines (-4.75 mm) content over the x-axis. The distribution of volumetric void fractions in the ore bed is plotted on the y-axis in Figure 35. The bed volume is divided into residual moisture (θ_r), the mobile moisture (defined as the increased moisture over and above the residual moisture) during irrigation governed by BC or VGM capillary flow (θ_{max} - θ_r), the volume fraction comprising "dead voids" (θ_s - θ_{max}), and the volume fraction occupied by solids (1 - θ_s).

Also plotted on the y-axis is the air entry point (θ_{aep}) derived from the gas conductivity curves (equation 33). The parity plot between the air entry point (θ_{aep}) and the point of discontinuity (θ_{max}) is presented in Figure 36, with the slope of the best-fit regression line equal to 1.139. Hence θ_{max} is on average slightly larger than θ_{aep}, suggesting the air entry point occurs below the point of discontinuity. This may occur because the air entry closes a little short of maximum saturation as there may still be free surface flow around entrapped air spaces even if there are no longer continuous gas channels. Alternatively, it may be ascribed to uncertainty related to the determination of an exact value of θ_{max} (it is always a result of extrapolation, and one would always expect physical / statistical uncertainty around what essentially constitutes a discontinuity in a highly heterogeneous system).

The close agreement between θ_{aep} and θ_{max} suggests that the air entry point occurs close to the point of discontinuity in the HCF. This may be explained by the fact that no new solution flow channels are expected to form once all the air flow channels are filled up with solution (one would expect air flow channels to be converted into solution flow channels as the moisture content increases).

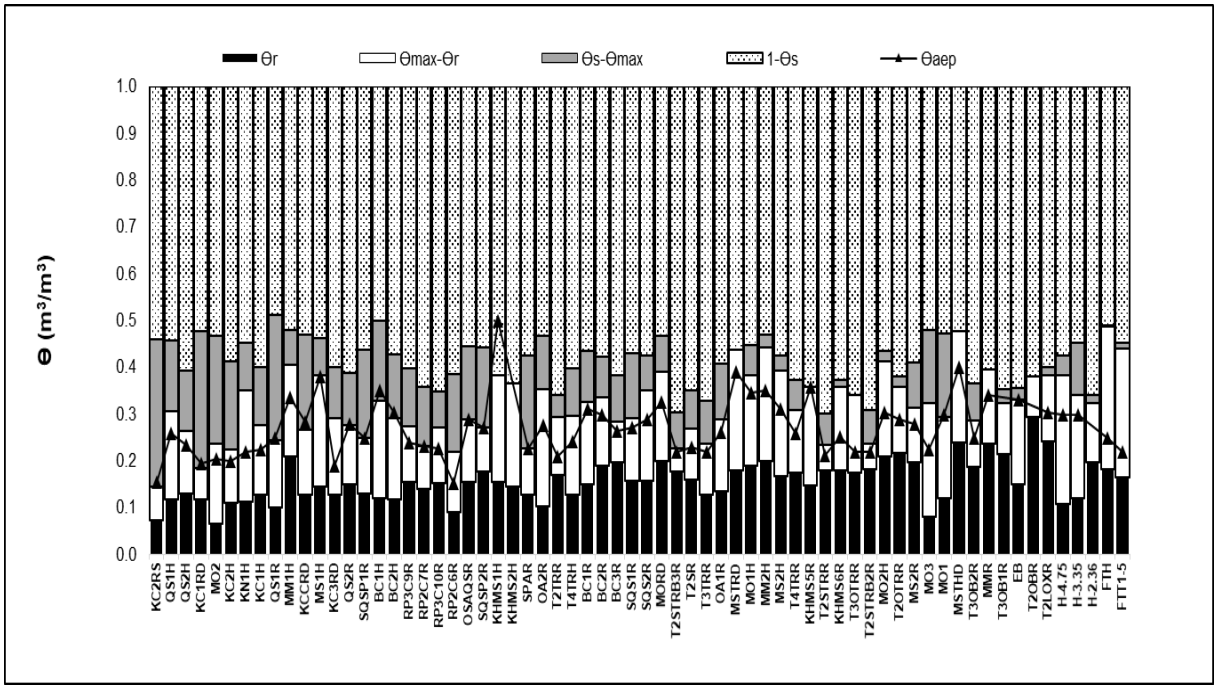

Figure 35. Volumetric void fractions and air entry point versus increasing fines content

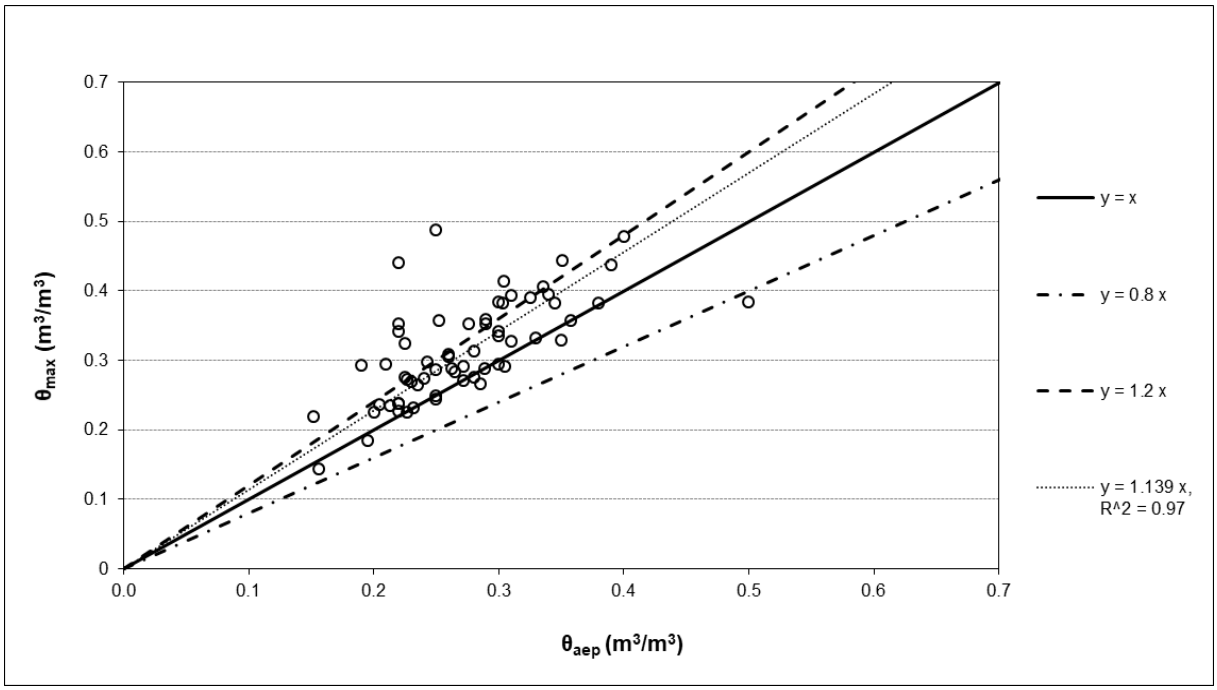

Figure 36. θ_{max} (point of discontinuity) versus θ_{aep} (air entry point)

The normalised void fractions (*i.e.* excluding the volume fraction occupied by solids) are plotted in Figure 37 as this allows visual comparison with some of the design targets used in geomechanical (hydrology and physical) testing, which are also plotted on the same graph. The design targets include the requirement that 65% void saturation ($S \leq 0.65$) should not be exceeded in order to achieve proper aeration, and 85% void saturation ($S \leq 0.85$) should not be exceeded in order to maintain geotechnical stability (Robertson *et al.,* 2013; Milczarek *et al.*, 2012). The 65% saturation rule appears to provide a good design target for heap aeration, as it agrees visually with the air entry point on average. The average air entry point occurs at S = 0.66. In other words, 65% void saturation provides on average a good estimate of the air entry point (θ_{aep}) above which gas does not pass through the bed and above which the heap cannot be aerated.

An air entry point substantially below 65% may be indicative of poor pore interconnectivity, whereas an air entry point above 65% suggests pores with good interconnectivity. It can also be seen from Figure 38 that coarser samples generally have a lower air entry point and that the proportion of "dead voids" (θ_s - θ_{max}) generally decreases as the fines content increases (from left to right over the x-axis). Coarser particles therefore contribute more to the formation of "dead voids", which is counter-intuitive, as one would expect coarser rocks to generate larger macro-voids and hence larger flow channels. However, the formation of larger voids may not necessarily translate into larger flow channels as the pores may not be well connected or may be blocked with finer material such as silt and clay.

The target for geotechnical stability ($S \leq 0.85$) occurs above the air entry point and the point of discontinuity in most cases. Hence the bed will become geotechnically unstable during the filling up of the "dead voids" and starts to break apart since further increase in moisture cannot be directed towards creating new flow channels. High saturation may occur in non-aerated heaps (*e.g.* copper oxides) at very high bulk densities or due to non-homogeneity, or if the bed contains a high silt and clay content which increases the compressibility of the bed. Increased water content can reduce the stability of the rock slope by increasing the unit weight of the soil. The increased water pressure may cause instability if the increased load exceeds the shear strength of the slope. At low moisture contents, for example, the pore pressure is negative (suction), but this is converted into positive pore pressure at higher moisture contents, resulting in increased pressure exerted by the water downwards and sideways in the heap. If the material is dry or non-saturated, an increase in load compresses and compacts the mass and increases shear strength as grains and rock fragments come in closer contact with each other. However, increasing pore pressure with increased moisture content has a buoying effect, reducing the friction and shear strength.

Figure 38 shows the VGM constant, m, plotted on the secondary y-axis, with the volume fractions plotted on the primary y-axis. There is no clear trend for m over the data range, with an average of 0.81 and a standard deviation of 0.25. This is attributed to the fact that S_e was normalised to S_e / $S_{e\ max}$ in equation 42, so that less variability is expected to occur between the various VGM fits. Data in literature typically ranges from m = 0.15 (clay) to m = 0.5 (loam) to m = 0.8 (sand) (Tzimopoulos *et al.*, 1996; van Genuchten, 1980), hence the current data appears to fall within the categories of loam and sand.

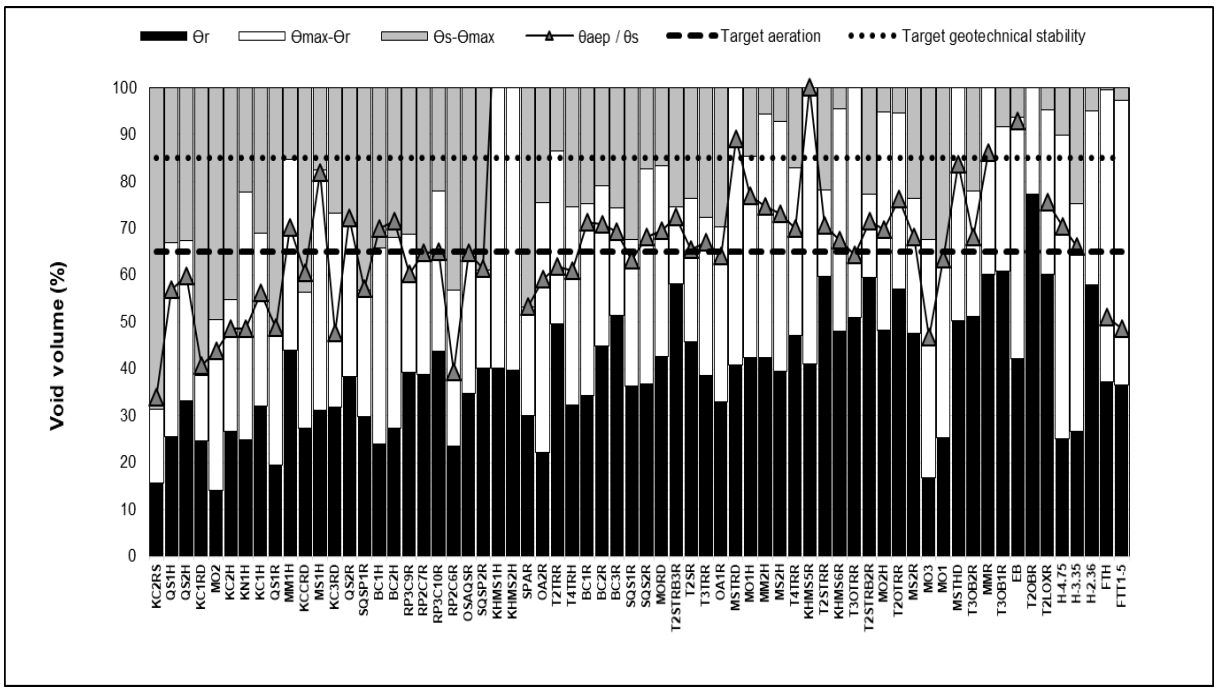

Figure 37. Normalised void fractions and normalised air entry point versus increasing fines content

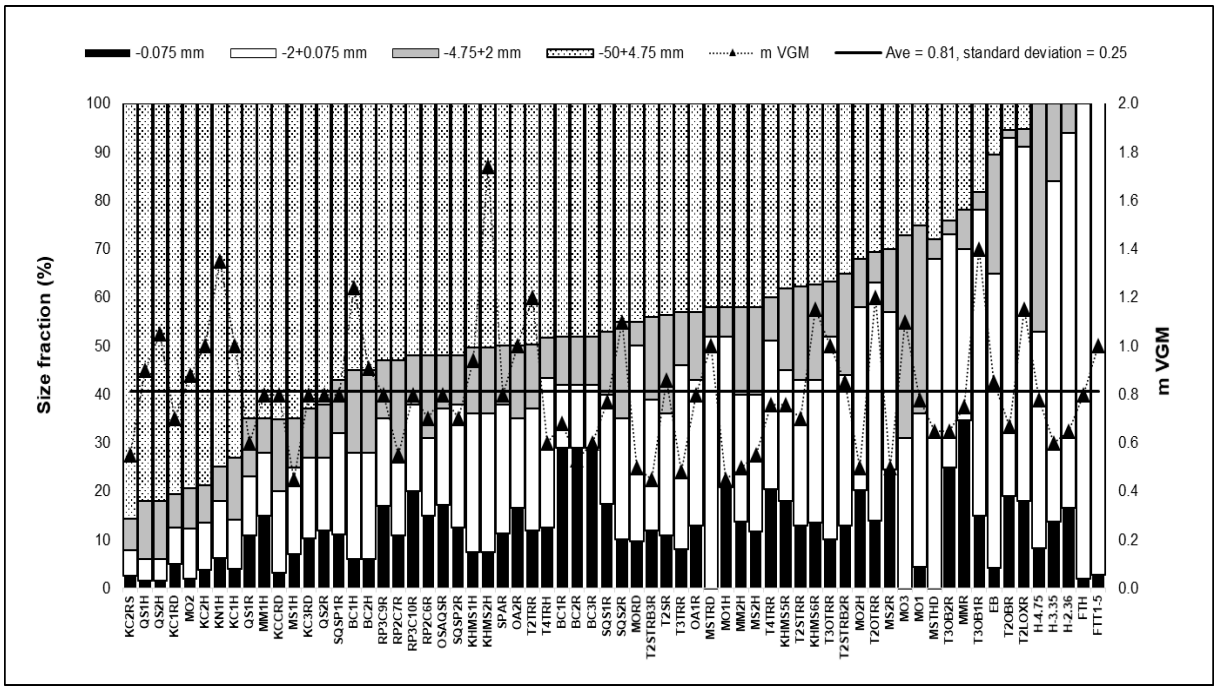

Figure 38. m VGM versus increasing fines content

The benefit of the discontinuous model is that: (1) it provides the first meaningful explanation of the observed discontinuity between the van VGM fit and the saturated flow measurements based in physical reality; (2) it is the first model which can combine both unsaturated data (which clearly fits a capillary model) and actual measured saturated hydraulic conductivities. In fact, most investigators do not even measure the HCF but only measure the WRC and K_s, and then reconstitute the HCF from these two; (3) it provides a meaningful explanation of the air entry point, and why it doesn't occur, for example at 100% saturation. The air entry point corresponds with the inflexion point, which provides strong support for the model; and (4) unlocks further interpretation and explanation of "rules of thumb" which cannot be inferred from earlier models.

5.2.2. Flow of air with residual stagnant solution phase

Using equation 39, together with the value of $K_{g\ max}$ determined from the VGM fit, the hydraulic radius ($r_{H\ gas} / \tau$) was calculated and plotted in Figure 39 on the secondary y-axis. The PSD size fractions are plotted on the primary y-axis, but the graph was inverted to show the relationship between $r_{H\ gas} / \tau$ and the coarser (-50+4.75 mm) size fraction. The porosity used here was $\varepsilon_g = \varepsilon_s - \varepsilon_r$, *i.e*. the void fraction filled with gas when only residual solution moisture is present in the bed (no solution flow). The value of $r_{H\ gas} / \tau$ ranges broadly from 10 µm to 150 µm and shows a general decrease as the coarse (-50+4.75 mm) fraction decreases. In other words, coarser beds create larger hydraulic radii.

For comparison, the values of $r_{H\ solution} / \tau$ were calculated from K_s and equation 9, for saturated solution flow and porosity $\varepsilon = \varepsilon_s$ (*i.e.* when the total bed porosity is occupied by solution). As indicated in Figure 40, $r_{H\ solution} / \tau$ was between 8 µm and 51 µm. This corresponds to an r_H of between 12 µm and 73 µm if one assumes a tortuosity of 1.44 and between 92 µm and 226 µm if one assumes a tortuosity of 4.44. Hydraulic radii for the samples with a topsize of -4.75 mm on the right of Figure 40 were between 15 and 25 µm, if one assumes a tortuosity of 1.44.

Since the ratio r_H / τ is larger for the gaseous flow, it suggests that either the hydraulic radius is larger, or the tortuosity is smaller, or both. This may be a result of the flow channels being partly filled with moisture (θ_r), possibly resulting in lower surface area, with the smaller pores expected to have been filled by solution due to capillary action, leaving behind larger and straighter pores for the air.

Both $r_{H\ gas} / \tau$ and $r_{H\ solution} / \tau$ are plotted against the +4.75 µm fraction in Figure 41, and the regression lines with 95% confidence intervals are plotted in each case. In both cases, there is a lot of variability around the parity line, possibly due to deviations from spherical geometry and variable amounts of silt and clay which may adhere to larger particles or change the pore structure.

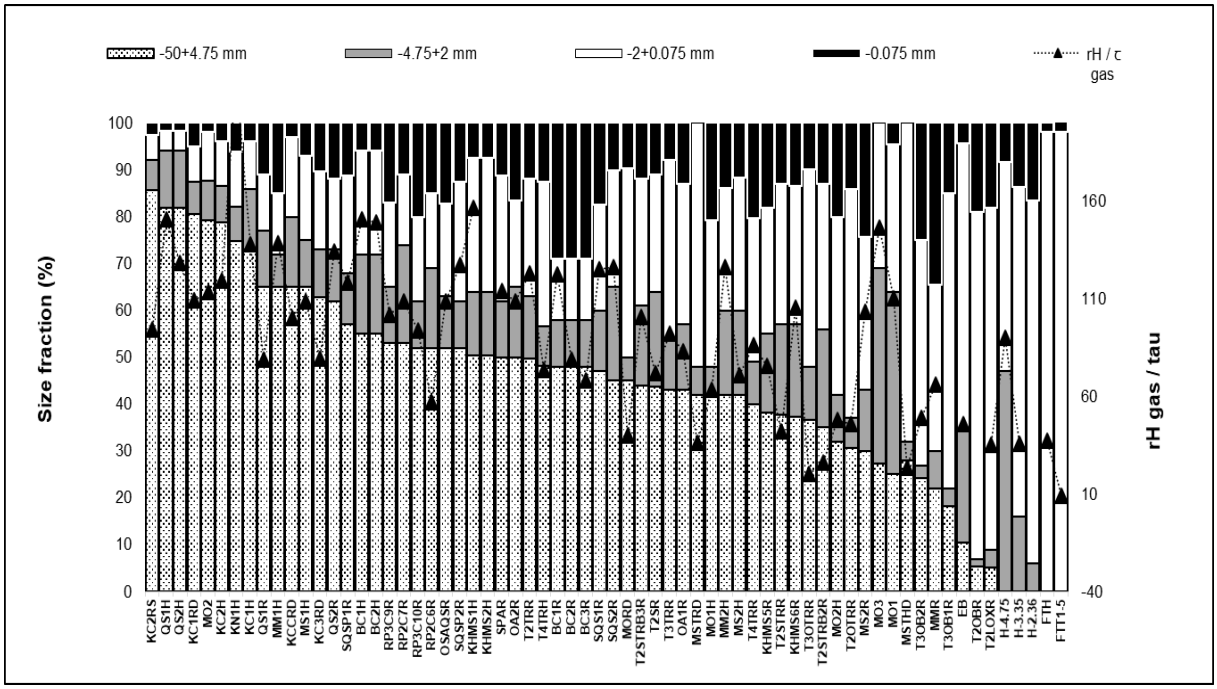

Figure 39. Size distribution and $r_{H\ gas}$ / τ versus increasing fines content

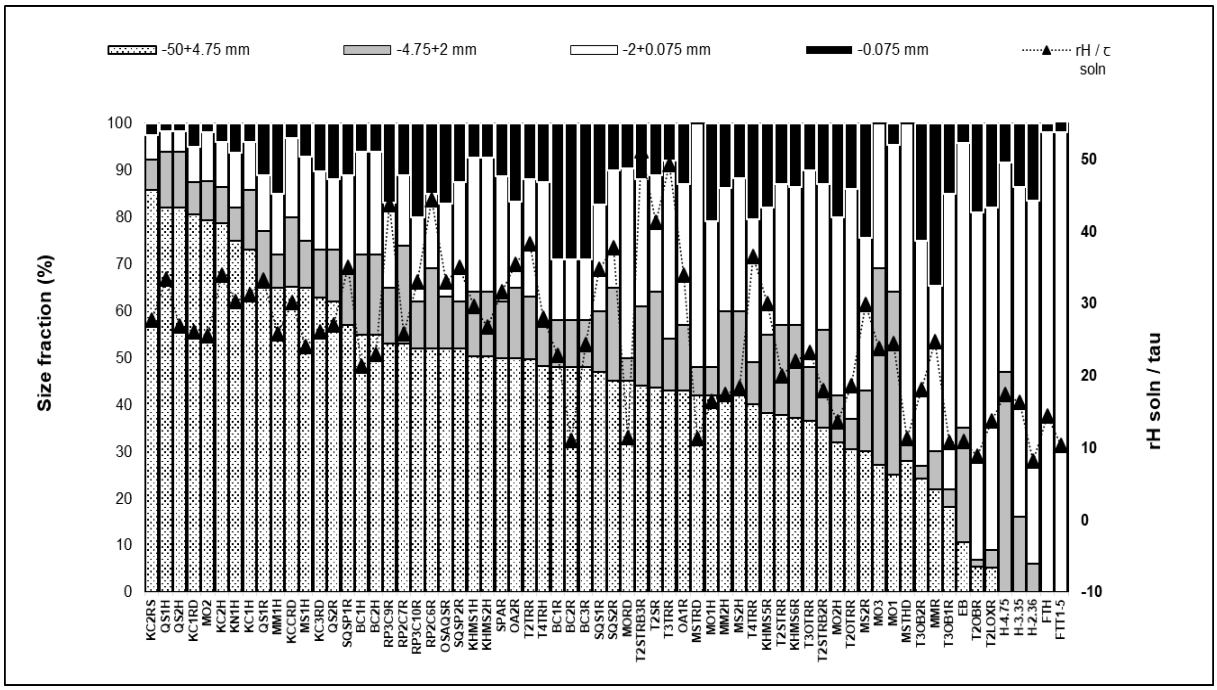

Figure 40. Size distribution and $r_{H\ solution}$ / τ versus increasing fines content

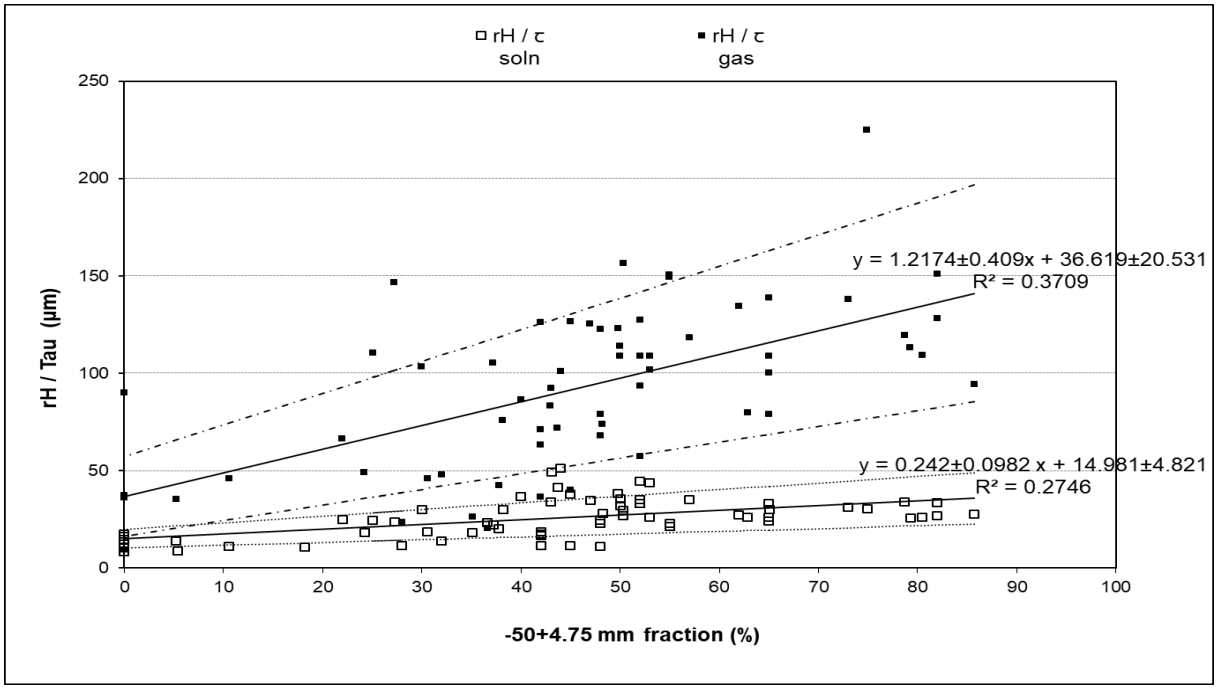

Figure 41. r_H / τ versus % +4.75 mm fraction with 95% confidence intervals (dotted lines)

5.3. Part III – Processing of low permeability ores – desliming and agglomeration with a cementitious binder

The physical and hydrodynamic properties of low-permeability ores are investigated, with particular focus on the micaceous copper stockpile material, in order to identify physical parameters such as high fines content and moisture hold-up which contribute to poor permeability. Two interventions, including desliming and agglomeration with a cementitious binder, and its effect on the hydrodynamics and copper dissolution rates is investigated. The test work progresses sequentially through uni-axial compression tests, hydrodynamic column tests and finally metallurgical column leach tests.

5.3.1. Uni-axial Compression Tests

The compression tests that were conducted in the context of this work are summarised in Table C.1 (Appendix C). Compression test profiles are presented in Figure 42 and 43 for a sub-set of 5 selected samples to display a range of silt plus clay (-75 µm) contents. The 5 samples show an increase in compressibility with increasing silt plus clay (-75 µm) content, as opposed to Milczerak *et al.* (2013) who reported it to be a function of ore grading alone. The targets for both bulk density (<1.89 t/m^3) and corresponding porosity (>0.3 m^3/m^3) are indicated in Figure 42. The absolute bulk density profiles (mass of dry solids per unit volume) and the corresponding porosity profiles (volume of ore bed not occupied by solids) are plotted against stacking height.

By this analysis, the untreated micaceous stockpile material (MSTH) clearly fails the target criteria. Also the sample with 31% -75 µm material (T2XOX) appears to fail the bulk density criterion of <1.89 t/m^3 at a 6 m stacking height, if the data is extrapolated. The sandstone material (T2OBR) appears marginal, whereas the porphyry (POR1) and dolomite (KC2H) samples clearly meet the target criteria at a 6 m stacking height.

Using the definition of the compression index (C_c) (equation 44), where e is the ratio of volume of voids to the volume of solids, and δ is the applied stress (kPa), the compressibility profiles of the same 5 samples are plotted as e versus logδ (Figure 43). The compression index (C_c) is derived from the slope of the linear regression (Terzaghi *et al.*, 1996).

$$C_c = \frac{\Delta e}{\Delta log \delta} \tag{44}$$

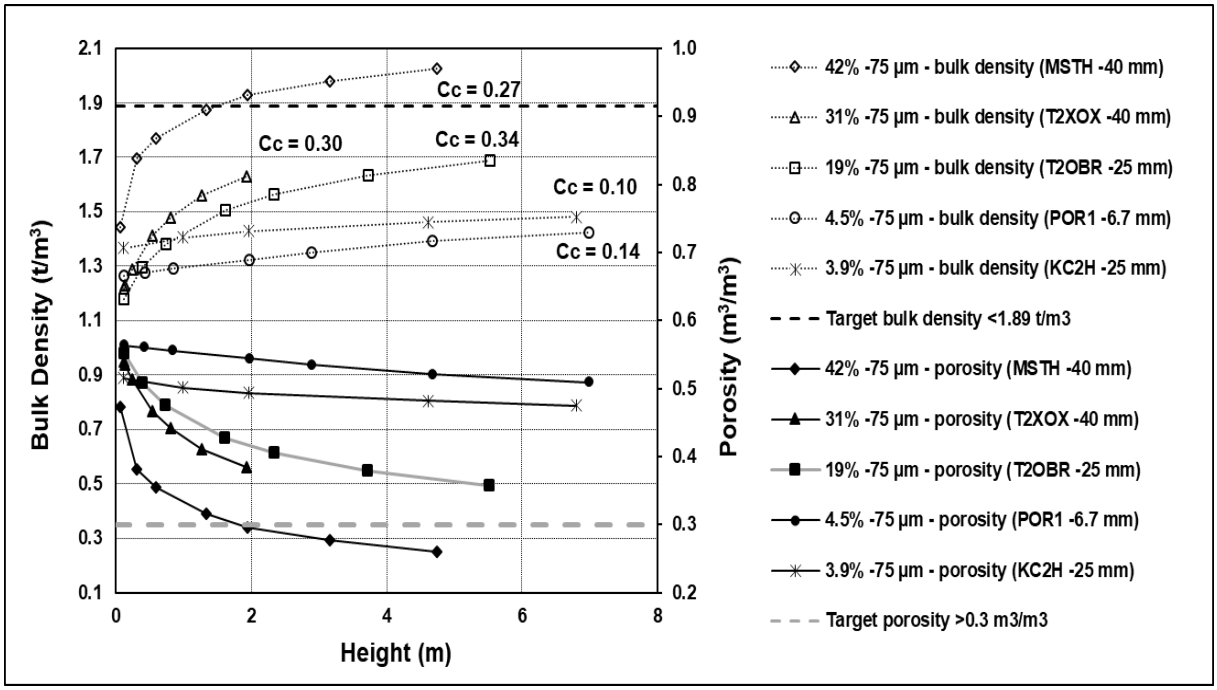

Figure 42. Uni-axial compression profiles (Effect of silt and clay content)

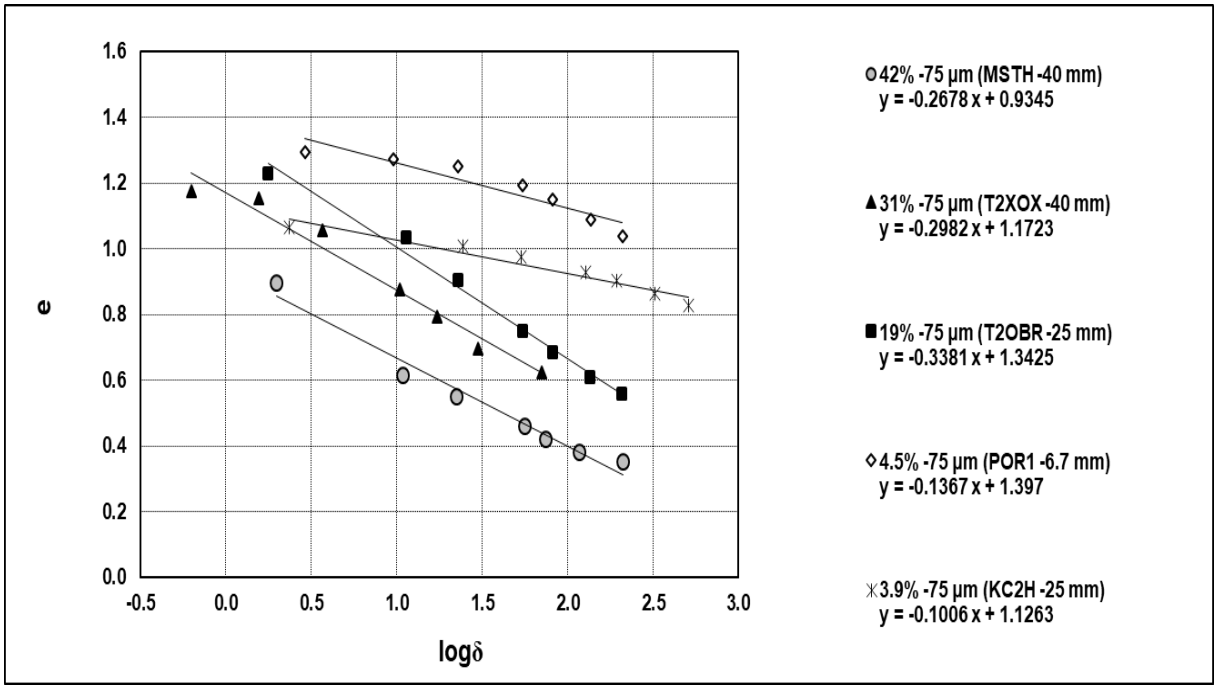

Figure 43. Void ratio versus log of applied stress

The approach used to plot Figure 43 was extended to calculate C_c for the compression profiles of all the samples listed in Table C.1 (Appendix C). These are plotted in Figure 45 (secondary y-axis) against PSD (primary y-axis).

As discussed previously, in this work the particle size distributions are classified as percentage gravel (-50+4.75 mm), coarse sand (-4.75+2 mm), fine sand (-2+0.075 mm) and silt + clay (-0.075 mm). These percentages were plotted as stacked bars on the primary y-axis and have been arranged in order of increasing fines (-2 mm) content on the x-axis (irrespective of ore type) for visual comparison.

Garcia and Jorgensen (1997) recommended that the sample should contain <10% to 15% -75 µm material in order to be suitable for percolation leaching. Most of the samples in Figure 45 meet this criterion, with ZA1R, ZA2R, MMR, T2XOX and MSTH being more notable exceptions. There appears to be a correlation between C_c and the percentage -2 mm material, which suggests the compressibility is related to the presence of fine sand, silt and clay, which may bind together or bind onto coarser rocks during agglomeration.

High compression indices were recorded for the untreated micaceous stockpile material (MSTH, C_c = 0.27), the Namibian sedimentary sandstone oxides (*e.g.* T2OBR, C_c = 0.34; T2LOXR, C_c = 0.35; and T2OBR, C_c = 0.34) and the West African gold ore (BOBO, C_c = 0.32). These samples contain high percentages of -2 mm material and fail the target criterion of Garcia and Jorgensen (1997) of <10% to 15% -75 µm. A high compression index was also measured for the deslimed micaceous stockpile

material (MSTDH1, C_c = 0.23), as it maintained a high percentage of -2 mm material, even though the -75 µm fraction was removed.

Compressibility is expected to be lowest in coarse-grained solids (to the left of Figure 45) where particles are in contact with each other. Compressibility increases as the proportion of small particles increases and it becomes highest in fine-grained soils. Figure 44 shows the linear regression of the graph of C_c versus percentage -2 mm material. The best correlation was obtained between C_c and the -2 mm fraction, whereas linear correlations with -4.75 mm and -0.075 mm material were poorer. Zhao *et al.* (2021) also found the compaction of gravelly soil (-30 mm) to increase with fines (-75 µm) content. At lower fines content (<5%), coarse solids are in direct contact with each other and the fine-grained portion only partially fills the voids. The shear strength of the gravel samples mainly derives from frictional and compression forces between the coarse grains, and compressibility is lowest. As the fines content increases to 10%, the sample has a "densely filled skeleton" structure (Zhao *et al.*, 2021), where fine particles fill the voids between coarser rocks. At high fines content, the fines exceed the amount needed to fill the voids between the coarser rocks and the coarse rocks are interspersed between finer particles. This results in even greater compressibility, as fines are bound onto each other and onto coarser rocks, they experience greater volume change during compression. This explains the sharp increase in C_c to the right of Figure 45 and the small change in C_c to the left of the graph.

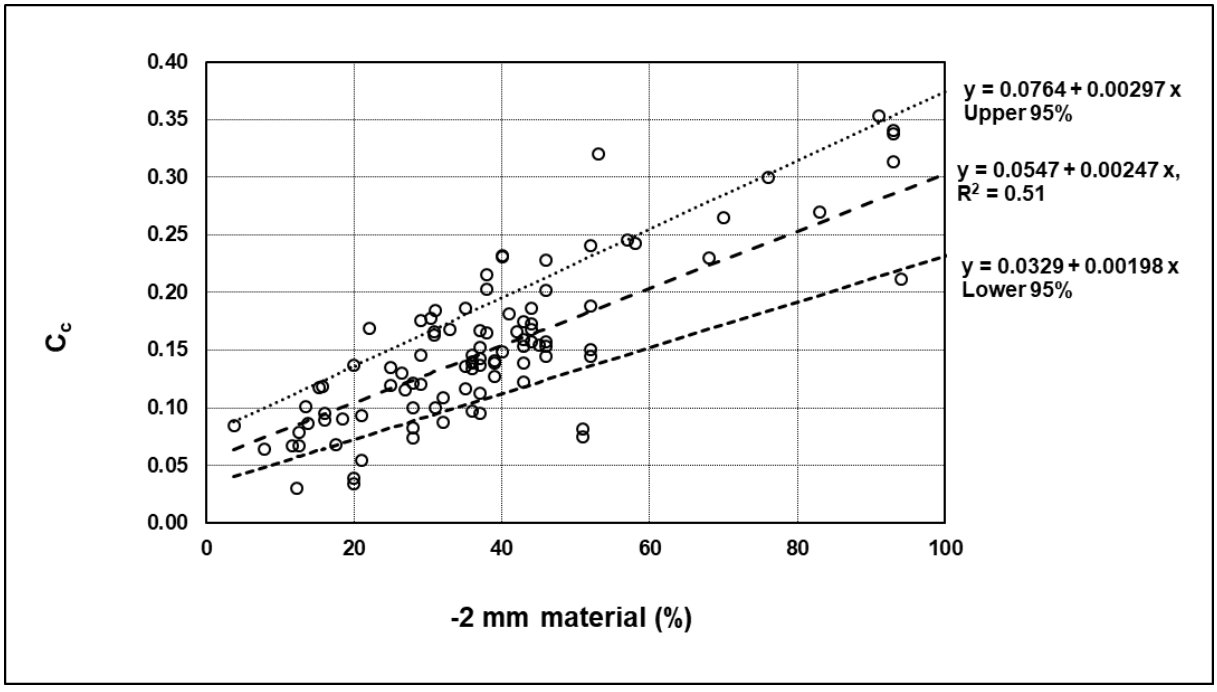

Figure 44. C_c versus percentage -2 mm material

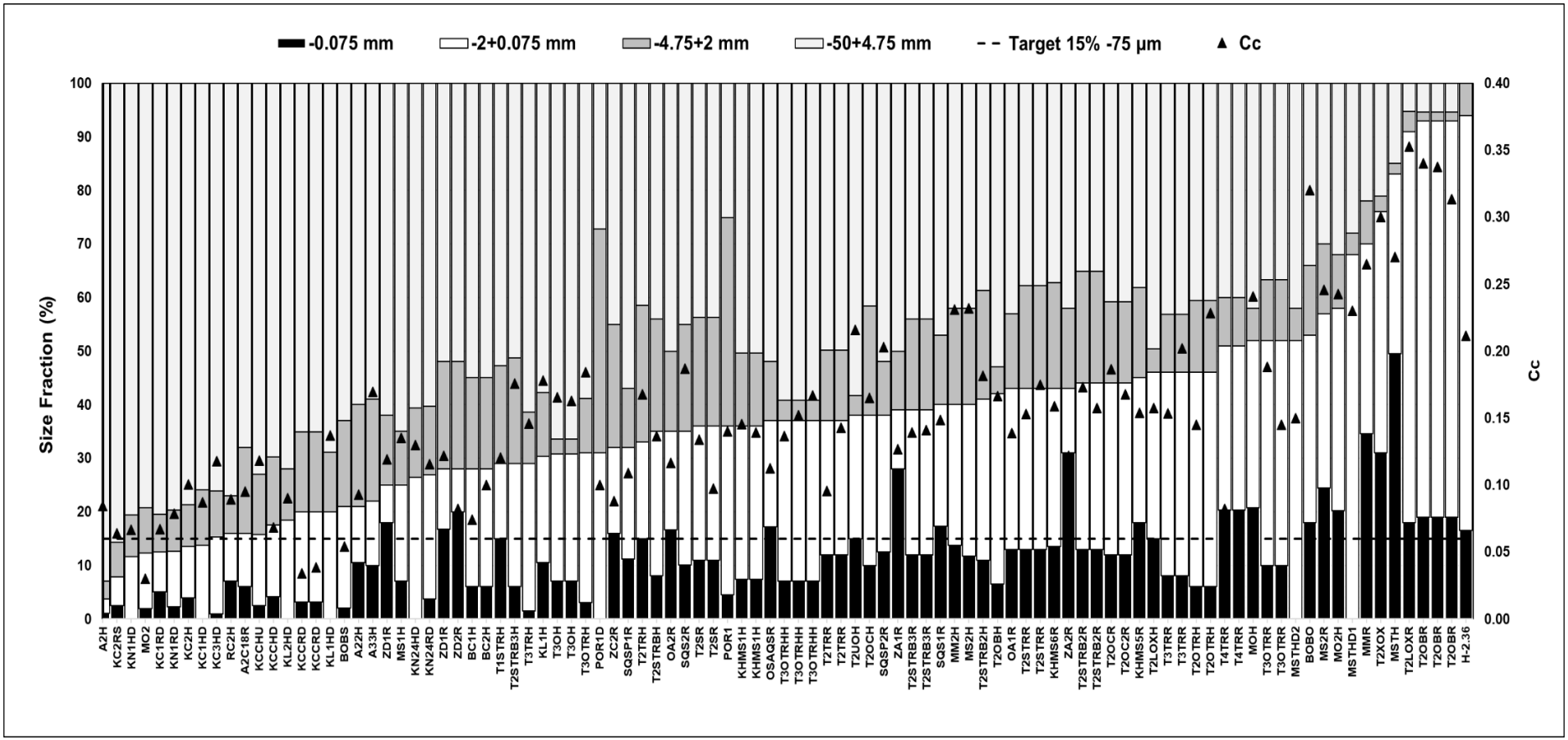

Figure 45. C_c versus particle size distribution

Three of the ore types described in Figures 46 and 47 (micaceous stockpile (MSTH), porphyry (POR1) and dolomite (KC2H)) were subsequently deslimed as part of their respective commercial amenability heap leach test work programmes.

The effect of fines removal is illustrated in Figure 46 for the micaceous stockpile material (MSTH). Desliming of this material by pre-treatment for 10 minutes in a trommel scrubber, followed by wet-screening over a 75 µm or 212 µm screen in a Rhologan shaker, resulted in a substantial improvement in the compressibility and porosity profiles (samples MSTHD1 and MSTHD2). Desliming had little effect on the compression profiles of the porphyry (POR1) and dolomite (KC2H) samples as these had little silt plus clay prior to desliming (Figure 47).

For sample MSTH the porosity after compression in Figure 47 was below 0.3 m^3/m^3, whereas the steady-state moisture hold-up in the hydrodynamic column (Figure 59) was 0.33 m^3/m^3. This suggests that the entire void space will be taken up with solution, and the sample will not be able to conduct air.

The deslimed samples had porosities after compression of 0.39 m^3/m^3 (MSTHD2) and 0.45 m^3/m^3 (MSTHD1) (Figure 46), and steady-state moisture hold-ups of 0.21 m^3/m^3 (MSTHD2) and 0.32 m^3/m^3 (MSTHD1) (Figure 59), respectively. Using these values one can calculate a degree of saturation of 54% (MSTHD2) and 71% (MSTHD1), respectively. This suggests that desliming improves the ability of the sample to conduct air, especially for MSTHD2 (the target for aerated heaps is <65% saturation).

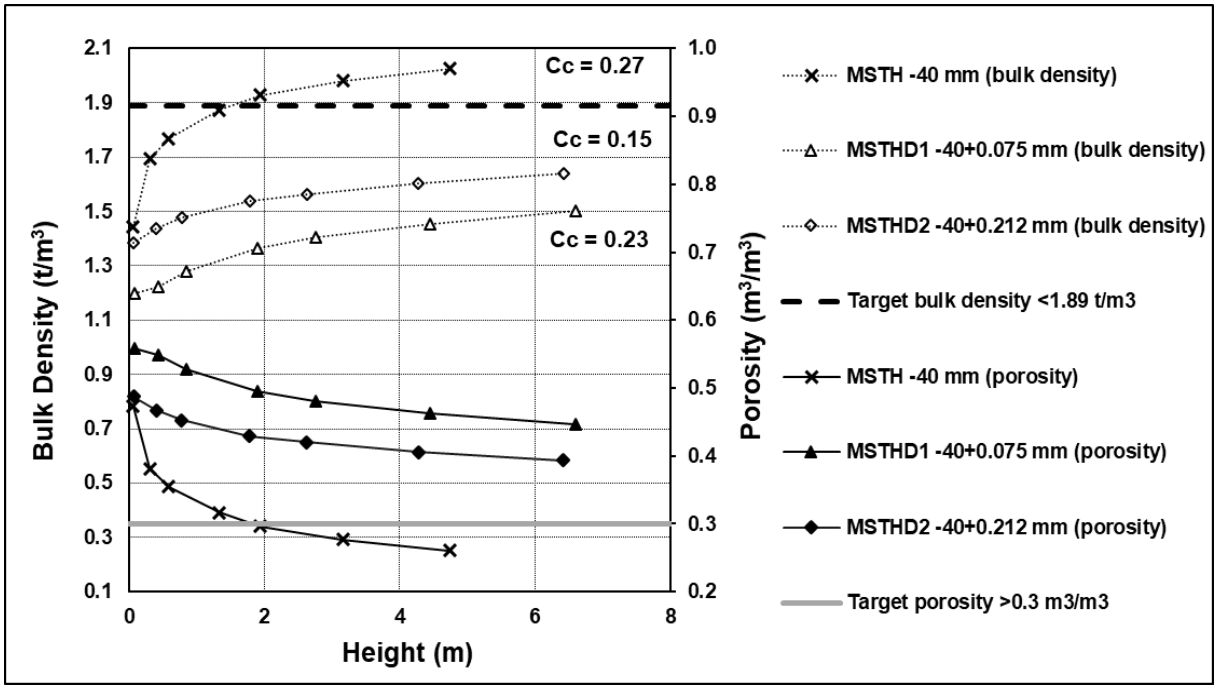

Figure 46. Uni-axial compression profiles (Effect of desliming: micaceous stockpile material)

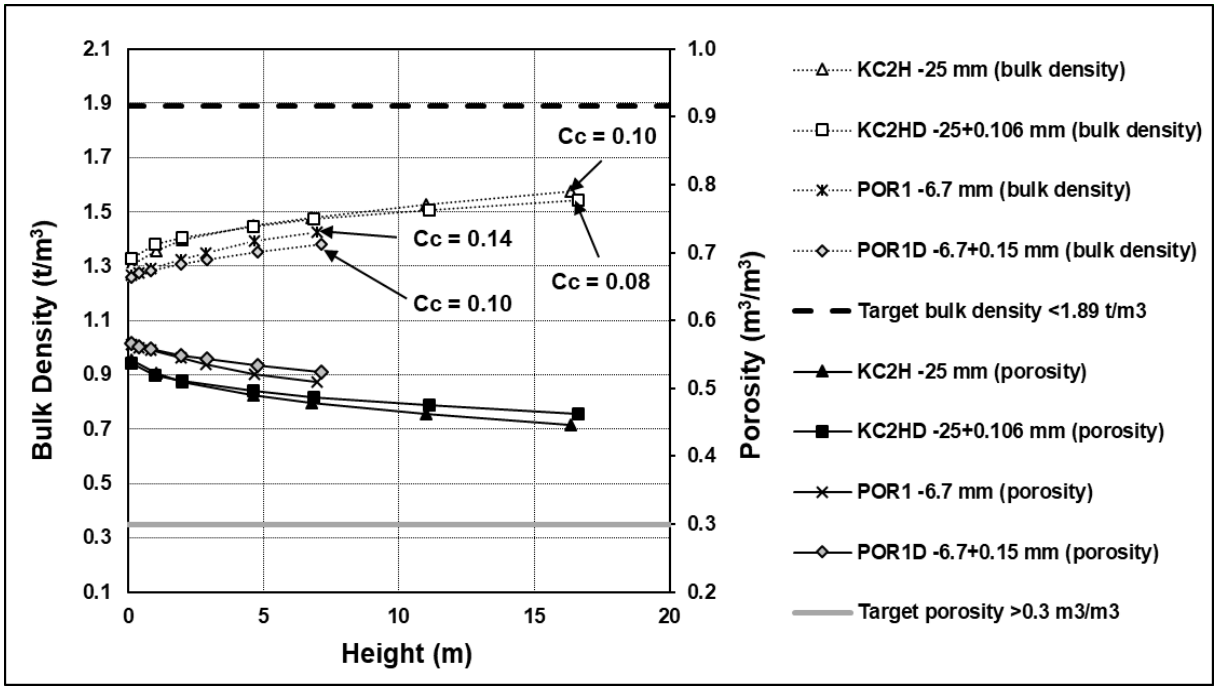

Figure 47. Uni-axial compression profiles (Effect of desliming, dolomite and porphyry)

The effect of agglomeration with binder on the micaceous stockpile sample (MSTH) is illustrated in Figures 48, 49 and 50 for Cements A, B and C.

As expected, the compressibility decreases with increasing cement dosage, with the lower cement additions being close to or failing the target criterion of <1.89 t/m^3 at a 6 m stacking height. The addition of cementitious binder showed a reduction in the value of the compression index C_c for the micaceous stockpile material (Figures 48, 49 and 50) and also for the West African gold ore (BOBO) (Figure 51).

Although the 10 kg/t Cement C addition to the micaceous stockpile sample showed less of a reduction in C_c relative to the 1 kg/t and 3 kg/t additions in Figures 49 and 50, the 10 kg/t samples experienced less slumping after initial pre-wetting. All the micaceous samples were loaded at an initial “as-placed” bulk density of approximately 1.3 t/m^3 and irrigated with 5 g/L H_2SO_4 for 24 hours prior to compression. The 10 kg/t sample did not slump after pre-wetting, compared with the other samples, resulting in a lower final compressed bulk density. Moreover, only the sample agglomerated with 10 kg/t cement was able to conduct solution during the saturated hydraulic conductivity (K_s) measurement. Hence the micaceous stockpile material is deemed suitable for percolation leaching at a cement addition of 10 kg/t.

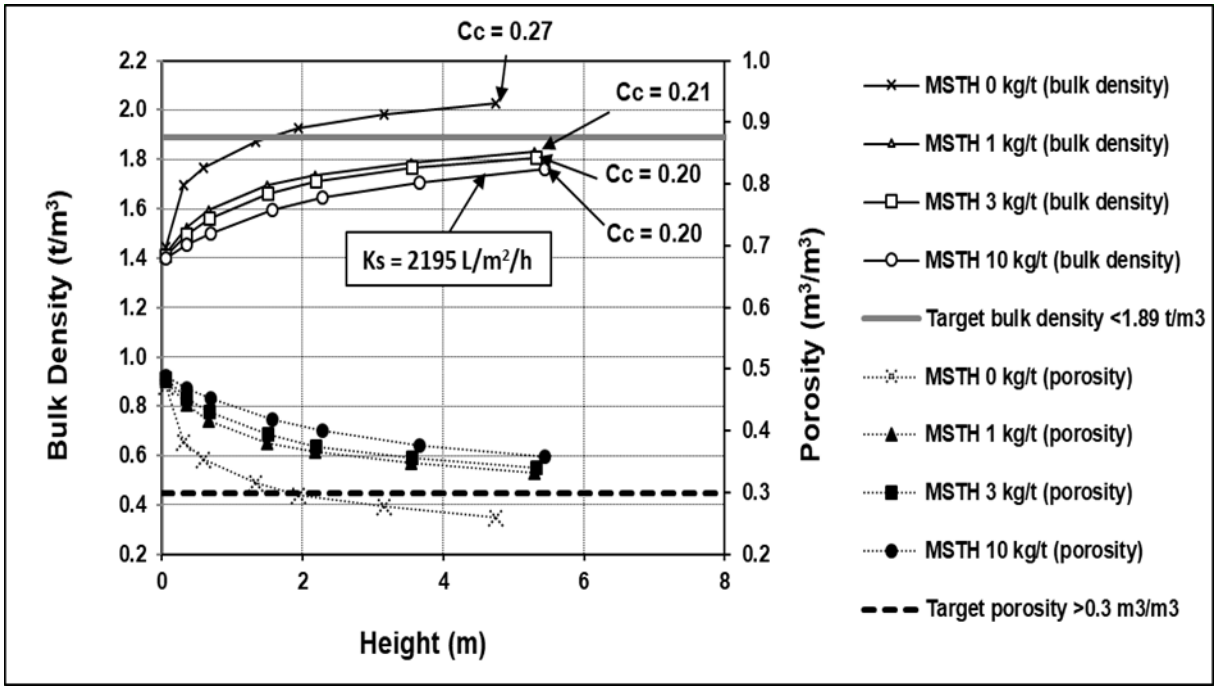

Figure 48. Uni-axial compression profiles (micaceous stockpile, Cement A)

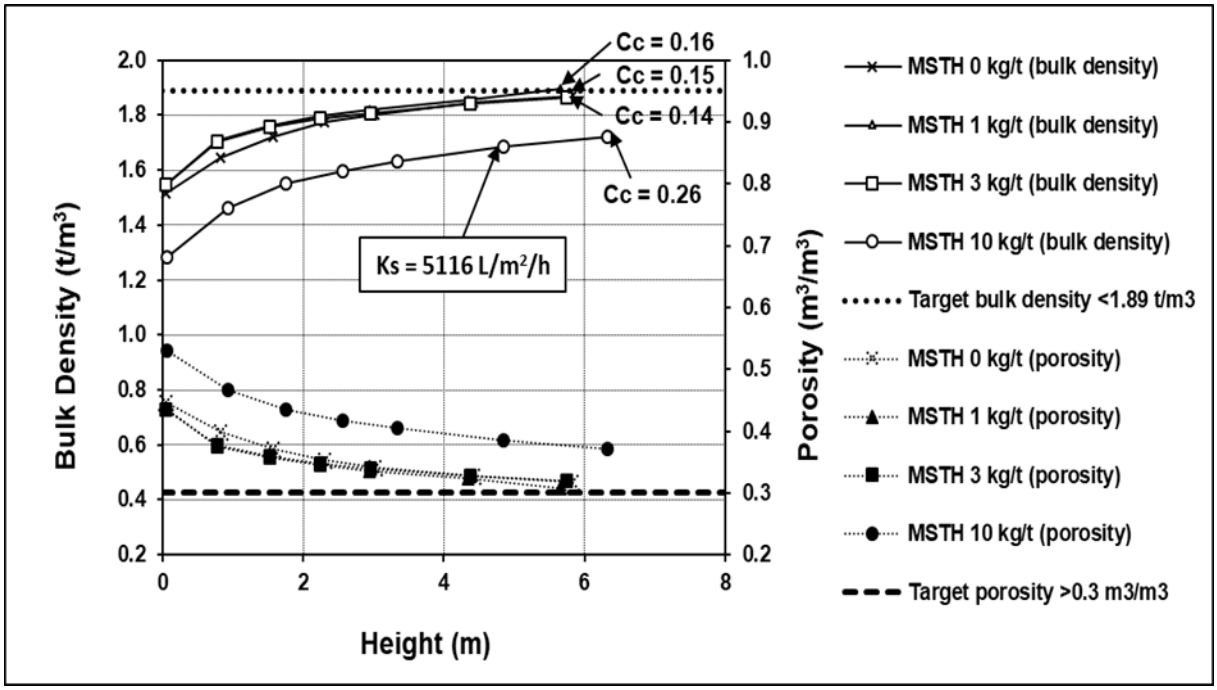

Figure 49. Uni-axial compression profiles (micaceous stockpile, Cement B)

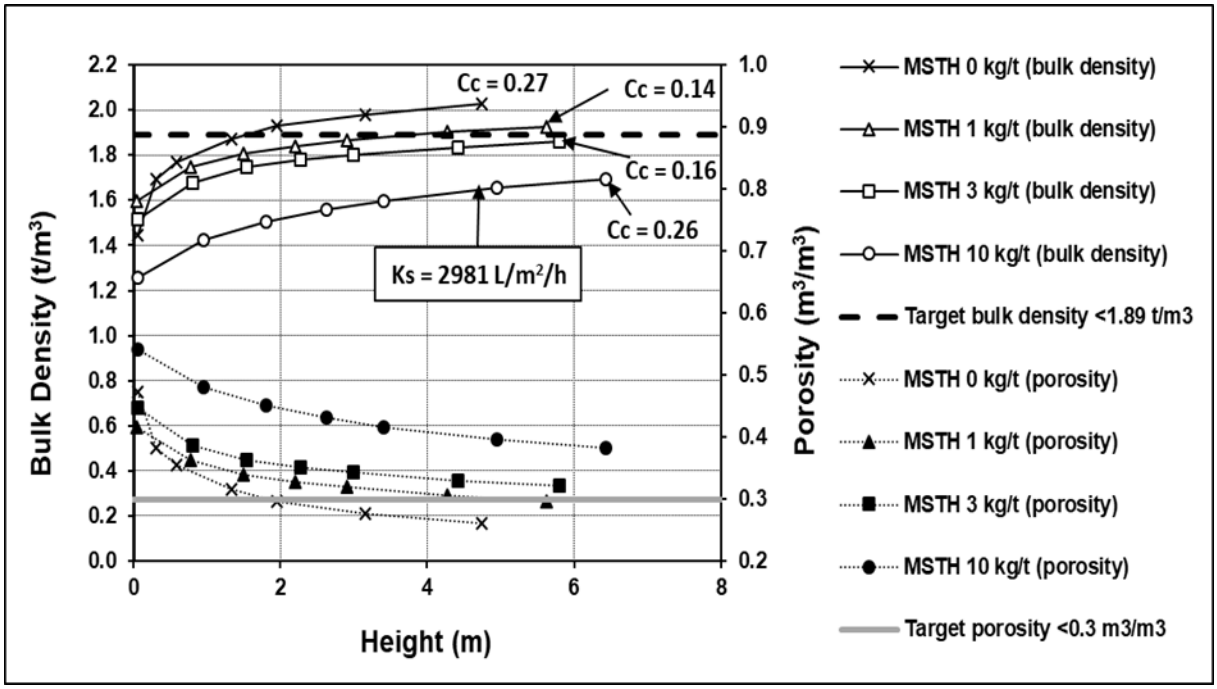

Figure 50. Uni-axial compression profiles (Effect of binder: micaceous stockpile + Cement C)

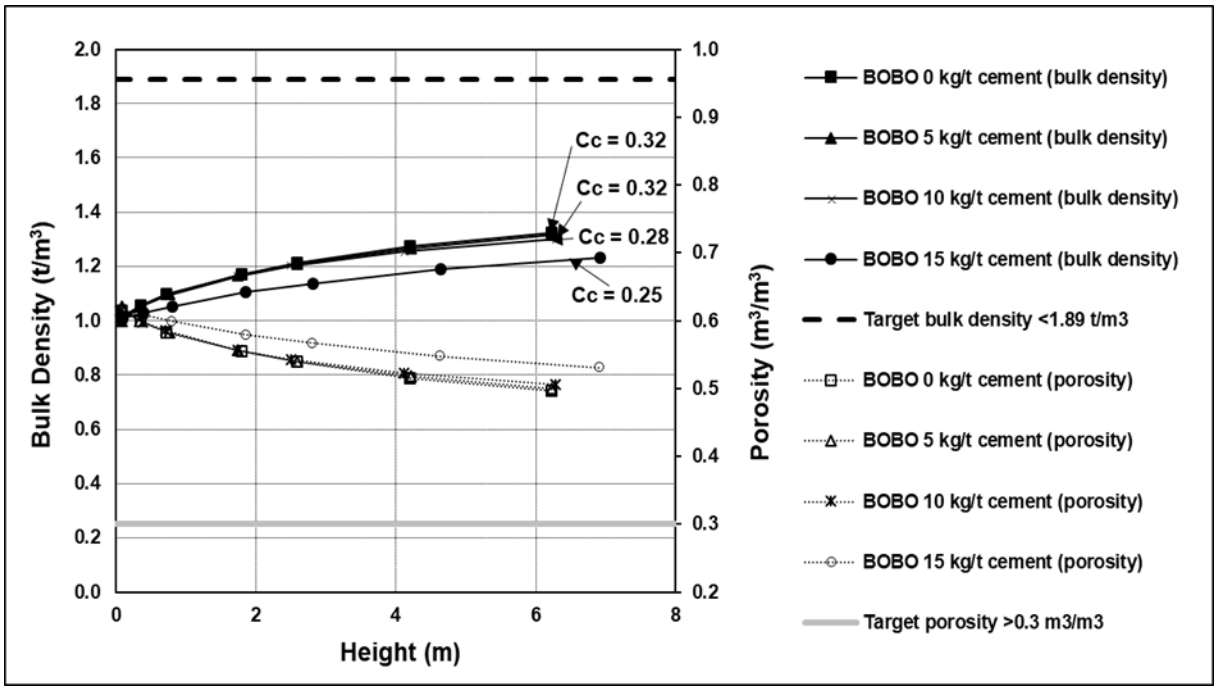

Figure 51. Uni-axial compression profiles (West African gold ore, OPC)

5.3.2. Hydrodynamic column tests

Hydrodynamic column test results are summarised in Table 10 below for the micaceous (MSTH), dolomite (KC2H) and porphyry ores (POR2), where desliming was performed as part of the heap leach amenability test work programme. Initial loaded bulk densities (dry basis) were between 1.43 t/m^3 and 1.71 t/m^3, which corresponded with bed porosities of between 0.35 m^3/m^3 and 0.48 m^3/m^3. The micaceous ore generally displayed higher residual moisture content (10.6% to 17.2%) on account of the higher fines content, compared with 3.7% to 6.7% for the coarser ore types (porphyry and dolomite). The porphyry and dolomitic ores also measured higher saturated hydraulic conductivities (2427 L/m^2/h to 8745 L/m^2/h) compared with the micaceous ore type (99 L/m^2/h to 1700 L/m^2/h).

Table 1010 also shows the ratio between drained and residual moisture after the column has been fully saturated and drained. The micaceous sample typically has a low ratio of drained to residual moisture on account of the higher fines content, whereas the other samples have ratios of close to 50 : 50. The porphyry deslimed at 0.425 mm has a very high ratio of drained to residual moisture (81 : 19) as it has the lowest fines content. The high ratio for the +0.425 mm porphyry sample (POR2D2) suggests that this sample may in fact have *too little* fines, which may impact lateral distribution in the bed if dripper spacing is far apart.

Figure 52 shows the hydraulic conductivity (K_w) versus degree of saturation (S) profiles for the micaceous stockpile material. As the sample is deslimed at coarser screen sizes, the curve shifts to the left, indicating more favourable operation at lower saturation. The values of the saturated hydraulic conductivity (K_s) were 1700 L/m^2/h and 996 L/m^2/h, respectively, for the two deslimed micaceous samples (MSTHD1 and MSTHD2). The unscreened micaceous sample without binder (MSTH) operated close to saturation and measured a much lower K_s of 99 L/m^2/h. The addition of binder shifted the curve to the left and increased the saturated hydraulic conductivity to 165 L/m^2/h.

Table 10. Summary of hydrodynamic column results

Code	Description	Column ID	Crush Size	Binder Cement C	Bulk Density	Porosity	K_s	Residual Moisture	Drained : Residual Moisture	$S_{e\ max}$	m	θ_{aep}	$K_{g\ max}$
		(mm)	(mm)	(kg/t)	(t/m^3)	(m^3/m^3)	($L/m^2/h$)	(%)	(m/m)	(m^3/m^3)		(m^3/m^3)	(cm/s)
MSTH	Micaceous	200	-40	-	1.62	0.41	99	16.4	22 : 78	1.0	0.60	0.41	0.14
MSTH	Micaceous	200	-40	10	1.60	0.42	165	17.2	17 : 83	1.0	0.65	0.42	0.28
MSTHD1	Micaceous	200	-40+0.075	-	1.50	0.48	1700	15.6	30 : 70	1.0	0.65	0.48	0.003
MSTHD2	Micaceous	200	-40+0.212	-	1.62	0.44	996	10.6	48 : 52	1.0	1.0	0.41	0.011
KC2H	Dolomite	200	-25	-	1.55	0.41	8735	4.6	37 : 63	0.38	1.0	0.20	0.14
KC2HD	Dolomite	200	-25+0.106	-	1.43	0.46	5000	3.7	47 : 53	0.19	0.55	0.16	0.11
POR2	Porphyry	160	-6.7	-	1.78	0.35	2427	6.7	45 : 55	0.78	0.65	0.25	0.08
POR2D1	Porphyry	160	-6.7+0.106	-	1.71	0.38	3100	5.7	53 : 47	0.72	0.55	0.32	0.04
POR2D2	Porphyry	160	-6.7+0.425	-	1.65	0.43	3799	4.7	81 : 19	0.60	0.61	0.28	0.15

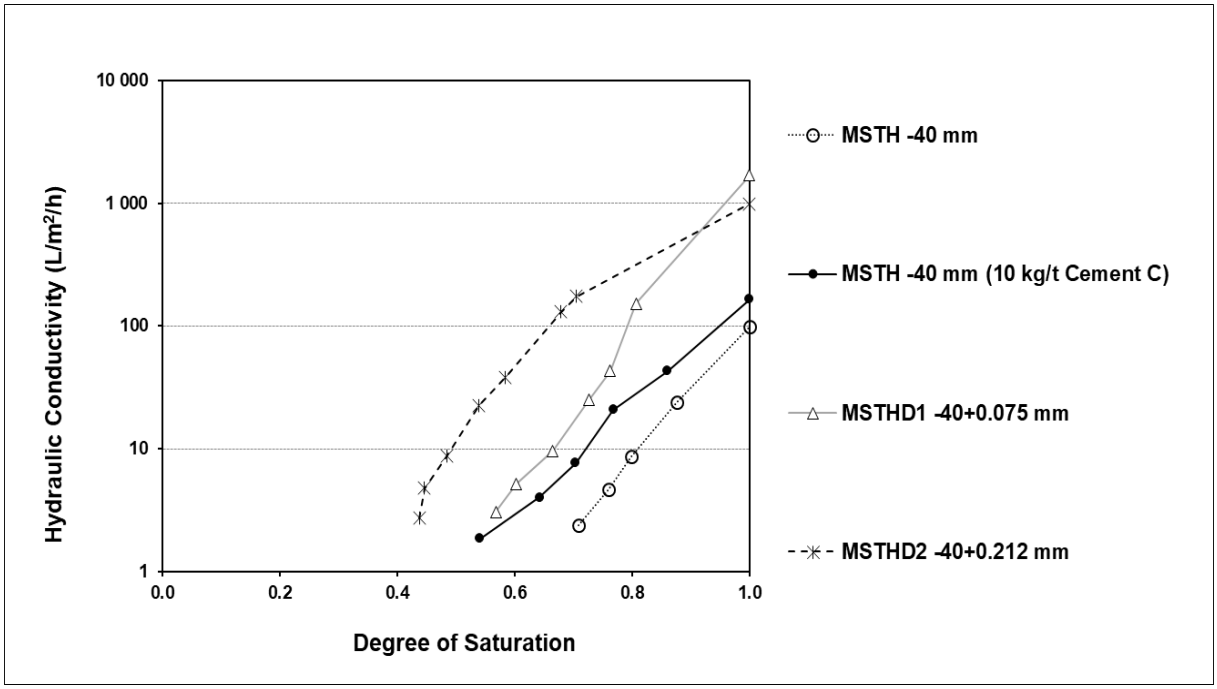

Figure 52. Hydraulic conductivity profiles (micaceous stockpile material

It was previously shown (Section 5.2.1.) that the hydraulic conductivity functions (HCFs) can be modelled with a modified version of the van Genuchten Mualem (VGM) equation (42). This approach was used to fit the data of the experiments summarized in in Table 10. The fitted HCF curves are indicated in Figures 53 to 55 below, showing the effect of binder and desliming on the hydrodynamic properties.

Figure 53 shows the HCFs of the micaceous samples (MSTH, MSTHD1 and MSTHD2). The relative degree of saturation shifts to the left as the cut size increases from 75 µm to 212 µm. A similar result is shown in Figure 54, where the HCF of the -6.7 mm porphyry (POR2) is compared with the -6.7+0.106 mm (POR2D1) and -6.7+0.425 mm (POR2D2) deslimed samples. K_s increases from 2427 L/m^2/h (POR2) to 3799 L/m^2/h (POR2D2), and the sample operates further away from saturation at higher cut size. The HCFs of the dolomite whole ore (KC2H) and deslimed dolomite (KC2D) are shown in Figure 55. Both samples measured a high K_s, but desliming shifted the HCF to the left, indicating lower saturation. The VGM fits of the HCFs of the micaceous stockpile materials do not display a point of discontinuity, as these sample mostly consisted of clay, silt and sand with little gravel. In these cases, the air entry point corresponds with the point of 100% saturation. The samples with a larger percentage gravel (dolomite and porphyry) displayed points of discontinuity in the VGM fits. It was mentioned in the previous section that the point of discontinuity shifts to the left as the PSD becomes coarser.

As mentioned in Section 5.2.1., equation (33), a modified version of the VGM function, can be used to fit the air conductivity profiles. Air permeability curves showing the effect of binder and desliming are

presented in Figures 56 to 58. The air entry point was found to correspond closely with the point of discontinuity determined independently from the HCF curves, as discussed in Section 5.2.1.

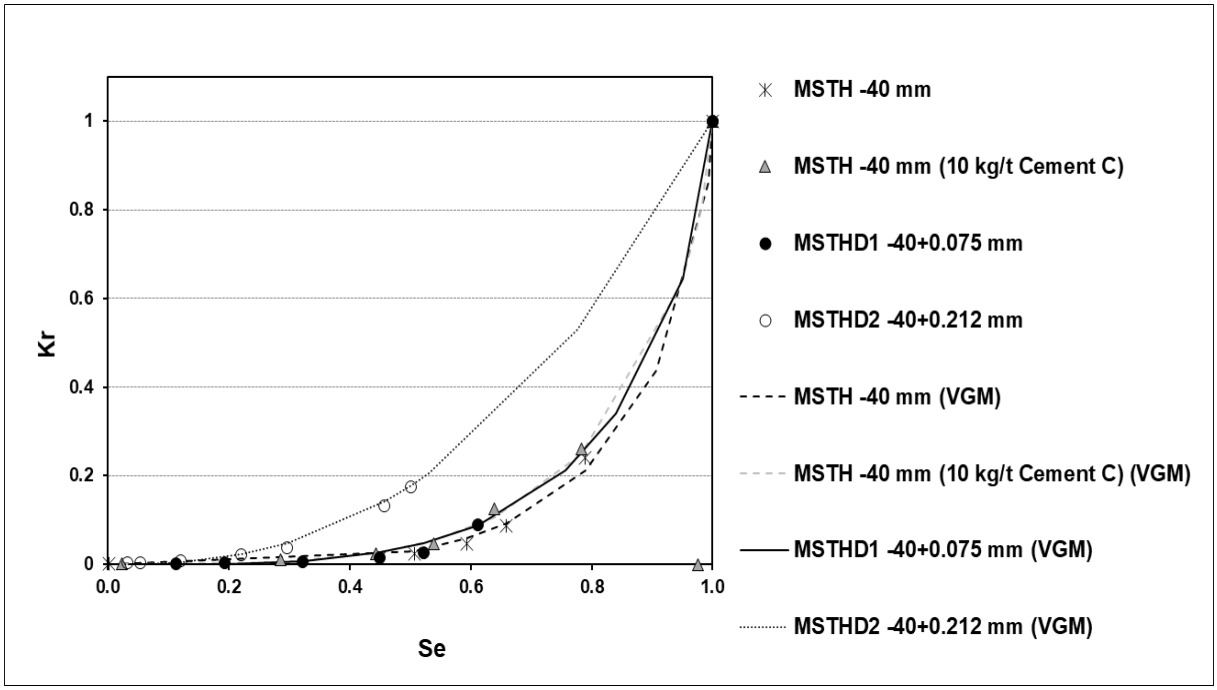

Figure 53. Relative hydraulic conductivity profiles (micaceous stockpile material)

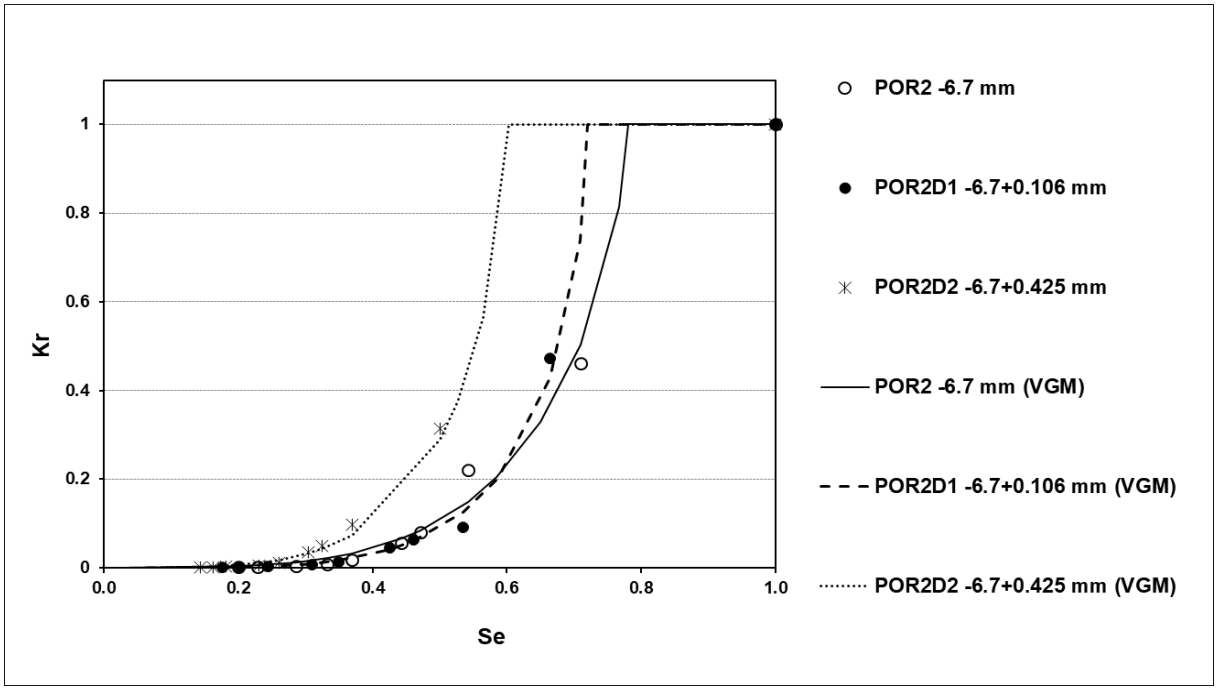

Figure 54. Relative hydraulic conductitivy profiles (porphyry)

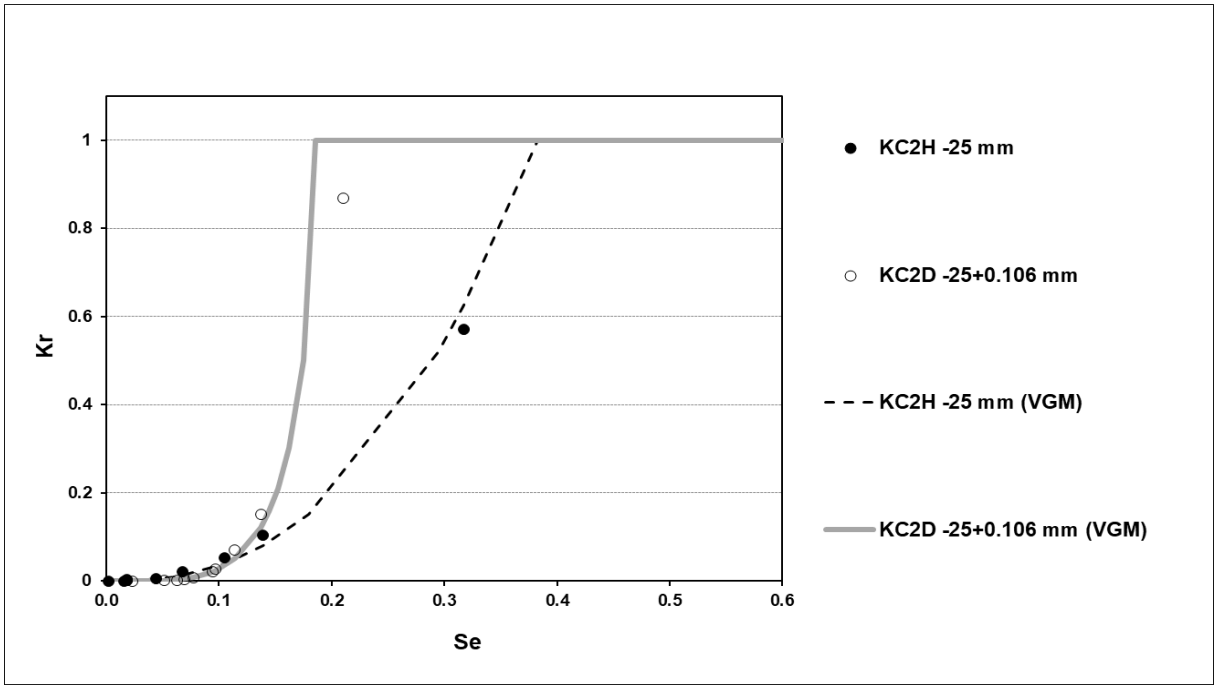

Figure 55. Relative hydraulic conductivity profiles (dolomite)

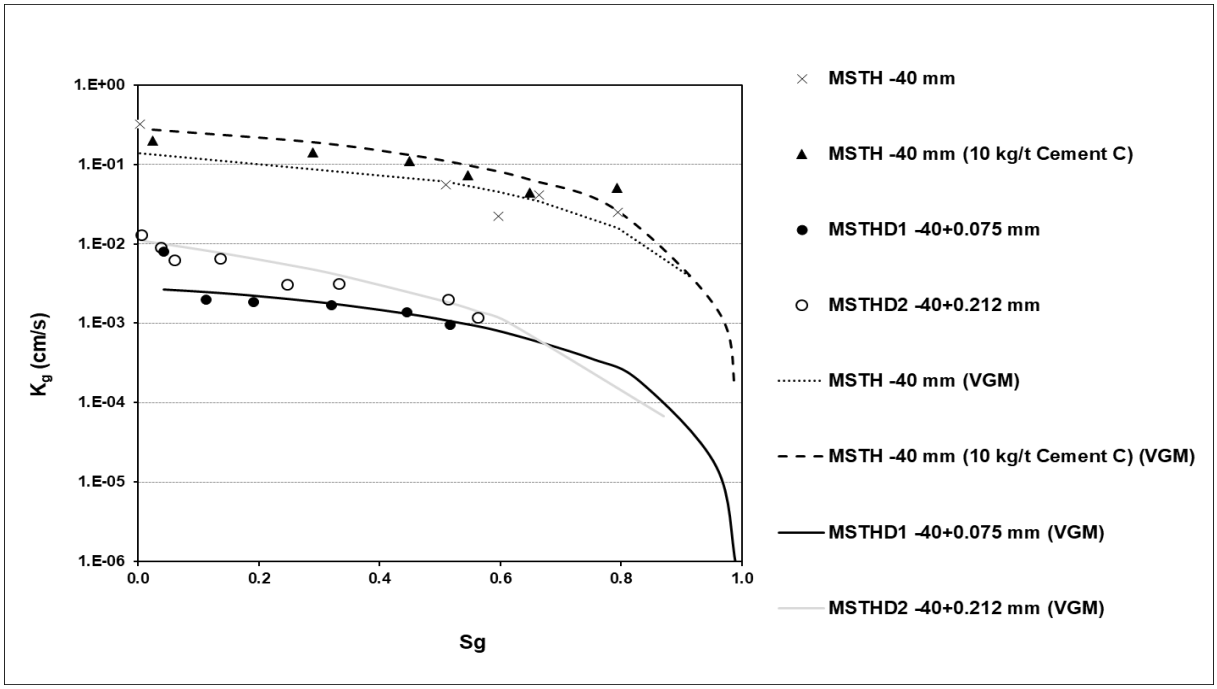

Figure 56. Air conductivity profiles (micaceous stockpile material)

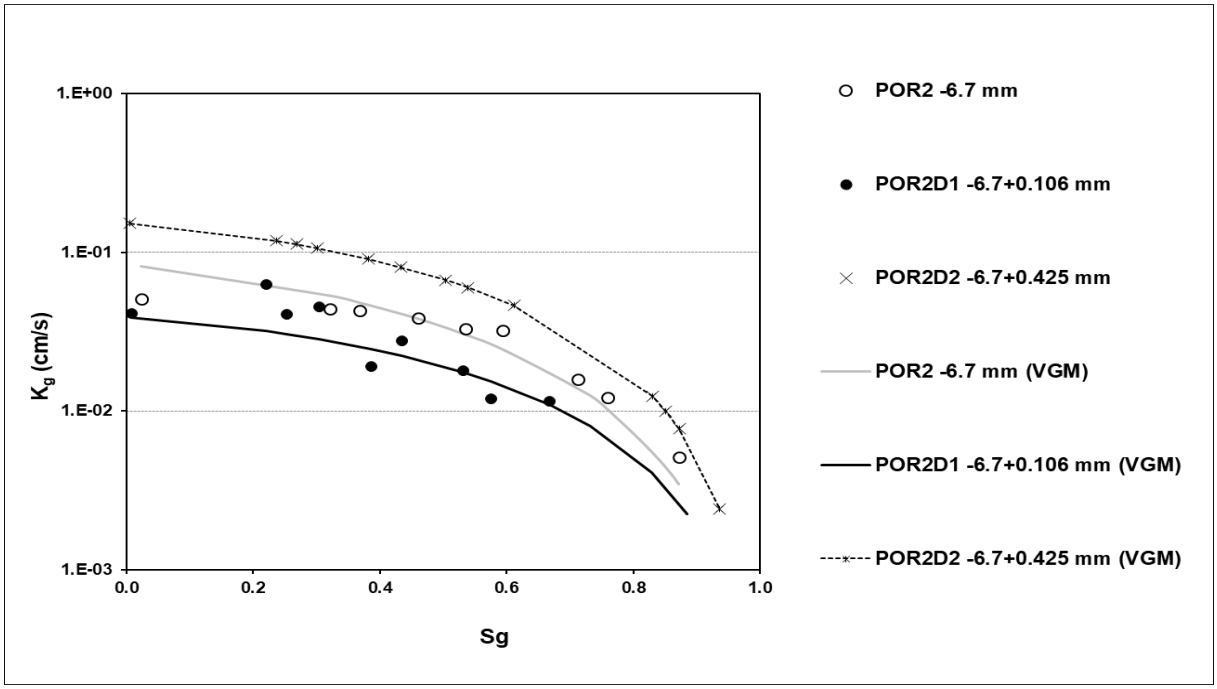

Figure 57. Air conductivity profiles (porphyry)

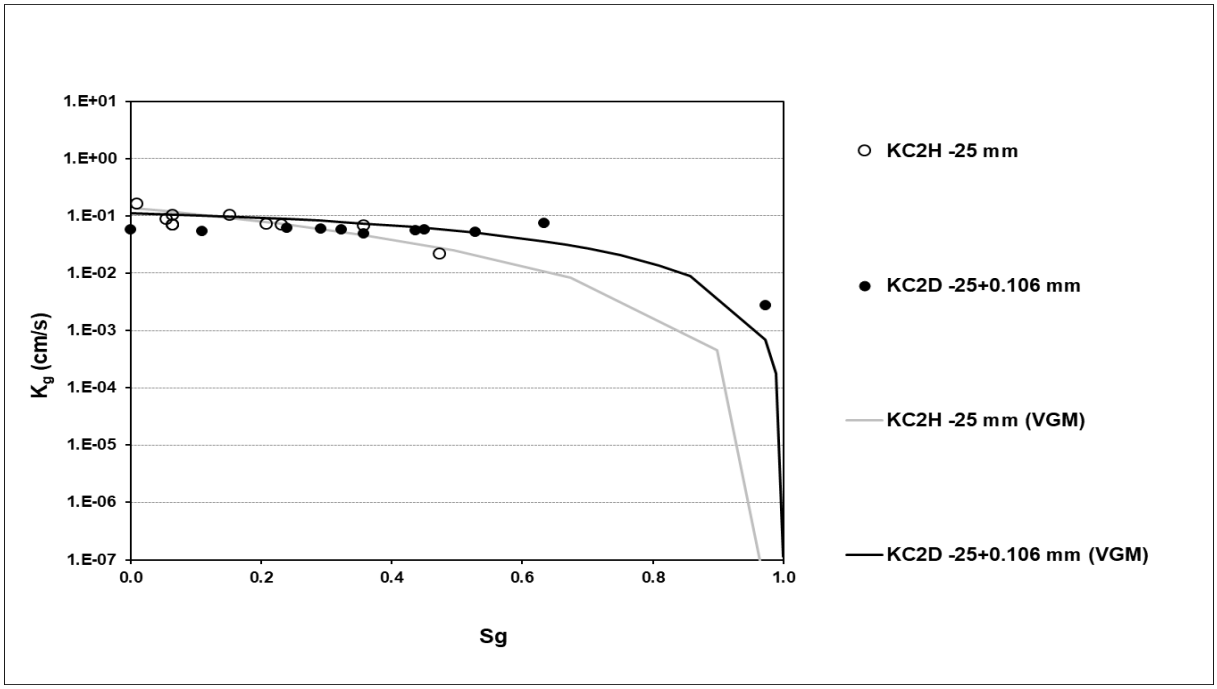

Figure 58. Air conductivity profiles (dolomite)

As discussed in Section 5.2.1., the distribution of the void fractions in the bed can be broken down into the volume of solids (1 - θ_s), the volume of residual moisture after drain-down (θ_r), the volume of mobile moisture ($\theta_{max} - \theta_r$) and "dead voids" ($\theta_s - \theta_{max}$). This representation was again used in Figure 59 to represent the various hydrodynamic column tests of Table 10. Also plotted in Figure 59 is the steady-state moisture hold-up at a typical target irrigation rate of 10 L/m^2/h. The reason for the poor permeability in the micaeous stockpile sample (MSTH) can be seen to be a result of the high steady-state moisture hold-up (0.30 m^3/m^3), which is close to the maximum porosity (θ_s). Deslimed mica columns (MSTHD1 and MSTHD2), porphyry columns (PO2, PO2D1 and PO2D2) and dolomite columns (KC2H and KC2D) operated further away from saturation, as these had lower steady state hold-up moistures resulting from lower fines contents. Poor permeability can therefore be attributed to a high steady-state moisture hold-up resulting from a high fines content, which results in the column operating close to saturation. The total bed porosities (gaseous + solution) in Figure 59 were between 0.35 and 0.48 m^3/m^3. The micaceous sample agglomerated with Cement C also operated at a high steady-state moisture, similar to the sample without cement, since it also contained a high fines content, even though the fines may have been bound together. Both samples were compacted to a bulk density of around 1.6 t/m^3.

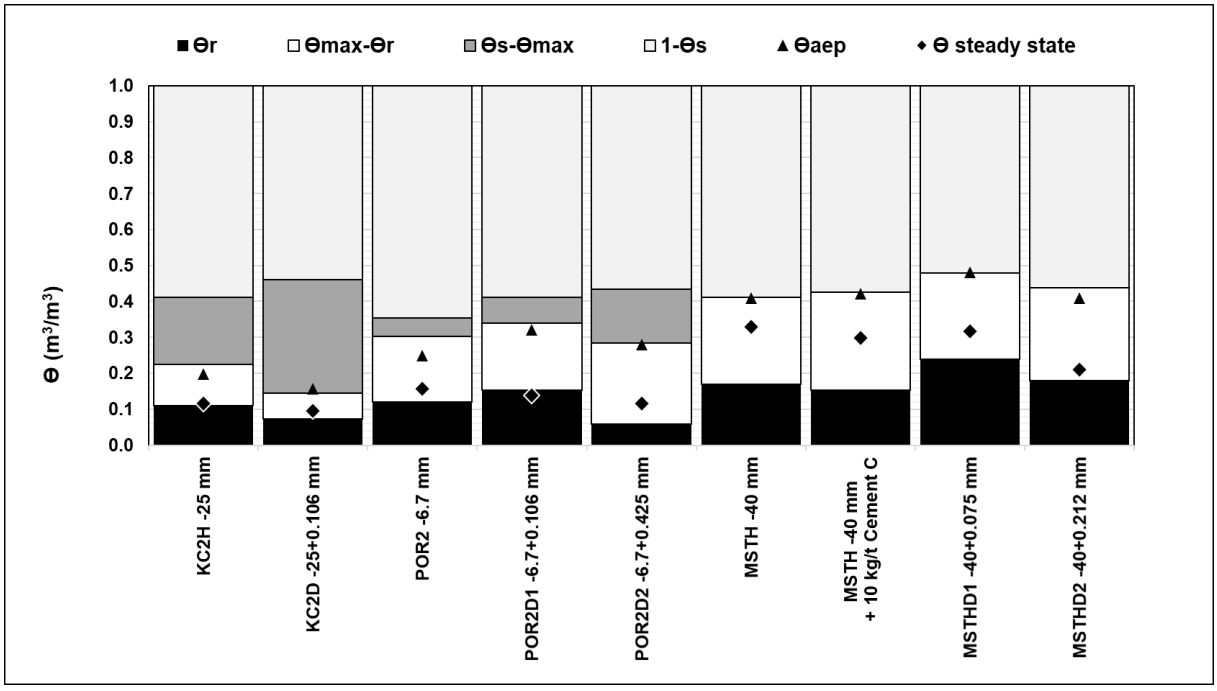

Figure 59. Void fractions versus air entry point and steady state moisture hold-up

The void fraction distributions are plotted in Figure 60 for all the hydrodynamic column tests to date, plotted on the y-axis. The samples on the x-axis are arranged in order of increasing -4.75 mm content. In the majority of cases, especially for the coarser PSDs (to the left of the graph), the steady state moisture hold-up is close to the residual moisture content and is in most cases below 0.2 m^3/m^3. The

micaceous sample (MSTH) operated at a higher steady state moisture (approximately 0.3 m^3/m^3) due to its high sand and clay content, which explains the poor permeability experienced with this sample.

The results also show the close correlation between the air entry point (θ_{aep}) and the inflection point (θ_{max}), which was discussed earlier. In the case where there are no “dead voids”, the air entry point correlates with θ_s. As discussed in the previous section, the percentage “dead voids” ($\theta_s - \theta_{max}$) increases with coarser PSD (to the left of the graph). In other words, samples with larger percentages gravel tend to form more “dead voids”. As the bed moisture content increases, the air spaces become isolated and disconnected, thus also eliminating the existence of continuous free surface flow channels. Continuous flow is now “rate-limited” by saturated flow conditions, and free surfaces where they still exist are in isolated “bubbles".

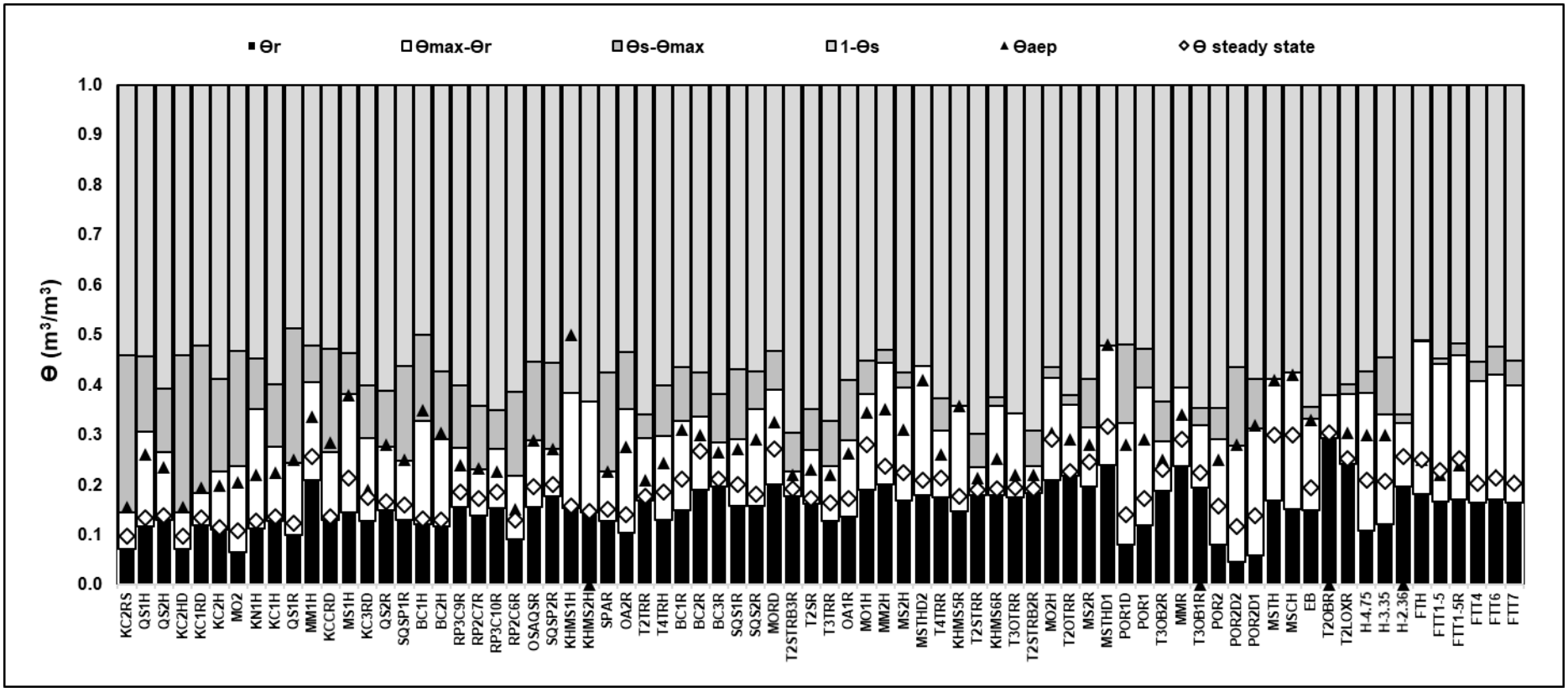

Figure 60. Distribution of void fractions relative to air entry point and steady-state moisture

Although the effect of solute concentration and irrigation pH on the permeability was not part of this research programme, hydrodynamic column tests and uni-axial compression tests were performed with synthetic leach solutions with SG < 1.1. It is anticipated that as the solution circulates over the heap, the concentration of soluble species will build up and hence the solution density and viscosity will increase. Solution through unsaturated heaps normally flows via the meniscus on the surface of the particles, and the thickness of the meniscus is a function of viscosity. Hence at higher viscosity the heap is expected to tie up more process solution (Kappes, 2002). An increase in $MgSO_4$ concentration from 0 M to 0.09 M in water (30°C) was shown to cause an increase of less than 30% in viscosity from 7.9 x 10-4 Pa.s to 10.6 x 10-4 Pa.s (Muhammad and Nadeem, 2022). The density of $MgSO_4$ solutions in water was reported to change from 1.0186 g/cm^3 (2% $MgSO_4$) to 1.2961 g/cm^3 (25% $MgSO_4$) at 20°C (Perry, 1999). Since heap leach solution concentrations are generally lower than conventional hydrometallurgical processes, the effect of salt build-up on the solution density and viscosity is therefore expected to be low.

It is also expected that the resulting increase in surface tension will reduce the ability of the solution to penetrate pores in the rock. The build-up of solutes in the leach solution will also increase with acid strength (decrease in pH), and will contribute to the formation of precipitates, which, together with increased decrepitation at lower pH may contribute to blinding of the heaps (Petersen, 2016).

5.3.3. Column Leach Tests

The column leach test results are summarised in Figures 61 to 69. Copper mass balances are presented in Table 11. Copper dissolutions were calculated from 1) solid head and solution analyses, 2) solid head and residue analyses, and 3) recalculated head and solid residue analyses. The AAS solution assays were used in these calculations. The dissolutions calculated by method 3, which incorporates a 100% copper mass balance (i.e. element out / element in) with respect to both solid and solution phases, are presented as the definitive values here. The copper dissolution profiles in Figure 61 were replotted by recalculated head and solution assays. Accountabilities for copper were between 92.5% and 112% (Table 11).

Irrigation profiles are presented in Figure 62. Deslimed 4 m columns (Tests 6 and 7) were able to accommodate target application rates of 6 L/m^2/h and achieved high copper dissolutions of above 80% after only 60 days of irrigation, with final copper dissolutions of 83.4% and 82%, respectively after 140 days. The addition of curing acid during in agglomeration contributed to initial high rate of copper dissolution rates.

Slumping profiles are presented in Figure 63. The 1 m column loaded without binder (Test 1) and without desliming performed poorly and experienced high slumping (20%). The high slumping in this column reduced the permeability of the bed substantially, such that a maximum irrigation rate of only 1.4 L/m^2/h could be applied before ponding occurred. This in turn limited the rate of acid supply, and

since the copper dissolution is essentially “acid-supply” limited, the copper dissolution rate was slower. The column was stopped after 162 days, at which point the copper dissolution was 43.7%.

The 1 m column loaded with 10 kg/t binder (Cement C) (Test 4), on the other hand, experienced minimal slumping, and was able to conduct irrigation solution at the target application rate of 6 $L/m^2/h$ and achieved high copper dissolutions of above 80% after only 60 days. The final copper dissolution was 88.1% after 141 days. Similar results were obtained with Cements A and B (Tests 2 and 3).

Table 11. Summary of column leach results

Test	Particle Size	Column ID	Height	Binder	Curing Time	Head Grade		Dissolution			Out/In	TAC [6]	NAC [7]
	(mm)	(mm)	(m)		(days)	(%) [1]	(%) [2]	(%) [3]	(%) [4]	(%) [5]	(%)	(kg/t)	(kg/t)
Test 1	-40	160	1	None	28	1.05	0.97	40.4	47.9	43.7	92.5	30.0	23.4
Test 2	-40	160	1	Cement A, 10 kg/t	28	1.05	1.02	85.2	88.1	87.7	97.1	105	91.1
Test 3	-40	160	1	Cement B, 10 kg/t	28	1.05	0.97	79.8	87.6	86.6	92.2	102	89.1
Test 4	-40	160	1	Cement C, 10 kg/t	28	1.05	1.03	86.5	88.3	88.1	98.1	107	93.3
Test 5	-40	320	4	Cement C, 10 kg/t	28	1.05	1.00	86.1	90.4	90.0	95.7	145	131
Test 6	-40+0.075	160	4	98% H_2SO_4, 14.3 kg/t	2	0.71	0.79	93.1	81.4	83.4	112	40	30
Test 7	-40+0.212	160	4	98% H_2SO_4, 14.3 kg/t	2	0.67	0.68	83.2	81.7	82.0	101	36	27

Notes:

1) Assayed copper head grade
2) Recalculated copper head grade
3) Copper dissolutions by solid head and solution analyses
4) Copper dissolutions by solid head and residue analyses
5) Copper dissolutions by recalculated head and residue (or recalculated head and solution) analyses; in other words, for a 100% copper mass balance. These are the definitive copper dissolutions.
6) Total acid consumption
7) Net acid consumption (= Total acid consumption (kg/t) – mass Cu leached (kg/t) / 63 x 98)

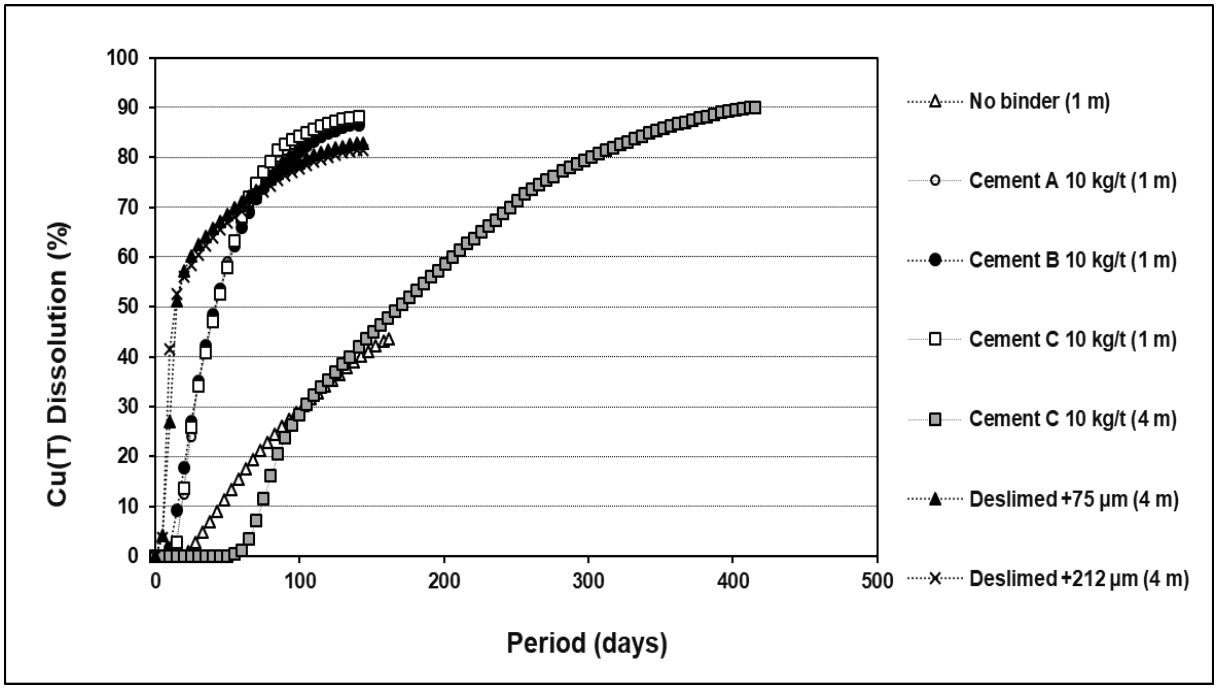

Figure 61. Cu dissolution profiles (micaceous stockpile material)

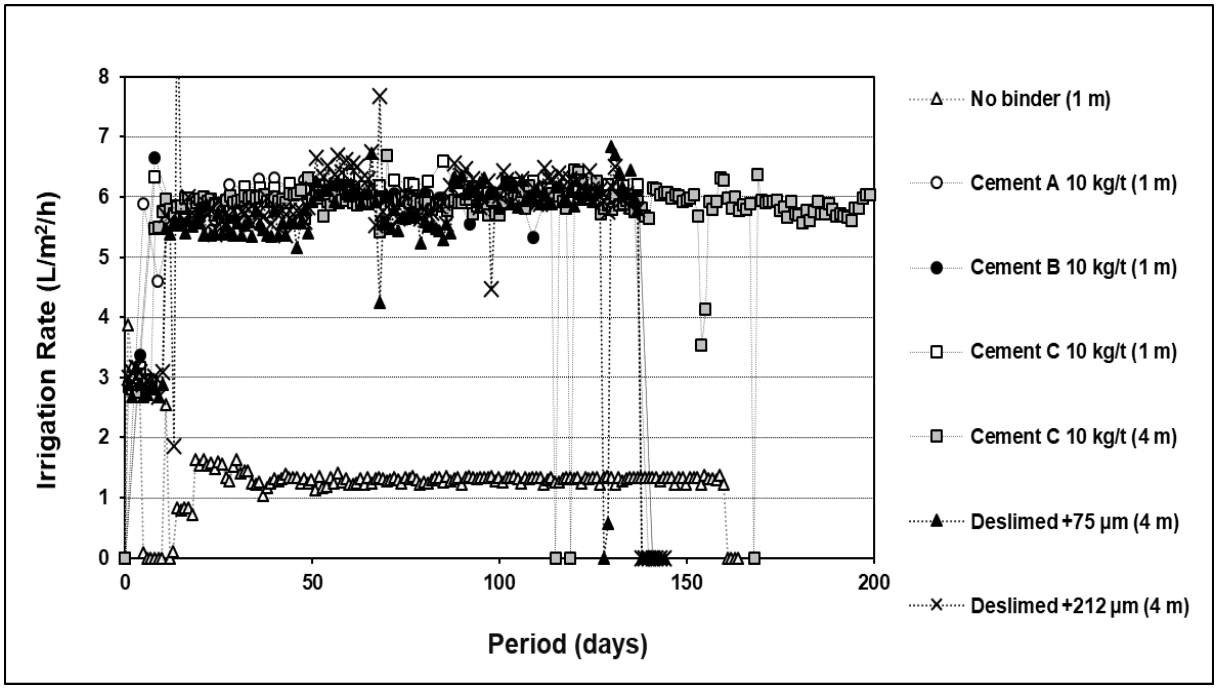

Figure 62. Irrigation rate profiles (micaceous stockpile material)

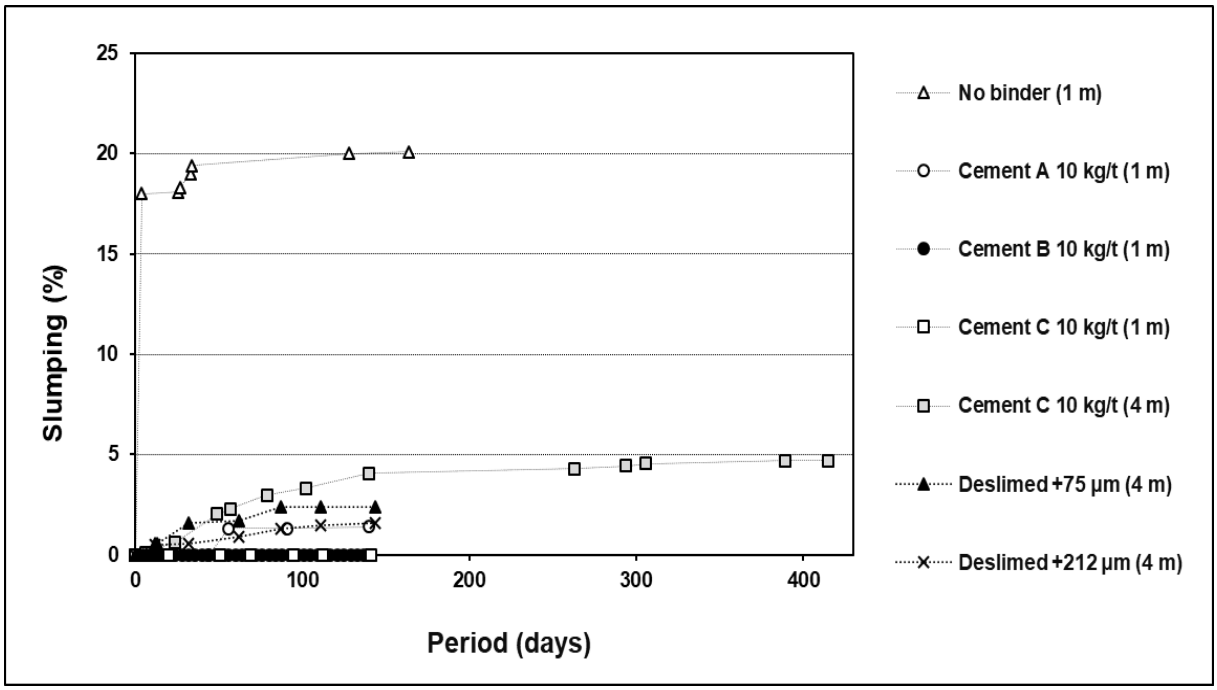

Figure 63. Slumping profiles (micaceous stockpile material)

Drainage pH profiles are presented in Figure 64. Here it can be seen that the taller lift in the 4 m column with binder (Cement C) (Test 5) resulted in a longer delay before the drainage pH was below 6, compared with the other columns. As a result the copper only started appearing in the drainage after approximately 50 days. This is approximately 4 times longer than in the corresponding 1 m column (Test 4), where the copper started appearing after 12 days, corresponding to the 4 times taller lift. The leach time in the 4 m column (Test 5) is also longer than in the corresponding 1 m column (Test 4) due to the taller lift. A final copper dissolution of 90% was obtained after 415 days, with the slumping remaining below 5% (Test 5).

The ore / binder mixture has high alkalinity, with the initial drainage pH rising as high as 12 in the 4 m column (Test 5). The initial drainage pH in the 1 m columns rose to about pH 8 whether binder was used or not (Tests 1, 3 and 4). An exception was Test 2 (Cement A), where the initial drainage pH rose to 12. Hence it appears the binder does not contribute significant to the alkalinity (except for Cement A), which contained a higher percentage of clinker.

In the case of the deslimed 4 m columns (Tests 6 and 7), acid was added during curing, and copper came out immediately, as the acid-soluble copper dissolved in the cure washes out as soon as irrigation is commenced. This highlights one of the disadvantages of the binder / agglomeration process, in that acid is not added in agglomeration, resulting in slower initial copper dissolutions compared with the deslimed columns.

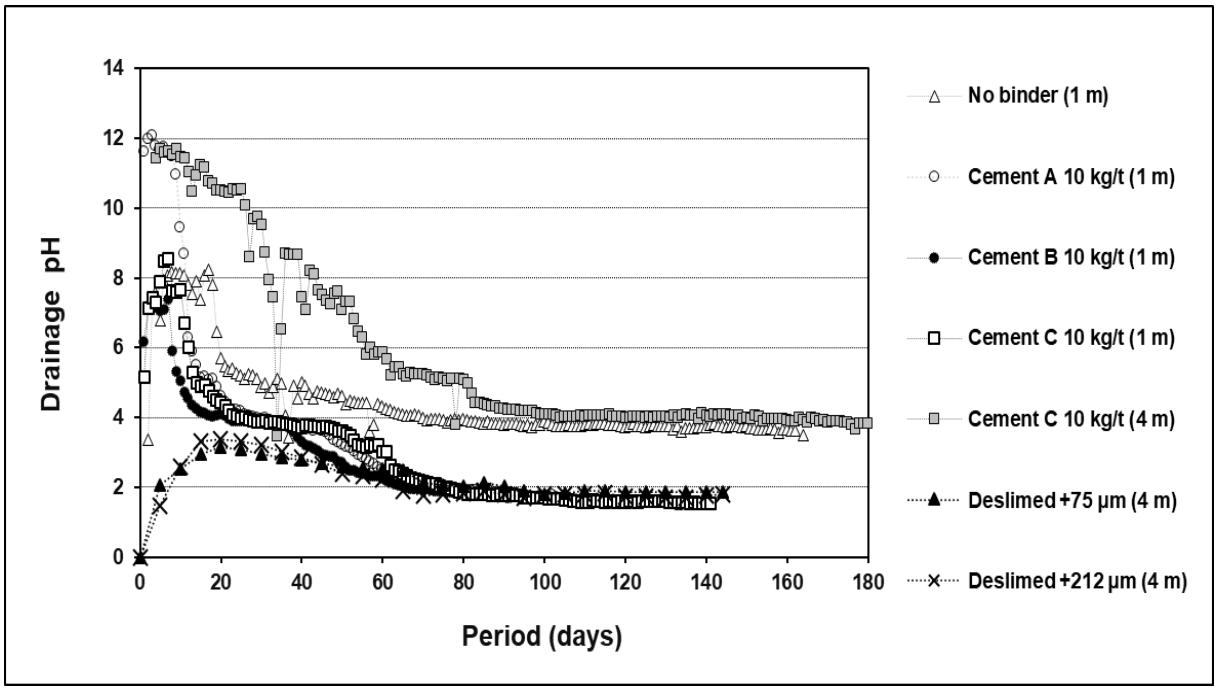

Figure 64. Drainage pH profiles (micaceous stockpile material)

The apparent copper dissolutions of the deslimed micaceous samples were 83.4% (-40+0.075 mm) and 82% (-40+0.212 mm), based on the recalculated copper head grades of the deslimed materials (0.79% and 0.68%, respectively) as indicated in Table 11. However, due to the large mass loss during desliming, the actual copper recoveries are only 27.2% (-40+0.075 mm) and 16.9% (-40+0.212 mm) if it is based on the original ore mass and copper head grade (1.05%).

This is further illustrated in Figure 65, which indicates that, as is often the case, the valuable metal grades are higher in the fine fractions. For the MSTH sample, 67.4% of Cu reports to the -0.075 mm fraction, with 12.1% reporting to the -0.212 +0.075 mm fraction. Hence desliming or size segregation causes disproportionate losses of the valuable metal to the fine fractions. This highlights one of the disadvantages of desliming as a means of improving permeability.

The high metal losses to the fines fraction during desliming and the high costs to construct an agitated tank leach plant to treat the fines make this process route unattractive. Furthermore, it is also not clear how the desliming will be performed on an industrial scale. The current industrial practice of dry screening normally targets a higher screen size (*e.g.* 0.6 mm) and not the lower cut sizes described in this thesis.

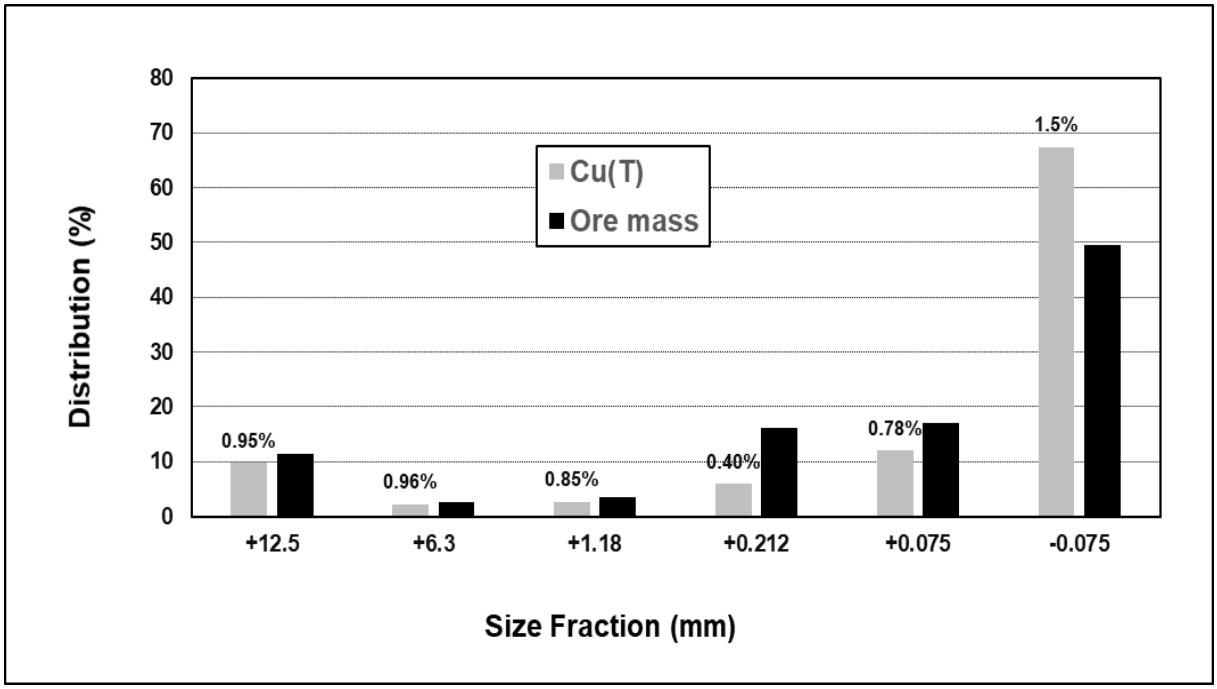

Figure 65. Cu distribution and grades per size fraction (MSTH)

Net acid consumption (NAC) curves are plotted against copper dissolutions in Figure 66. Lower overall net acid consumptions (27 kg/t and 30 kg/t, respectively) were obtained in the deslimed columns compared with the agglomerated samples. The lower overall NAC obtained in the deslimed columns can be explained by the removal of fines, which contain higher surface area and therefore consume more acid. Furthermore, as highlighted in Figure 65, the finer fractions also contain more copper, which would also contribute to a higher acid consumption if they had leached as mica.

The 1 m column without binder (Test 1), when compared with the 1 m column with binder (Cement C) (Test 4), had similar NACs (23 kg/t) up to 43.7% Cu dissolution, at which point the column without binder was stopped. This seems to indicate that the binder does not add significantly to the acid consumption. By way of illustration, using a CaO content of 63.2% for the OPC component of the binder, and assuming that all of that is consumed during the leach by sulphuric acid (H_2SO_4) according to Equation 51, a hypothetical contribution of the binder to the total acid consumption (TAC) can be determined for Cements A (7.07 kg/t), B (4.2 kg/t) and C (5.53 kg/t), respectively at a dosage of 10 kg/t. This number is <10% of the TAC for the three 1 m columns where binder was used (105 kg/t, 102 kg/t and 107 k/gt) (Table 11).

$$CaO + H_2SO_4 = CaSO_4 + H_2O \quad (51)$$

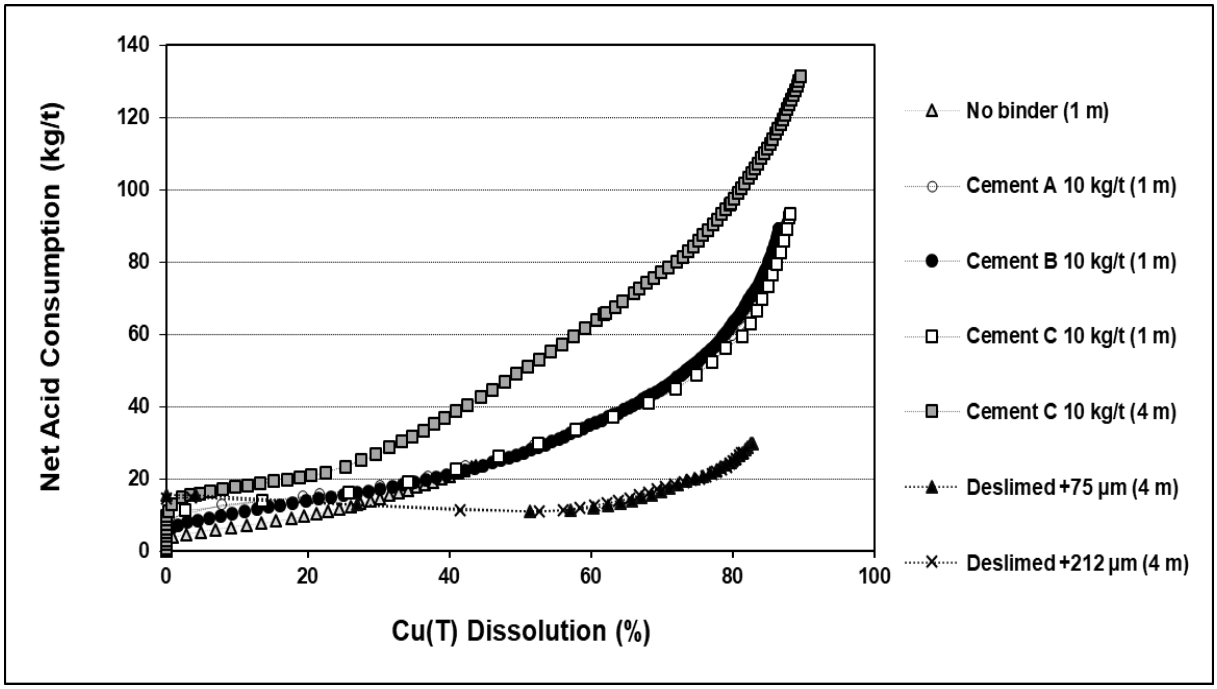

Figure 66. Net acid consumption versus copper dissolution (micaceous stockpile material)

Net acid consumption profiles against leach time are also presented in Figure 67. The 1 m column with Cement C (Test 4) was irrigated up to a total leach cycle of 141 days, at which point the NAC was 93.3 kg/t (TAC = 107 kg/t). Although one would expect the NAC per ton ore in the taller column (Test 5) to be the same as the 1 m column (Test 4), this was in fact not the case. The 4 m column with Cement C (Test 5) had a higher overall acid consumption, since the feed acid concentration was raised from 8 g/L to 15 g/L after 53 days in order to reduce the pH to below 4 in the drainage (to prevent copper precipitation). The final NAC was 131 kg/t (TAC = 145 kg/t) after 415 days.

The steady-state moisture hold-up and degree of saturation are presented in Figure 68 and 69, respectively. The steady-state moisture content was calculated, assuming constant solids mass, from masses of solution irrigated and drained on a daily basis, incorporating the moisture added in agglomeration. In order to improve the accuracy of these plots, the final moisture after drain-down was determined by drying the residue cake. The cake moisture and mass of solution drained immediately after irrigation was stopped, were used to back-calculate the moisture hold-up before irrigation was stopped. Both graphs (Figures 68 and 69) were normalised based on the final cake moisture. As can be seen in Figure 68, most columns operated close to 20% moisture, except for the sample deslimed at 212 µm. All the columns operated well below the target of 85% saturation, except for Test 1, which operated close to the 85% on account of the high bed compaction, resulting in the lower maximum irrigation rate that could be accommodated. Furthermore, wall effects always play a more prominent role in columns so that slumping may be higher in the field.

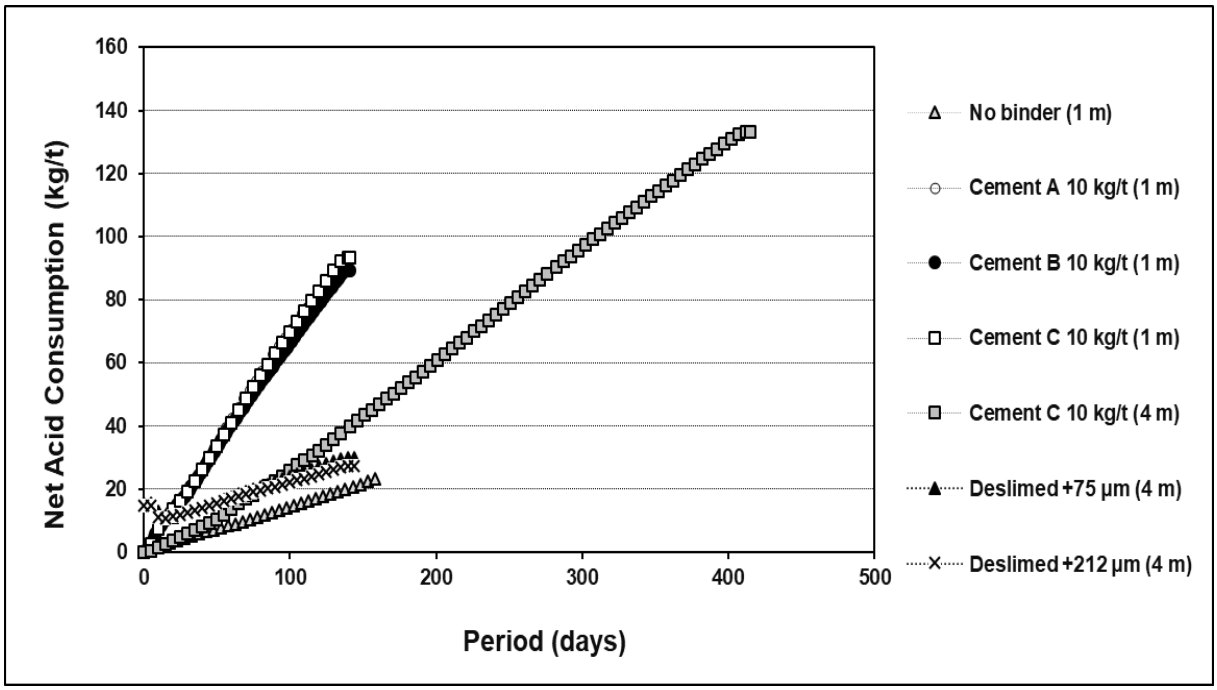

Figure 67. Net acid consumption profiles (micaceous stockpile material)

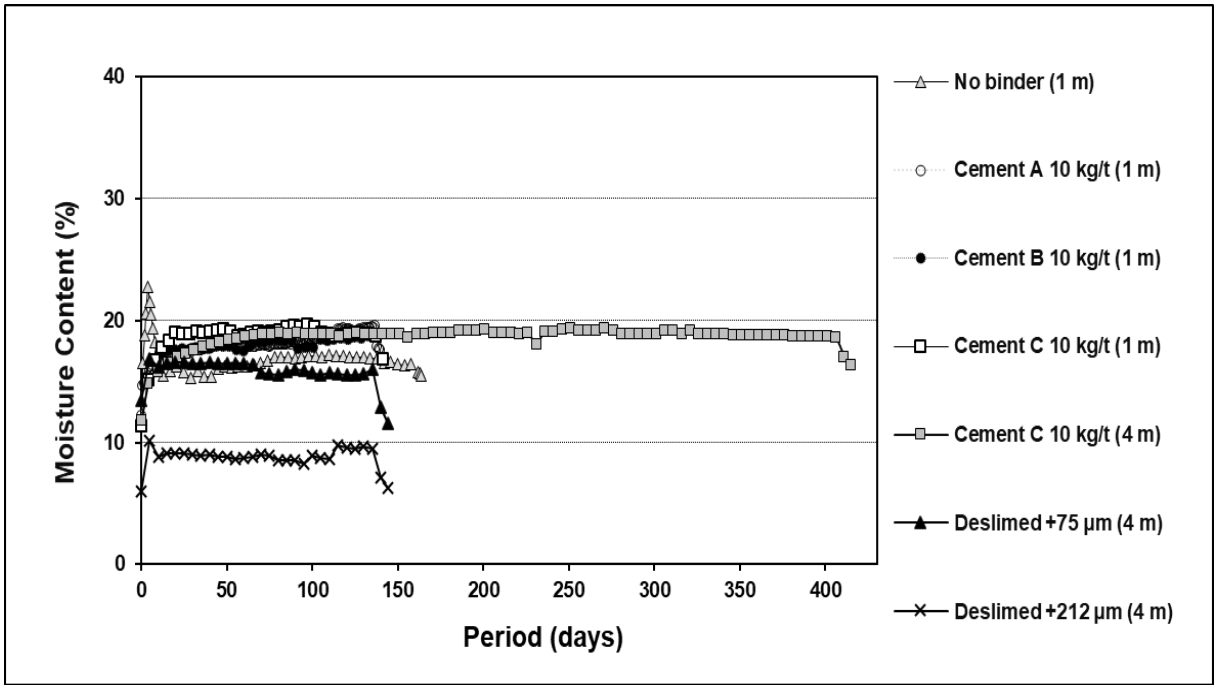

Figure 68. Moisture content profiles (micaceous stockpile material)

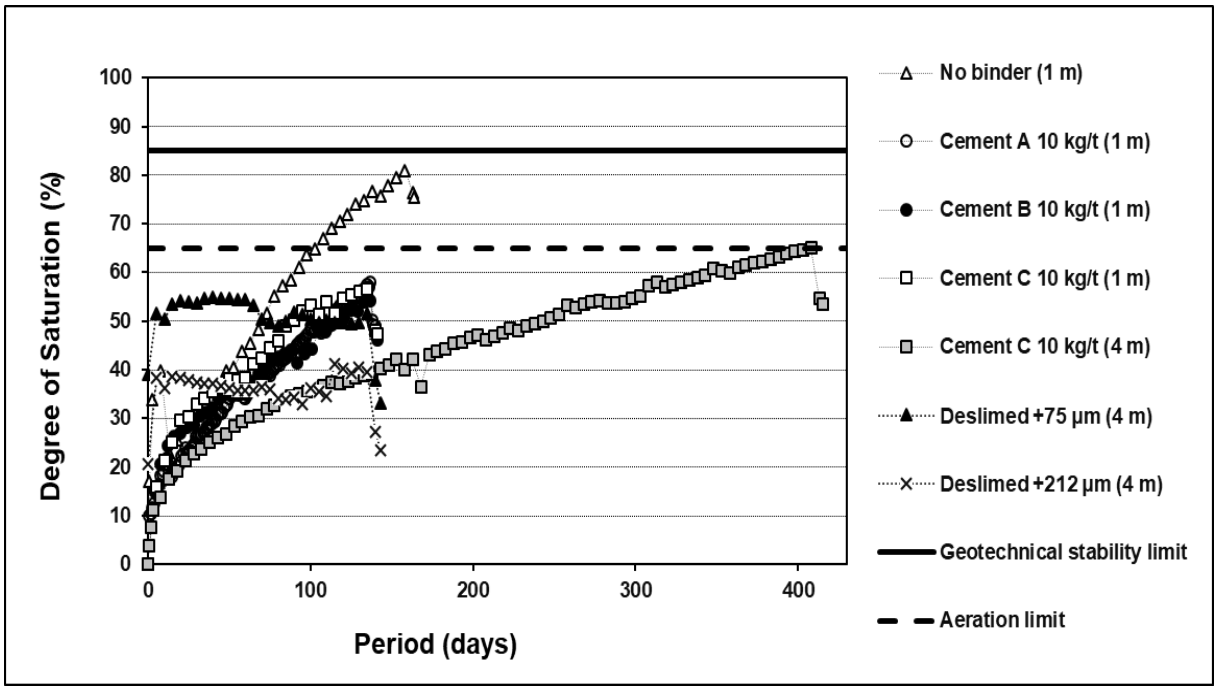

Figure 69. Degree of saturation profiles (micaceous stockpile material)

Figure 70 shows the distribution of void fractions in the leach columns containing the various deslimed and cement-agglomerated samples of the MSTH ore, prior to the point at which the irrigation was stopped. The untreated whole ore sample (agglomerated with water and no binder) (Test 1) had a much lower total porosity compared with the other columns, due to the high degree of slumping (20%). The steady-state moisture hold-up prior to drain-down was thus closer to saturation than in the other columns. This explains why the whole ore column without binder performed poorly and was only able to achieve a maximum irrigation rate of 1.4 L/m^2/h.

The samples agglomerated with cementitious binder slumped to a much lower degree compared with Test 1, even though they had similar fines contents and moisture hold-ups. Thereby a higher bed porosity was maintained and therefore they operated further away from saturation. This effect may, however, be less pronounced in the field, where greater compaction may occur during stacking. The fact that using cement works in the field for gold heap leach operations in alkali medium suggests that it may also work in acid medium if the bonds are not destroyed when exposed to acid. This seems to be supported by the fact that the binder did not contribute significantly to the alkalinity / acid consumption, seeming to indicate that pozzolanic bonds were not destroyed.

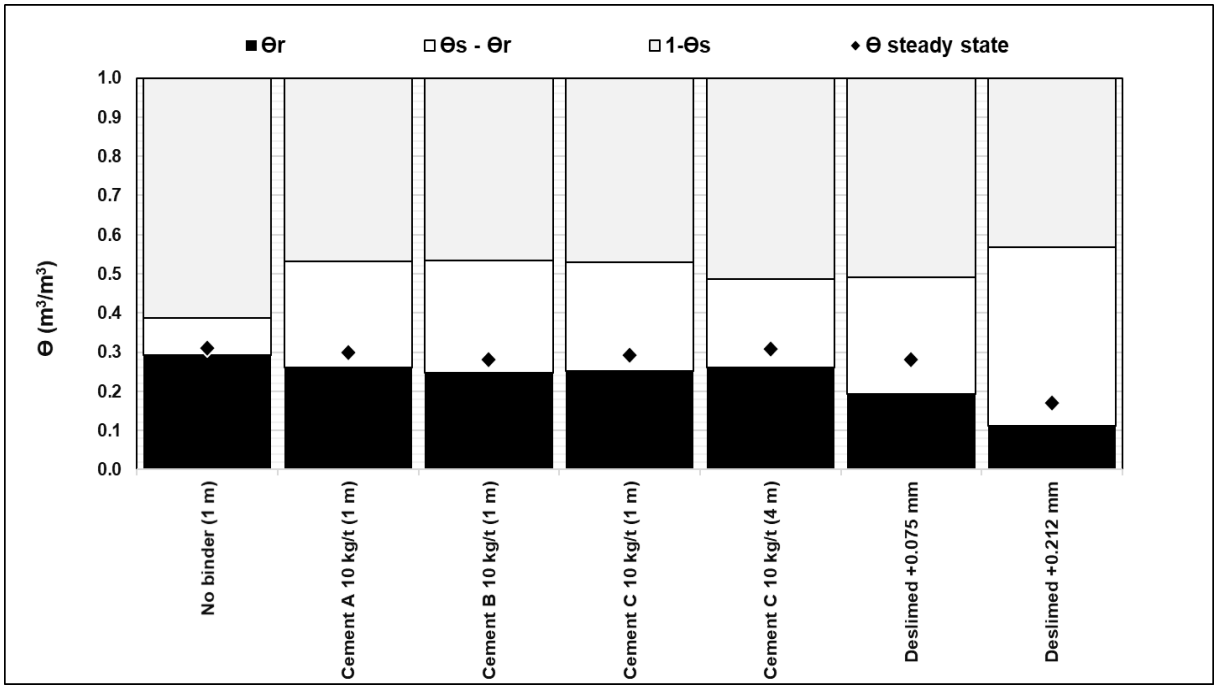

Figure 70. Void fractions versus steady state moisture hold-up (micaceous stockpile material)

A quick estimate of the cost of the binder was made, assuming an average binder cost of US $ 100 / t, a sulphuric acid cost of US $ 250 / t and ignoring the reagent transport costs. Assuming a head grade of 1% Cu and a copper dissolution of 80% as per the micaceous stockpile material, and a copper price of US $ 6000 / t, this translates into a revenue of US $ 48 / t ore. Alternatively, assuming a flotation cut-off grade of 0.5% soluble Cu, this translates to a revenue of US $ 24 / t ore. For the micaceous stockpile material, the binder dosage was 10 kg/t, which translates into a cost of US $ 1 / t ore. The hypothetical contribution of the Binder C to the total acid consumption was calculated above as 7.07 kg/t, which translates into a cost of US $ 1.8 / t ore treated. The cost of binder plus additional acid is then US $ 2.8 / t ore treated, or between 5.8% and 11.5% of the recoverable copper value for the two head grades above.

It is therefore concluded that the binder may provide a more cost-effective method for treatment of low-permeability ores than desliming, where there are large losses of the target mineral to the fines fraction, and the costs of building an auxiliary tank leach plant to process the fines may be prohibitive, especially for small operations and perceived high-risk investment regimes. Nonetheless, the figure below shows the commercial heaps for the Moxico micaceous oxide material, which was shown in column tests to require desliming in order to achieve suitable permeability (MO2H).

Although detailed information regarding the commercial heaps is not available, it is assumed that these operate with desliming. However, the binder test work showed that this may be a more cost-effective way of operating, however, at the time, the binder technology was not yet offered to the client since it was still being patented.

Figure 71. Mimbula oxide heap leach pads [www.moxicoresources.com/projects/republic-of-zambia/operations; accessed 29.09.2023 with permission Moxico Resources plc]

5.3.4. Mineralogy

Images of the sample agglomerated with water only (Test 1) is shown in Figure 72, indicating natural agglomeration of fines with water in the absence of binder. The fines in the sample were found in depressions in the quartz, however, the packing of the fines is a lot “looser” than the mixtures where cement was added. Mica phases do not display any deformation in this sample and the clay hosts less than 1 % Mg.

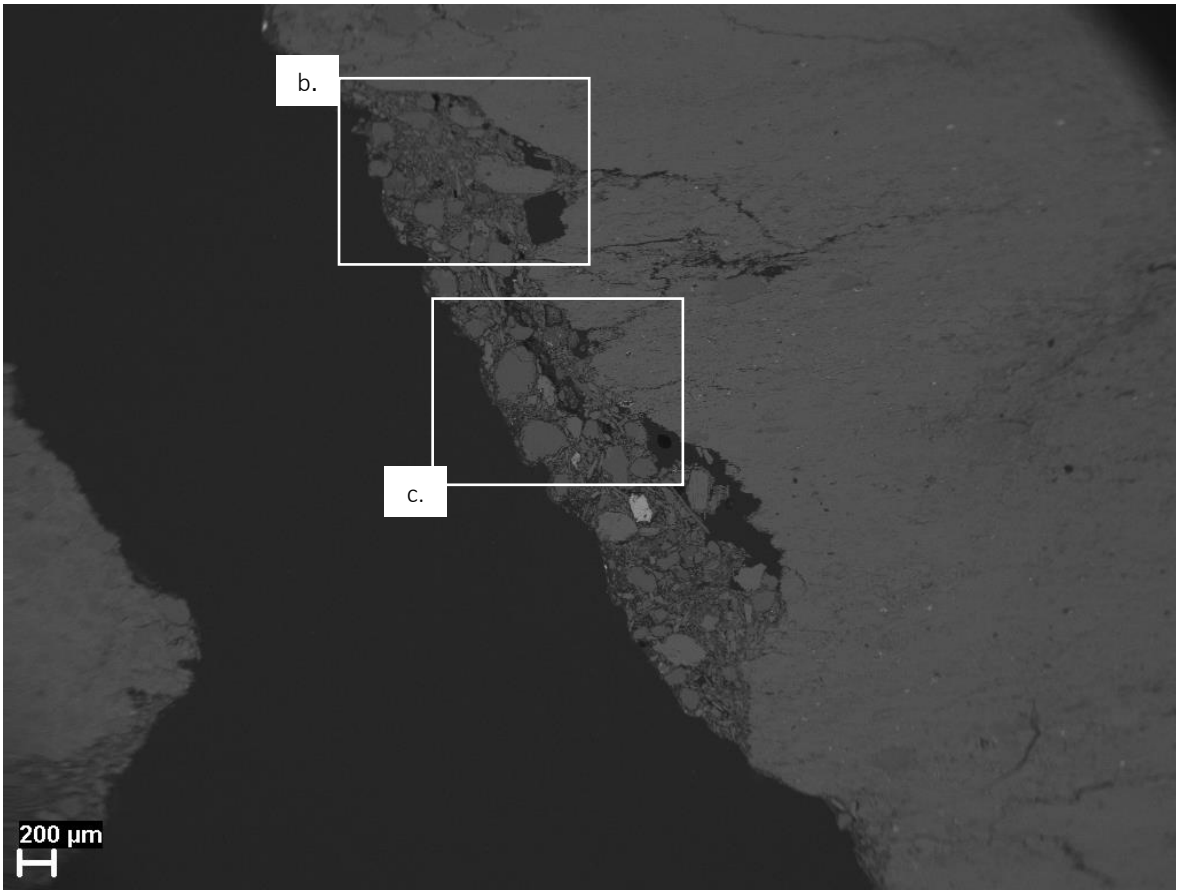

a.

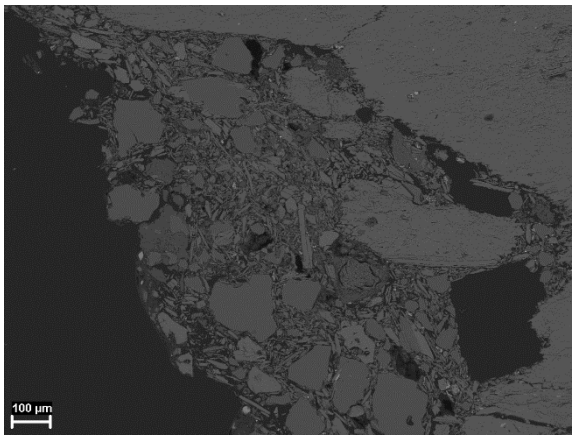

b.

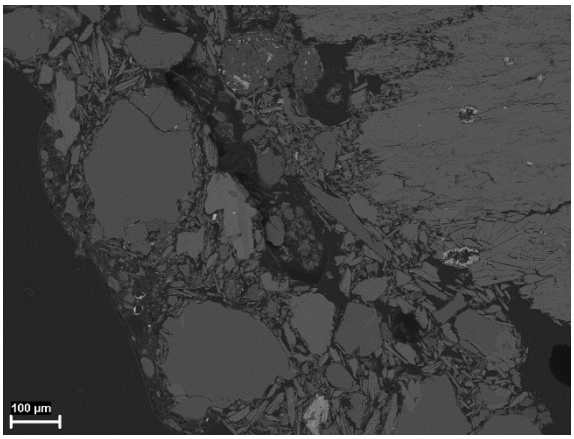

c.

Figure 72. Back-scattered electron images of sample Test 1 head (a) Overview of selected particle, with box denoting area selected for closer examination. (b) and (c) Areas selected for closer examination.

In feed agglomerates where cement was used, on the other hand, agglomerates are coarse (>1 mm in diameter) (Figure 73). They are rounded to sub-rounded in shape. The phases occur in a mosaic-like pattern with obvious porosity. Phases identified upon close examination were quartz, feldspar, mica (Mg-rich and Mg-poor) and clay – Mg-deficient and Mg-hosting. The clay is the cementing / binding agent to the other gangue phases from the ore sample. Within the agglomerate, this phase has broken down into very fine masses, which occur between the particles of ore minerals. These masses are noted to occur along the rims of quartz and feldspar and appear to have caused a physical deformation of the micas.

The agglomeration mechanism appears to be that of a reacted form of clay acting as a binding / cementing agent to bind together to the gangue phases (e.g. quartz, feldspar or mica), forming tightly bound agglomerates (Figure 73a), or coatings onto larger quartz particles (Figure 73b). Within the agglomerate, this clay is very fine in nature, and appears to have caused a physical deformation when bonded, particularly with mica. Compositionally, the binder hosts kaolinitic components Al, Si and O, while Mg was detected up to 4% (Figure 74). Ca components from the original cement were not detected by the techniques used, suggesting low concentrations present in the clay binders.

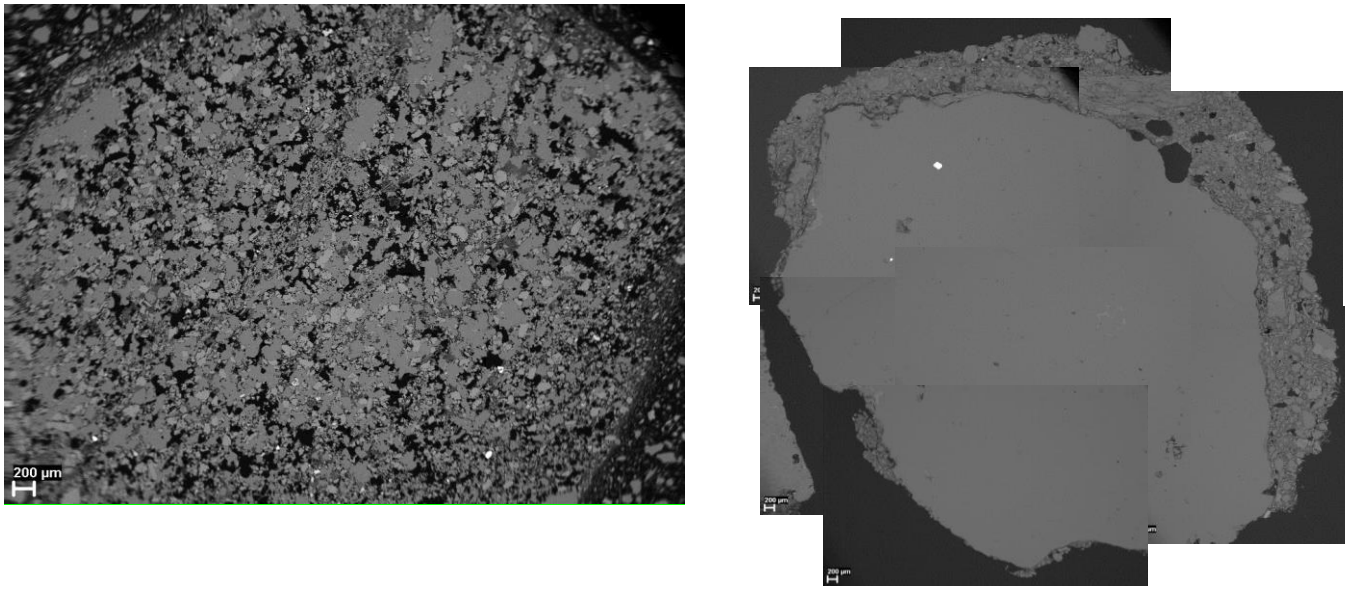

a. *b.*

Figure 73. Mosaic (a) and rim (b) agglomerates formed from agglomeration of feed ore, cement and water.

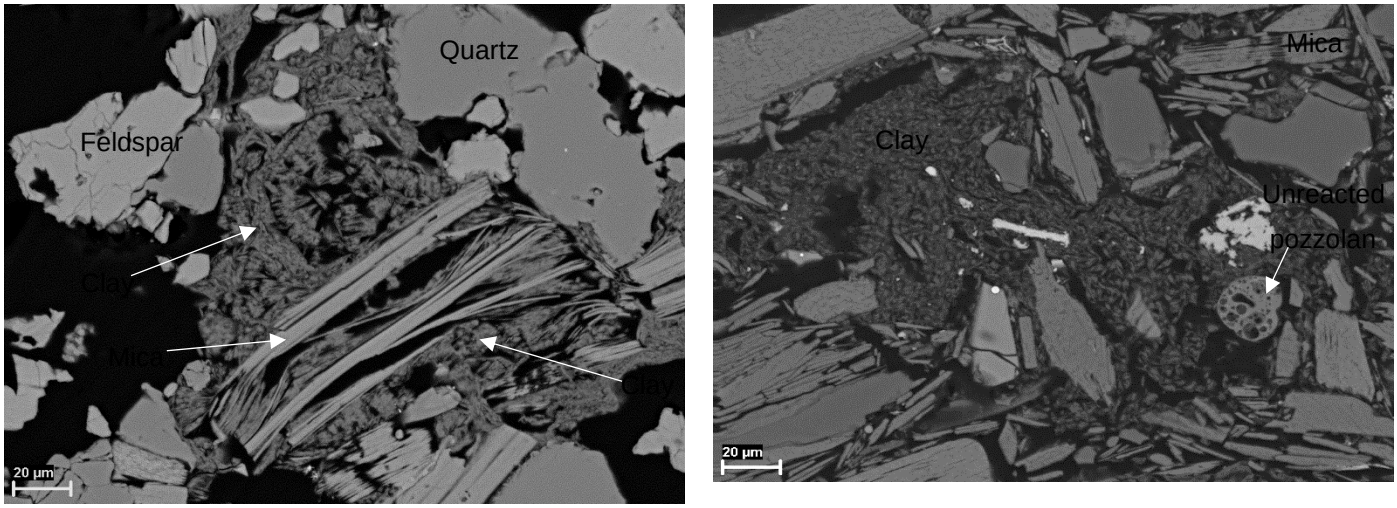

a. *b.*

Figure 74. Back-scattered electron images of clay binder around ore minerals (a) and indicating an unreacted pozzolan (b).

Column leach residue sample (Test 2) comprised quartz as the main component, with subordinate clay, mica, feldspar and chlorite (Figure 75). Examination of residues showed a few instances of clay binder – this phase has the composition of kaolinite and hosts up to 4% Mg. In the samples examined in this study it is clear that Al- and Si-minerals have reacted to form binding agents for the ores. It may be that kaolinite from the original ore reacted with the cement during initial agglomeration, itself undergoing dehydration and absorption of Mg. Hardening results from various chemical reactions between the calcium aluminates (in cement) and silicates present and water. During leaching, these structures appear to have held firm, thus contributing to geomechanical stability of the agglomerates in the leach column.

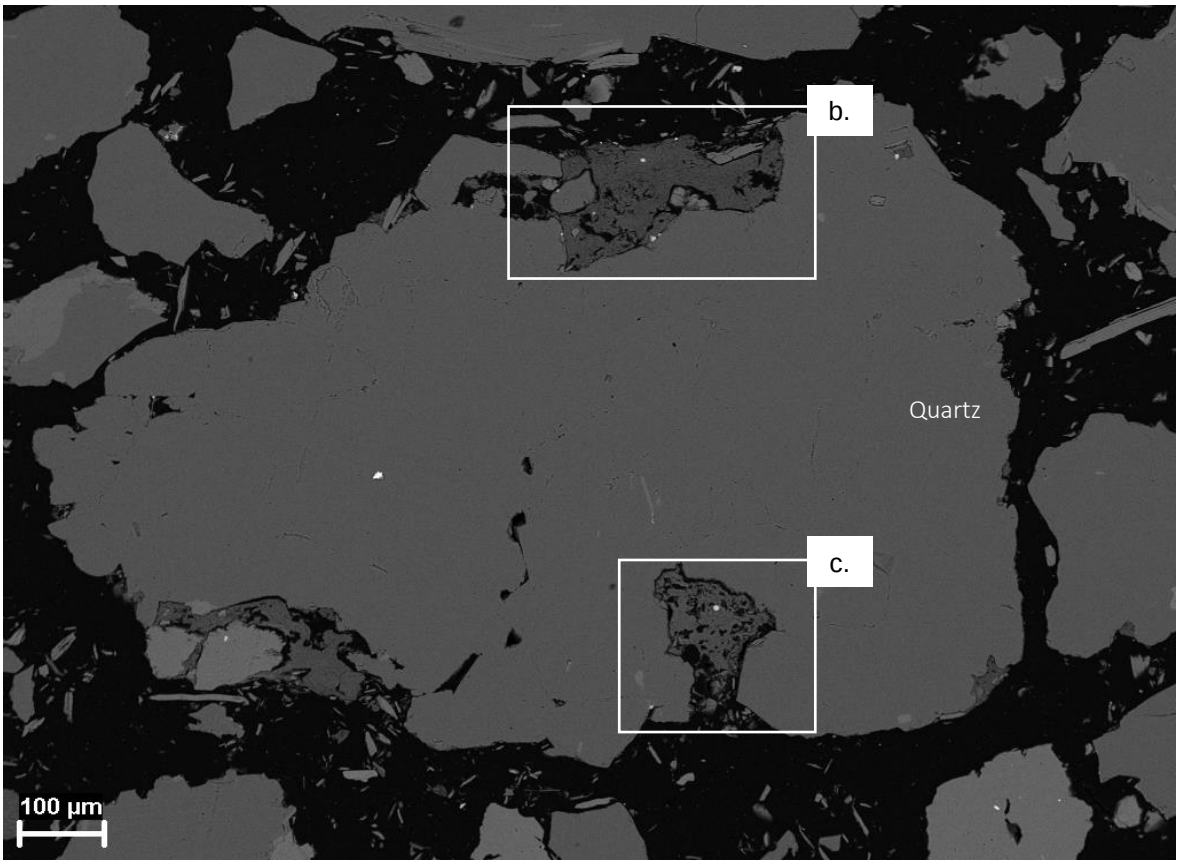

a.

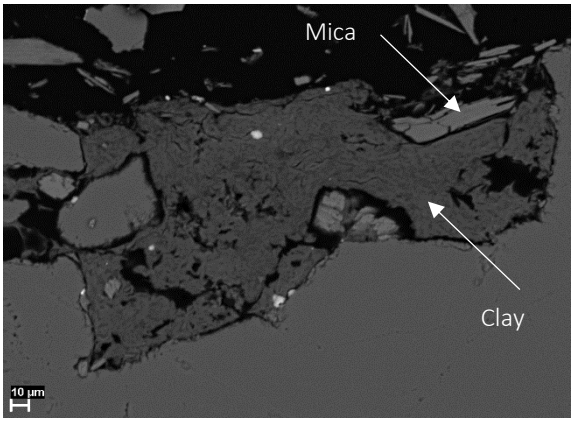

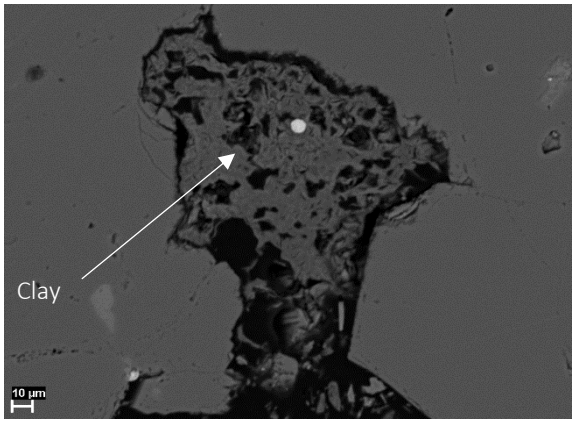

b. c.

Figure 75. Back-scattered electron images of selected areas in sample Test 2 residue. (a) Overview image with areas of interest highlighted in the white boxes and shown in images (b) and (c) showing clay binder around ore minerals in the leach residue.

6. CONCLUSIONS AND RECOMMENDATIONS

The development of hydrological and physical test protocols for testing heap leach ores is an important step in advancing the design of heap leach operations and reducing the risk associated with new projects. If the ore is not able to efficiently support the leach process under given conditions of crush size, lift height, solution application rate and agglomeration technique, this indicates that alternative ore preparation approaches such as coarser crush size, blending or improved agglomeration techniques should be employed. In particular, the uni-axial compression tests also allow an estimation of the stacking height that may be accommodated, and poor permeability may require the use of lower heap heights (with adverse effect on the economics of the process). If problems with permeability persist, it may even be recommended not to proceed with the project, or to look for an alternative processing route. However, this research aims to provide a more fundamental basis for the test protocols and to reduce reliance on “rules of thumb”. In this work novel ways of representing the data, such as the distribution of void fractions in the bed, were incorporated. This representation provides further valuable insights and assists in interpreting the data and has been adapted to represent column leach tests.

6.1. Effect of physical properties on saturated hydraulic conductivity and application of packed bed theory

The study found that a packed bed model (modified Carman-Kozeny) is suitable to represent saturated solution flow through the bed. A method was also devised whereby the tortuosities could be calculated from the experimentally determined saturated hydraulic conductivity and the hydraulic radius calculated from the PSD surface areas. A D_{min} of 0.2 mm provided the best agreement with literature values and yielded tortuosities of between 1.48 and 4.44. The results support the hypothesis that very fine particles (in this case below 200 µm) do not contribute to the surface area exposed to irrigation solution but bind together or onto coarser rocks or are suspended in liquid.

The hydraulic radius concept proved convenient when representing the bed as a collection of spheres of different diameters which may be described as a packed bed. This allows packed bed theory to be adapted for heap leach ores and agglomerates, although only when measuring saturated flow conditions. The minimum diameter of 200 µm was not directly measured but inferred from the data. Hence this is something that could be further investigated. Hydraulic radii determined from saturated solution flows were between 12 µm and 73 µm assuming a tortuosity of 1.4 (the theoretical minimum for a packing of ideal spheres). This does not vary much from the hydraulic radii of the coarse sandy samples (-4.75 mm) in this test work programme, which were between 15 µm and 25 µm. This suggests that coarser particles do not contribute as much to the formation of flow channels as one would expect, supporting the hypothesis of the formation of “dead voids”.

6.2. Effect of particle size distribution on residual moisture hold-up

The residual moisture (after drain-down) was related to the proportion of sand (-4.75 mm) in the bed and to a spherical approximation of the particle surface area. This may be correlated with the Bond number, which is close to 1 for a particle diameter close to 4 mm (assuming a sub-section of the bed containing uniform 4 mm diameter spheres). Hence the percentage sand is also an indicator of the residual moisture that will be retained in the bed, as the presence of fine material reduces the inter-pore spaces and increases the available surface area. As the particles diameter becomes larger than 4 mm, the Bond number increases by the square of the particle diameter, such that the gravitational forces quickly dominate the capillary forces and the moisture drains out. This is important in terms of quantifying losses of water to the leach residues, especially in arid regions such as the Atacama desert (Chile) and Arizona (USA). Samples with high clay content such as laterites have also been reported to contain high residual moisture contents which makes handling of the residues difficult. The lower moisture losses associated with heap leaching also make this technology preferable over other technologies such as flotation, where the sample is finely milled and the residues therefore contain higher moisture contents.

6.3. Applicability of traditional capillary soil science to model hydraulic conductivity and air conductivity functions

Whereas unsaturated flow models have been applied almost exclusively to material containing lower particle sizes (*e.g.* clay -0.002 mm, silt 0.002-0.075 mm and sand 0.075-2 mm), typical heap leach material spans a wider range, with top sizes typically between 6 mm and 25 mm. If one assumes the smaller particles (-0.2 mm) clump together or adhere to larger particles and do not contribute individually to the surface area, the particle size range becomes narrower.

It is proposed that traditional capillary models, such as BC and VGM, may be applied to coarser heap leach samples at lower flowrates. The hydraulic conductivity function should however be described as a discontinuous J-curve, rather than a continuous J-curve with a fitted saturated hydraulic conductivity value as was recommended by previous authors. The VGM fit is popular since it provides a closed-form, continuous function suitable for mathematical models. Furthermore, most of the work publicised to date has been done on sand, where the effect of “dead voids” will be less important. However, the results obtained in the laboratory do not suggest dual-porosity flow and indicate that flow is governed by capillary forces up to the air entry point (a single discontinuous VGM curve). However, the conventional approach to modelling heap leach data, which comprises measuring the WRC and K_s, and then using the VGM model to predict the HCF curve, is unsatisfactory. The benefit of measuring both the HCF and the K_s was demonstrated in this work as well as the importance of performing hydrodynamic column tests.

At higher flowrates, there is a discontinuity between the saturated hydraulic conductivity and the lower portion of the graph governed by capillary flow. This is explained by the fact that, as the flowrate increases, the flow channels increase and the pores fill up, to the point where the maximum flow rate is

reached. Above this point, the moisture content increases further, without additional increase in flowrate, due to the presence of “dead voids” (poorly connected macro-pores) which fill up but do not create more flow channels. This explanation fits the data better than a transition from capillary- to gravity-controlled flow, as has been proposed by a number of authors. For example, if the transition was from capillary flow to gravity flow, the K_r value would show an upwards trend rather than flatten off above the transition point, since K_s of the gravity controlled macro-pores would be greater than the K_s of the fine-grained micro-pores. Furthermore, this explanation seems to be confirmed by fact that the air entry point and the point of discontinuity coincide. In other words, as the moisture content increases, additional pore spaces are filled up, but since they are not connected, no additional flow channels are created.

The use of “dual porosity” as a blanket explanation to describe the discontinuity in the HCF curve is incorrect, especially since test work in smaller columns tend to be more homogeneous. However, the author does not discount the presence or importance of dual porosity in heap leach operations at a larger scale. The change in homogeneity during scale-up was not the focus of this investigation and is something that needs to be addressed with respect to diffusional radii and dripper spacings.

The data also show an increase in the proportion of “dead voids” with *decreasing* fines content, suggesting that coarser particles contribute to the formation of “dead voids”. This is counter-intuitive, as one would expect the presence of coarser rocks to contribute to the formation of larger channels, which would enhance aeration. The experiential rule that recommends that the void saturation should not exceed 65% for heap aeration appears to correlate with the average of the data points and seems to be validated by the data. The research does not contradict the current “experiential rule” of <60% to 65% saturation, since the rule on average provides a good estimate of the degree of saturation above which aeration drops off over a range of samples tested. Also, for the first time, the manner in which the underlying fundamentals give rise to the quantities associated with these rules of thumb has now been revealed. A 65% saturation corresponds on average with the air entry point (the maximum solution moisture at which air can still just pass through the bed, or at which the air conductivity drops off completely as the bed becomes more saturated). The presence of dead voids further reduces the percentage of the bed that is available for solution and air flow. This is a very interesting and a novel finding and has important implications for heap design. For example, it implies that aeration is not necessarily improved by a coarser crush. It is expected that a better graded sample will also have better connected pores and less dead void volumes.

The research shows that only a portion of the bed voidage is connected to flow paths and therefore available for air and solution flow. However, the 60% to 65% rule does not apply universally, for example for coarse samples, the proportion of the void space available for air and solution flow decreases even further below 60%, whereas for sandy ores, almost the entire void space is available for solution flow. Hence, during hydrodynamic column tests it is best to measure the air entry point rather than choose the 65% saturation point.

Furthermore, gas conductivities in the presence of two phases (solution and gas), with the gas phase mobile and the solution phase stagnant was modelled with Darcy's law combined with the Carman-Kozeny equation. The air entry point can be determined by fitting the air permeability curves with traditional capillary models such as van Genuchten-Mualem.

6.4. Treatment of low permeability ores with desliming and agglomeration with cementitious binder

The compressibility of agglomerates under load was found to correlate with the percentage of -2 mm material in the PSD. High contents of silt and clay result in the destruction of porosity under load to the extent where the bed becomes impermeable. Low permeability is therefore generally associated with a large percentage silt, clay and fine sand.

A few practical interventions which can be applied to manipulate the effective PSD were discussed, including a novel approach of using cement-based binders, despite the fact that unmodified Portland cement is normally reactive to the acidic environment of copper leaching. Poor permeability was shown to result from a high steady-state moisture hold-up in the bed, caused by a high fines content combined with a reduction of porosity due to compression and slumping after wetting. This results in the bed operating close to saturation, resulting in ponding and a low maximum solution application rate. Where the leach rate is reagent (acid) supply limited, this invariably results in lower copper dissolution rates.

Both desliming and agglomeration with a modified cementitious binder were successful in improving the hydrology of low-permeability ores. In both cases the result is a decrease in compressibility and slumping. During desliming, fines are removed, also resulting in a lower steady-state moisture hold-up, so that the bed operates further from saturation. This reduces ponding and allows higher maximum irrigation rates.

The cementitious binder caused a reduction in slumping after initial wetting in the leach columns. The slumping did not increase during prolonged exposure to dilute sulphuric acid in the leach columns, suggesting that the cementitious bonds do not break in the presence of acid. The binder also does not inhibit the dissolution of copper from the agglomerated ore matrix, since both columns with and without binder yielded similar final copper dissolutions. Since acid cannot be added during agglomeration with binder, addition of binder significantly delays the release of copper compared with a process where acid is added in agglomeration. Although mineralogy indicates the disappearance of the clay "binder" phase between the head to residue, there is no evidence that the binder increases the acid consumption significantly, both in terms of initial pH rise in the PLS and initial acid consumption measured in 1 m columns (except for Cement A which has a higher percentage clinker).

The mechanism is proposed to be the binding together of finer particles or onto larger rocks. These bonds break down in the absence of binder, but if binder is used the structures do not disintegrate, so that adequate porosity is maintained. As it was also proposed that -200 µm particles do not contribute directly to the surface area exposed to the solution but lump together or bind onto larger particles, the solution to low permeability is the removal or binding together (by agglomeration) of the fine material.

Agglomeration with modified OPC provides a novel method for heap leaching of low-permeability ores in acid medium, which cannot otherwise be processed due to the high costs of conventional milling / flotation / concentration, and which cannot be heap-leached due to poor permeability. However, this method still requires further testing in the field in the absence of column wall support and where higher as-placed bulk densities may occur. Although the leach columns showed reduced slumping when binder was added, this was not necessarily the case in the hydrodynamic column tests.

The effect of compaction in the field could therefore negate the benefit provided by reduced slumping illustrated by the leach columns. For this reason it is important that the binder concept be demonstrated in the field in an actual pilot heap. Although a fairly wide column diameter (320 mm) was used in the 4 m tall column test, the presence of wall support cannot be discounted. However, the experimental programme followed a logical sequence from uni-axial compression tests, to short columns, to tall (4 m) columns, such that a field demonstration would be the next loxical step in the process. This will depend on finding a suitable industrial partner with a resource to demonstrate the technology.

Disadvantages of the binder include that no acid is introduced in agglomeration. For example, in oxide copper heap leach operations a large proportion of the acid is introduced during agglomeration to speed up the copper recovery. As demonstrated in the tall (4 m) leach column, it also takes a while for the drainage pH to be reduced to below pH 4, at which copper is soluble. Hence copper only started appearing in the drainage after 60 days. Although the calculation above indicates that the binder is economical, for large and remote operations the availability and transport of cement may become a problem. Hence this process may be more suitable at certain economies of scale (smaller operations).

6.5. Implications for heap leach design

One benefit of this work was to provide a summary and discussion of the design criteria for hydraulic testing of heap leach ores and agglomerates. The knowledge gained from the representation of the moisture balances in the leach columns (derived from the methodology applied in the hydrometallurgical columns), provide a better understanding of the hydrology of the leach columns. This type of representation is novel and has been uniquely adapted by the author in recent decades to better represent the hydrology of the leach columns. These include plotting the continuous moisture hold-up and degree of saturation profiles. The representation of the moisture content in the bed as a split between residual, mobile, “dead voids” and solids is also novel and has improved the understanding of the hydrology of the bed.

It is important to note that one of the reasons for the discrepancy in dissolution kinetics that is commonly observed during scale-up is the lower “as placed” bulk densities that are commonly employed in columns. This, together with column wall support and reduced homogeneity during scale-up leads to leach columns typically overestimating the permeability of both solution and air. Poor solution transport out of the packed bed was attributed to the presence of stagnant zones, which was proportional to the percentage fines and higher bulk density resulting from lack of column wall support. More uniformly sized and agglomerated material also had less stagnant zones (Bouffard and West-Sells, 2009). Hence

it is recommended that column leach tests should be performed at more realistic bulk densities as indicated by the compression test bulk density profile.

It was further identified that only the silt + clay fraction (-200 µm) plays an important role in inhibiting flow, rather than the entire fines fraction, which includes sand. Hence, desliming or agglomeration with binder needs only to focus on this fraction, rather than on reducing the overall fines content. Furthermore, even if desliming is performed on the head sample, additional fines may be generated due to the formation of precipitates such as jarosite, as well as decrepitation of the gangue matrix. This also emphasizes the need to incorporate hydrodynamic testing of leached residues as part of the test work programme. As a result, heap leach design often attempts to minimise the acid addition in order to reduce gangue reaction and associated precipitate formation. The hydrodynamic data should be interpreted in conjunction with the PSD of the head and residue.

Whereas lower crush sizes often enhance liberation of target minerals, this needs to be traded off against excessive fines (silt + clay) formation which inhibits permeability. This problem may be further exacerbated due to fines segregation during scale-up, which will result in a higher fines content in portions of the bed.

If the sample contains too little fines, on the other hand, this may result in poor radial dispersion of solution as well as increased channeling, which may be exacerbated by a wide dripper spacing. However, if only the silt + clay is removed, sufficient sand may remain behind to provide radial distribution of liquid. Hence it is important to differentiate between the sand and the silt + clay fraction, as the sand fraction does not necessary inhibit permeability. Furthermore, the presence of sand is beneficial, as it provides high surface area and accessibility of target minerals, as well as improving interconnectivity of pores (“reduced dead voids”), although the mechanism for this has not been clearly demonstrated.

It was furthermore highlighted that for ores with high silt + clay content, compression tests may overestimate agglomerate strength if the compression is performed with the sample containing only the agglomeration moisture. Hence the sample should be pre-wetted or the compression test should be performed under saturated conditions. This should be less of an issue with coarser samples with lower fines contents, as most of the load is exerted on coarser particles which compress against each another.

The test work results also show, counter-intuitively, that a coarser crush size is not necessarily beneficial for aeration, as this results in the formation of a larger proportion of poorly connected macro-pores which do not conduct solution or air once the more connected pores are filled up. This explains why the requirement for aeration requires a lower proportion of the bed voids (<65% rather than <100%) to be filled with solution, as a proportion of the voids are not connected and available for solution or air flow. Conventionally, the bed is divided into “mobile moisture” associated with macro-pores and “residual moisture” associated with micro-pores. The macro-pores partially fill with solution during percolation whereas the micro-pores hold solution even after draining.

Conventional wisdom suggests that coarser particles will provide more macro-pores and hence improve aeration. However, the results presented in this thesis suggest that, on average, only 65% of the

porosity is available for solution and air flow. This decreases to as low as 30% for ores with low fines content. It is therefore also necessary, not only to rely on the rule of thumb of 65% saturation, but to determine the percentage of the bed that is filled with “dead voids”. This may be done with hydrodynamic column tests, where the air entry point is measured.

6.6. Limitations of research

Whereas publications in heap leaching cover numerous aspects, such as modelling, hydrodynamics, novel techniques such as chloride-assisted leaching, leaching of refractory minerals such as chalcopyrite, and microbial assisted heap leaching at elevated temperature, the work here was limited to heap leach geomechanics (*i.e.* physical properties and hydrology). The results presented in this thesis are essentially limited to small-scale, 1 D column tests and compression tests. Furthermore, in most cases, the materials are agglomerated to produce fairly uniform, homogeneous samples. Hence the effects of fines segregation, non-homogeneity, and changes in hydrodynamics during scale-up was not addressed. The presence of column walls is also known to provide additional support and channel air in an upwards direction, whereas in practice, air may escape sideways in the heaps. For example, the binder concept was extended to a tall (4 m), 320 mm ID column to reduce the effect of wall support. In practice, leach columns of up to 1 m diameter have been used in Mintek’s laboratory, but in most cases, scale-up proceeds from tall (160 mm or 200 mm ID) columns directly to test heaps. For this reason, the binder concept needs to be further tested on a pilot heap scale.

6.7. Summary of findings

In summary, a number of important findings or benefits were derived from the test work:

- Single-phase or saturated flow can be modelled with packed bed theory, employing the concept of hydraulic radius.
- A better understanding of the effect of the distribution of void porosity on the ability of the ore to conduct air and solution was derived.
- It was shown that traditional soil models such as VGM are not applicable to heap leach materials, except for sandy ores. The VGM model needs to be modified to include an inflection point. This allows the data to be modelled by capillary flow and also allows the measured K_s to be used in the same model.
- A better understanding of the causes of low-permeability was derived, and a novel, potentially cost-effective process route for the treatment of low-permeabilty ores as high clay-containing African ores was developed, where traditional processing routes are uneconomical or technically unsound. It may also be extended to improve aeration, for example, in ores with medium clay content, and requires demonstration in the field.

7. REFERENCES

Afewu, K.I. (2009). *'Development and testing of a 2D axisymmetric water flow and solute transport model for heap leaching'*, PhD thesis, The University of British Columbia.

AME (2018). *'Copper – declining copper ore grades'*, https://www.amegroup.com [accessed 5 September 2023].

Arpalahti, A. and Lundström, M. (2019). *'Dual aeration tests with heap leaching of pyrrhotite-rich pentlandite ore'*, Hydrometallurgy 185, 173-185.

Assouline, S. and Or, D. (2013). *'Conceptual and parametric representation of soil hydraulic properties: A Review',* doi:10.2136/vzj2013.07.0121, www.VadoseZoneJournal.org.

Afrisam (2021). https://www.afrisam.co.za/product/cement/slagment/ [accessed 25 April 2023].

Arrellano, A.D.B., Yao, T., Milczarek, M. and Busseau, M. (2022). *'Column experiments to assess consolidation behaviour at different initial irrigation rates in copper heap leaching'*, Proceedings of Heap Leach Solutions 2022, Sparks, USA.

Bartlett, R.W. (1998). Solution Mining: Leaching and Fluid Recovery of Materials. Gordon and Breach Science Publishers.

BASF global mining solutions. https://energy-resources.basf.com/global/en/mining_solutions/BASF_Hydrometallurgy/CopperApplications/Leaching.html [accessed on 26 March 2024].

Basov, V. (2015). Heap Leach: Mining's breakthrough technology, https://www.mining.com/ heap-leach-minings-breakthrough-technology [accessed on 9 June 2020].

Bennet, C.R., McBride, D., Cross, M. Gebhardt, J.E. (2002), *'A comprehensive model for copper sulphide heap leaching'*. Hydrometallurgy 127-128, 150-161.

Bouffard, S.C. (2008). *'Agglomeration for heap leaching: Equipment design, agglomerate quality control, and impact on the heap leach process'*, Minerals Engineering, 21, 1115-1125.

Bouffard, S.C. and Dixon, D. (2001). '*Investigative Study into the Hydrodynamics of Heap Leaching Processes'*, Metallurgical and Materials Transactions B, 32B, 763-776.

Bouffard, S.C. and West-Sells, P.G. (2009). *'Hydrodynamic properties of heap leach piles: Influence of testing scale and material properties'*, Hydrometallurgy 98, 136-142.

Burdine, N.T. (1953). '*Relative permeability calculations from pore-size distribution data*', Petr. Trans., Am. Inst. Mining Metall. Eng. 198: 71-77.

Brooks, R.H. and Corey, A.T. (1964). *'Hydraulic properties of porous media'*, Hydrology Papers No. 3, Colorado State University, Fort Collins, Colorado.

Cariaga, E., Martinez, R., Sepulveda, M. (2015). *'Estimation of hydraulic parameters under unsaturated flow conditions in heap leaching'*, Math. Comput. Simul. 109C, 20-31.

Carman, P.C. (1937). Trans. Inst. Chem. Engrs. (London), 15, 150.

Cherkaev, A. (2019*). 'The art of soaking rocks: systematic study of liquid and solute flow in packed rock beds in the context of heap leaching'*, PhD thesis, University of Cape Town, 100-110.

Chen, K., Yin, W., Rao, F., Wu, J., Zhu, Z. and Tang, Y. (2020). '*Agglomeration of Fine-Sized Copper Ore in Heap Leaching through Geopolymerization Process',* Minerals Engineering, 159, 106649, 1-8.

Clennel, M.B. (1997). *'Tortuosity: a guide through the maze'*, in: Lovell, M.A. and Harvey, P.K. (Eds.), Developments in Petrophysics, Geological Society Special Publication No. 122, 299-344.

Deep South Resources, (2020), Preliminary economic assessment, Completed December 2020 by Mineral Engineering and Technical Services (METS), Australia, https://www.deepsouthresources.com [accessed 5 September 2023]

De Andrade Lima, L.P.R. (2006). *'Liquid axial dispersion and holdup in column leaching'*. Miner. Eng. 19, 37-47.

Dew, D.W., Rautenbach, G.F., van Hille, R.P., Davis-Belmar, C.S., Harvey, I.J. and Truelove, J.S. (2011). *'High temperature heap leaching of chalcopyrite: Method of evaluation and process model'*, Percolation leaching: The status globally and in Southern Africa, The Southern African Institute of Mining and Metallurgy.

Dixon, D.G. and Petersen, J. (2003). *'Comprehensive Modelling Study of Chalcocite Column and heap Bioleaching*.' Copper 2003, Volume VI-Hydrometallurgy of Copper (Book 2), Santiago. pp.493-516.

Dhawan, N., Safarzadeh, M.S., Miller, J.D., Moats, M.S. and Rajamani, R.K. (2013). '*Crushed ore agglomeration and its control for heap leach operations'*, Minerals Engineering, 41, 53-70.

Dullien, F.A.L. (1977). Porous Media: Fluid Transport and Pore Structure. Second Edition. Academic Press, San Diego.

Espinoza-Andaluz, M., Andersson, M. and Sundén, B. (2017). '*Computational time and domain size analysis of porous media flows using the lattice Boltzmann method',* Computers and Mathematics with Applications. 74: 26-34.

Garcia, A. and Jorgensen, M. (1997). '*Agglomeration and Heap Leach Testing Requirements for High Clay Ores*', Randol Gold Forum, 143-146.

Galdos, H., Guevara, J. and Saavedra, A. (2013). *'Geotechnical Lessons Learned from the Operation of Cerro Verde's Crush Leach Pad 4-A'*, 5th International Seminar on Process Hydrometallurgy, Santiago, Chile.

Gerke, H.H. and van Genuchten, M.T. (1993). *'A Dual-Porosity Model for Simulating the Preferential Movement of Water and Solutes in Structured Porous Media'*, Water Resources Research, Vol. 29, 305-319.

Ghasemi, Y. and Cwirzen, A. (2017). *'Estimation of specific area of particles based on size distribution curve'*, Magazine of Concrete Research, Paper 1700045

Ghorbani, Y., Franzidis, J.P., Petersen, J. (2015). '*Heap leaching technology – current state, innovations and future directions: A review',* Mineral Processing and Extractive Metallurgy Review, 37, Issue 2, 73-119.

Goguen, G. (2020). '*A closer look: fly ash, slag cement and metakaolin'*, National Precast Concrete Association, Precast Magazines, https://precast.org/2020/01/a-closer-look-fly-ash-slag-cement-metakaolin/#:~:text=Slag%20is%20not%20a%20pozzolan,alkalis%20in%20its%20hydration%20products.&text=Slag%20cement%20is%20generally%20ground,range%20of%202.85%20to%202.95. [accessed 25 April 2023].

Grieve, G. (2009*). 'Cementitious materials'*. *In*: Owens, G (Ed.), Fulton's Concrete Technology. Cement & Concrete Institute, South Africa. Pp. 1 – 16.

Guzman, A., Scheffel, R. and Flaherty, S. (2008). '*The Fundamentals of Physical Characterisation of Ore for Heap Leach*', Sixth International Symposium on Hydrometallurgy, Y.A. Courtney *et al*., eds., Phoenix, AZ, Society for Mining, Metallurgy and Exploration Inc., Englewood, CO.

Glover, P.W.J. (2023). Petrophysics MSc course notes, https://homepages.see.leeds.ac.uk/~earpwjg/PG_EN/CD%20Contents/GGL-66565%20Petrophysics%20English/Chapter%202.PDF, [accessed 3 December 2023]

Guzman, A. (2012), *'Tschudi Characterisation'* – Technical review report.

Guzman, A., Robertson, S.W. and Calienes, B. (2013). *'Constitutive relationships for the representation of a heap leach process'*, International Heap Leach Conference, Vancouver, Canada.

Ilankoon, I.M.S. (2012). 'Hydrodynamics of Unsaturated Particle Beds Pertaining to Heap Leaching', PhD Thesis, Imperial College, London.

Ilankoon, I.M.S. and Neethling, S.J. (2012). 'Hysteresis in unsaturated flow in packed beds and heaps', Minerals Engineering, 35, 1-8.

Ilankoon, I.M.S. and Neethling, S.J. (2013). *'The effect of particle porosity on liquid holdup in heap leaching',* Minerals Engineering, 45, 73-80.

Ilankoon, I.M.S., Neethling, S.J., Huang, Z. and Cheng, Z. (2017). '*Improved inter-particle flow models for heap leaching hydrodynamics*', Minerals Engineering, 111, 108-115.

John, L.W. (2011). *'Financial risk reduction via hybrid heap leaching'*, Percolation leaching: The status globally and in Southern Africa, The Southern African Institute of Mining and Metallurgy, Mulsdersdrift, Gauteng, South Africa.

Kappes, D.W. (2002) *'Precious metal heap leach design and practice'*, Mineral Processing Plant Design, Practice, and Control', Volume 1, 1606-1630.

Kawatra, S.K., Eisele, T.C., Lewandowski, K.A. and Gurtler, J.A. (2006). *'Novel binders and methods for agglomeration of ore.'* Semiannual Technical Progress Report, Michigan Technological University.

Keller, J., Yao, T., Miczarek, M., Lofftus, V. and Myrhow, S. (2022). *'Ore permeability and blending evaluation to optimise leach performance'*, Proceedings of Heap Leach Solutions 2022, Sparks, USA.

Kodali, P., Depci, T., Dhawan, N., Wang, X.M., Lin, C.L. and Miller, J.D. (2011). '*Evaluation of stucco binder for agglomeration in the heap leaching of copper ore',* Minerals Engineering, 24 (8), 886-893.

Kosugi, K., Hopmans, J.W. and Dane, J.H. (2002). *'Parametric models'*, Methods of soil analysis. Part 4: Physical methods, SSSA Book Series No. 5, Soil Science Society of America, Madison, WI.

Kruger, T. (2017). *'Tiger Resources' cash flow comes under pressure due to difficulties at Kipoi copper project'*, Mining Review Africa, Tiger Resources' cash flow comes under pressure due to difficulties at Kipoi copper project (miningreview.com) [accessed 5 September 2023].

Lea, F.M. (1956*). 'The Chemistry of Cement and Concrete'*, 2nd Edition. Butler & Tanner Ltd., Frome and London.

Lewandowski, K.A. and Kawatara, S.K. (2009). *'Binders for heap leaching agglomeration'*, Minerals and Metallurgical Processing, 26 (1), 1-24.

Lizama, H.M. (2009). *'Oxygen liquid-film mass transfer in heap leaching'*, Hydrometallurgy, Vol. 100, 29-34.

Logan, T.C., Seal, T. and Brierley, J.A. (2007). *'Whole-Ore Heap Biooxidation Sulfidic Gold-Bearing Ores, In: Rawlings'*, D.E. and Johnson, D.B. (Eds). Biomining. 1st Edition, Springer, Berlin, 113-138.

Lopez, M.J. (2021). Private Communication.

Lothenbach, B., Scrivener, K. and Hooton, R.D. (2011*). 'Supplementary cementitious materials, Cement and Concrete Research'*, 41:1244-1256.

Luckner, L., van Genucten, M. T. and Nielsen, D.R. (1989). *'A consistent set of parametric models for the two-phase flow of immiscible fluids in the subsurface'*, Water Resourc Res. 25: 2187-2193.

Lupo, J.F. (2011). '*Sustainability issues related to heap leaching operations*', Percolation leaching: The status globally and in Southern Africa, The Southern African Institute of Mining and Metallurgy, Misty Hills, Muldersdrift, South Africa.

Menacho, J. and Cifuentes, (2013). *'Heap Leaching Aeration: Science or Art?'*, Hydroprocess 2013, Sheraton Hotel, Santiago, Chile.

Manchisi, J., Mhandu, T.J., Kane, J., Ndlovu, S. (2019). *'A hybrid process to enhance the dissolution of cupriferous micas in the Chingloa refractory ore'*, Hydrometallurgy, 186, 151-161.

Marsden, J. and Botz, M.M. (2017). *'Heap leach modelling: A review of approaches to metal production forecasting'*, Minerals and Mineral Processing, 34 (2), 53-64.

McBride, D., Cross, M., Croft, T.N., Bennet, C. and Gebhardt, J.E. (2006). *'Computational modelling of variably saturated flow in porous media with complex three-dimensional geometries'*, Numerical Methods in Fluids, 50, 1085-1117.

McBride, D., Gebhardt, J.E., Croft, T.N. and Cross, M. (2015). '*Modelling the hydrodynamics of heap leaching in sub-zero temperatures*', Minerals Engineering, Vol. 90, 77-88.

McDonald, M.J., Chu, C., Guilloit, P.P. and Ng, K.M. (1991). '*Generalised Blake-Kozeny Equation for Multisized Spherical Particles*', AIChE Journal, Vol. 37, No. 10.

Mclelland, G.E. (1986). *'Heap Leaching and Agglomeration: Heap Leaching Practice in the United States'*, Gold 100, Proceedings of the International Conference on Gold, Volume 2, Extractive Metallurgy of Gold, SAIMM, Johannesburg.

Miao, X., Narsilio, G.A., Wu, A. and Yang, B. (2017). '*A 3D dual pore-system leaching model. Part 1: Study on fluid flow*', Hydrometallurgy, Vol. 167, 173-182.

Milczarek, M., Banerjee, M., Yao, T., Keller, J. and Shrestha, P. (2012). *'Ore permeability methods of evaluation and application to heap leach optimisation'*, Geomet 2012: International Seminar on Geometallurgy, Santiago, Chile.

Milczarek, M., Yao, T., Banerjee, M. and Keller, J. (2013). '*Ore permeability methods of evaluation and application to heap leach optimisation*', Heap Leach Solutions, Vancouver, Canada.

Miller, G.M. (2003). *'Analysis of commercial heap leach data*'. Copper 2004, Volume VI-Hydrometallurgy of Copper (Book 2), Santiago, Chile, pp. 531-545

Mohanty, M.P., Bowman, R.S., Hendrickx, J.M.H. and van Genuchten, M.T. (1997). *'New piecewise-continuous hydraulic functions for modelling preferential flow in an intermittent-flood-irrigation field'*, Water Resources Research, Vol. 33, No. 9, 2049-2063.

Moxicoresources (2020). 'Mimbula copper project', https://moxicoresources.com/projects-3-1/2020/6/30/mimbula, [accessed 9 September 2023].

Mualem, Y. (1976*). 'A new model for predicting the hydraulic conductivity of unsaturated porous media'*, Water Resources Research, Vol. 12, No. 3, 513-522.

Muhammad, S. and Nadeem, S. (2022). '*Viscometric study of ionic interactions of $MgSO_4$ in water and water-ethanol mixtures at different temperatures'*, Russian Journal of Physical Chemistry A, 2022, Vol. 96, 849-859.

Neira, A., Pizarro, D., Quezada, V. and Velasquez-Yevenes. (2021). *'Pretreatment of copper sulphide ores prior to heap leaching: A review'*, Metals, 11, 1067.

Newman, L.L., Herasymuik, G.M., Barbour, S.L., Fredlund, D.G. and Smith, T. (1997). '*The Hydrology of Waste Rock Dumps and a Mechanism for Unsaturated Preferential Flow*', Fourth International Conference on Acid Rock Drainage, Vancouver, B.C., Canada, Proceedings, Vol. II, 551-565.

O'Kane Consultants Inc. (2000). *'Demonstration of the application of unsaturated zone hydrology for heap leach optimisation'*, https://www.ore-max.com/pdfs/resources/unsaturated-zone-hydrology-for-heap-leach-optimization.pdf, [accessed on 20 September 2022].

Parker, J.C., Lenhard, R.J. and Kuppusamy, T. (1987). *'A parametric model for constitutive properties governing multiphase flow in porous media'*, Water Resources Research, Vol. 23, No. 4, 618-627.

Perry, R.H., Green, D.W., Maloney, J.O. (1999). *'Perry's chemical engineers' handbook'*, 7th edition, Mc-Graw-Hill.

Petersen, J. (2016). *'Heap leaching as a key technology for recovery of values from low-grade ore – A brief overview'*, Hydrometallurgy, 165, 206-212.

Pyper, R., Kappes, D.W. and Albert, T. (2015). *'Evaluation of agglomerates using the Kappes Percolation Test'*, Heap Leach Solutions, Reno Nevada, 319-325.

Ramírez, L., Font, J. and Saldaña, M. (2019). '*Chuquicamata Improvements for Low Permeability Heap Leaching Dump*', 11th International Seminar on Process Hydrometallurgy, Santiago, Chile.

Rautenbach, G.F. (2015). *'Heap leaching of copper'*, *WO2015059551 A1*.

Reyes, O., Moreno, L., Parada, F. and Sancez, M. (2007). *'Modelling of bacterial leaching in heap with forced aeration'*, IFAC Proceedings, Volume 40, Issue 11, 81-86.

Robertson, S.W., van Staden, P.J., Vercuil, A., Glover, G. and Shaidaee, B. (2007). *'Heap bioleaching of low-grade chalcopyrite ore from the Darehzare deposit'*, ALTA 2007, Perth.

Robertson, S.W., Guzman, A. and Miller, G. (2013). '*Implications of hydraulic behaviour testing for heap leach modelling*', Hydroprocess: 5th International Seminar on Process Hydrometallurgy, Santiago, Chile.

Robertson, S.W. (2017). *'Development of an integrated heap leach solution flow and mineral leaching model'*, Hydrometallurgy 169, 79-88.

Robertson, S.W., Basson, P., Mxinwa, S. and Ndhlalose, M.S. (2020), *'Advances in Heap Leaching of Refractory and Low-Permeability Ores'*, Hydroprocess 2020: 12th International Conference on Process Hydrometallurgy, Santiago, Chile.

Robertson, S.W., Mxinwa, S., Basson, P., Ndhlalose, M.S., Nxumalo, D.N. (2022a). *'Binder for an agglomeration process'*, WO 2022/05560 A1.

Robertson, S.W., van Staden, P.J., Cherkaev, A. and Petersen, J. (2022b). *'Properties governing the flow of solution through crushed ore for heap leaching'*, Hydrometallurgy, 208, 105811.

Robertson, S.W., Mxinwa, S., Basson, P., Ndhlalose, M.S., Nxumalo, D.N. (2023a). *'Binder for an agglomeration process'*, Namibian Patent: NA/P/2023/0001.

Robertson, S.W., Basson, P., van Staden, P.J. and Petersen, J. (2023b*). 'Properties governing the flow of solution and air through crushed ore for heap leaching: Part II: Unsaturated dual-phase flow'*, Hydrometallurgy, 215, 105990.

Russo, D. (1988). 'Determining soil hydraulic properties by parameter esimtation: On the selection of a model for hydraulic properties', Water Resources Research, 24, 453-459.

Saleh, H.M. and Eskander, S.B. (2020). *'Innovative cement-based materials for environmental protection and restoration'*. In: Samui, P., Iyer, N.R., Kim, D. and Chaudhary, S. (Eds.), New Materials in Civil Engineering. Elsevier, 613 – 641.

Saez, A.E. and Carbonell, R.G. (1985*).'Hydrodynamic paramters for gas-liquid cocurrent flow in packed beds'*, AICHE Journal, Vol. 31, No. 1, 52-62.

Scheffel, R.E., Guzman, A. and Dreier, J.E. (2016). *'Development of metallurgy guidelines for copper heap leach'*, Minerals and Metallurgical Processing, Vol. 33, No. 4, 187-199.

Scheffel, R. (2017). Private communication.

Simunek, J., van Genuchten, M., (2008). *'Modelling non-equilibrium flow and transport processes using HYDRUS'*. Vadose Zone Journal 7, 782-797.

Snellings, R., Mertens, G. and Elsen, J. (2012). *'Supplementary cementitious materials'*. *In*: Broekmans, M.A.T.M. and Pöllmann, H. (Eds.), Applied Mineralogy of Cement and Concrete, *Reviews in Mineralogy and Geochemistry*, Volume 74. Mineralogical Society of America Geochemical Society, USA, 211 – 278.

Taylor, H.F.W. (1997*). 'Cement Chemistry'*, 2nd Edition. Thomas Telford Publishing, London.

Terzaghi, K., Peck, R.B. and Mesri, G. (1996). *'Soil Mechanics in Engineering Practice'*, Third edition, John Wiley & Sons, Inc., New York.

Toro, N., Ghorbani, Y., Turan, M.D., Robles, P. and Galvez, E. (2021). *'Gangue and clays minerals as rate-limiting factors in copper heap leaching: A review'*, Metals, 11, 1539.

Tzimopoulos, C.D. and Sakellariou-Makrantonaki, M. (1996). *'A new analytical model to predict the hydraulic conductivity of unsaturated soils'*, Water Resources Mangagement 10: 397-414.

Van Genuchten, M. T. (1980*). 'A closed-form equation for predicting the hydraulic conductivity of unsaturated soils*', Soil Science Society of America, Vol. 44, No. 5.

Van Staden, P.J. (2017). *'Comparative assessment of heap leach production data – 2. Heap leaching kinetics of Kipoi HMS floats material, laboratory vs. commercial scale'*, Minerals Engineering 101, 58-70.

Van Staden, P.J. and Petersen, J. (2018). *'The effects of simulated stacking phenomena on the percolation leaching of crushed ore, Part 1: Segregation'*, Minerals Engineering 128, 202-214.

Van Staden, P.J. (2019). *'Effect of scale of operation on heap leaching performance'*, PhD thesis, University of Cape Town.

Wang, L., Yin, S. and Wu, A. (2021). *'Ore agglomeration behaviour and its key controlling factors in heap leaching of low-grade copper minerals'*, Journal of Cleaner Production, 279, 123705.

Warren, B. (2021). *'Dealing with lumps and clumps in solids'*, De Dietrich Process Systems, https://ddpsinc.com/blog/dealing-with-lumps-and-clumps-in-solids, [accessed 3 December 2023]

Whiterow, P. (2013). '*Update – Frontier Mining says Benkala now generating cash for the first time in its history'*, https://www.proactiveinvestors.com.au/companies/news/54061/update-frontier-mining-says-benkala-now-generating-cash-for-first-time-in-its-history-64083.html [accessed on 9 June 2020].

Zender, C. (2017). '*Particle size distributions: Theory and Application to Aerosols, Clouds and Soils'*, University of California, http://dust.ess.uci.edu/facts/psd/psd.pdf, [accessed on 23 November 2020].

Zhao, M., Liu, G., Deng, L. and Li, Y. (2021*). 'Optimizing the compaction characteristics and strength properties of gravelly soils in terms of fine contents'*, Advances in Materials Science and Engineering, Vol. 2021, Article ID 6634327, https://doi.org/10/1155/2021/6634237.

APPENDIX A

Table A.1. List of samples used in compression and hydrodynamic column tests (Part I)

Sample description	Code	Topsize, mm	Silt + clay % -75µm	Columns		Compression tests		Polynomial		Power	
				Residual Moisture, m^3/m^3	Residual Porosity, m^3/m^3	Residual Moisture, m^3/m^3	Residual Porosity, m^3/m^3	A x 100	B x 100	a x 100	ʌ
Chilean copper porphory quartz sericite head	QS1H	12.5	1.6	0.12	0.46	-	-	0.551	0.55	5.9	0.73
Chilean copper porphyry quartz sericite head	QS2H	12.5	1.6	0.13	0.39	-	-	0.551	0.50	5.9	0.73
Chilean copper porphyry quartz sericite residue	QS1R	12.5	11.0	0.10	0.51	-	-	0.233	3.50	22.1	0.36
Chilean copper porphyry quartz sericite residue	QS2R	12.5	12.0	0.15	0.39	-	-	0.233	3.50	22.1	0.36
Chilean copper porphyry (BC) head	BC1H	12.5	6.0	0.12	0.50	-	-	-0.088	8.10	21.7	0.54
Chilean copper porphyry (BC) head	BC2H	12.5	6.0	0.12	0.43	-	-	-0.088	8.10	21.7	0.54
Chilean copper porphyry (BC) residue	BC1R	12.5	29.0	0.15	0.44	-	-	0.051	4.72	42.1	0.20
Chilean copper porphyry (BC) residue	BC2R	12.5	29.0	0.19	0.42	-	-	0.051	4.72	42.1	0.20
Chilean copper porphyry (BC) residue	BC3R	12.5	29.0	0.20	0.38	-	-	0.051	4.72	42.1	0.20
Chilean copper / gold porphyry oxide argillic residue	OA1R	20	13.0	0.14	0.41	-	-	-	-	34.4	0.36
Chilean copper / gold porphyry oxide argillic residue	OA2R	25	16.6	0.10	0.47	-	-	-	-	29.7	0.36
Chilean copper / gold porphyry supergene quartz sericite residue	SQS1R	20	17.4	0.16	0.43	-	-	-	-	34.4	0.32
Chilean copper / gold porphyry supergene quartz sericite residue	SQS2R	25	10.1	0.16	0.43	-	-	-	-	34.0	0.30
Chilean copper / gold porphyry mixed oxide supergene argilic quartz sericite residue	OSAQSR	25	17.2	0.16	0.45	-	-	-	-	30.8	0.34
Chilean copper / gold porphyry mixed supergene quartz sericite P residue	SQSP1R	25	11.1	0.13	0.44	-	-	-	-	34.4	0.36
Chilean copper / gold porphyry mixed supergene quartz sericite P residue	SQSP2R	20	12.5	0.18	0.44	-	-	-	-	35.5	0.32
Chilean copper / gold porphyry supergene phyllic alteration residue	SPAR	20	11.2	0.13	0.43	-	-	-	-	27.1	0.42
Congolese sedimentary stratified hosted copper oxide (C1) head	KC1H	25	4.8	0.13	0.40	0.26	0.47	0.029	2.94	13.9	0.46
Congolese sedimentary dolomite hosted copper oxide (C1) deslimed head	KC1HD	25	0.0	-	-	0.17	0.43	-0.009	4.02	6.0	0.94
Congolese sedimentary dolomite hosted copper oxide (C1) deslimed residue	KC1RD	25	5.0	0.12	0.48	0.14	0.48	0.042	2.70	13.2	0.45
Congolese sedimentary dolomite hosted copper oxide (C2) head	KC2H	25	3.9	0.11	0.41	0.16	0.45	0.024	3.05	12.2	0.50
Congolese sedimentary dolomite hosted copper oxide (C2) deslimed head	KC2HD	25	0.0	-	-	0.11	0.50	0.027	3.20	6.0	0.94
Congolese sedimentary dolomite hosted copper oxide (C2) deslimed residue	KC2RS	25	2.5	0.07	0.46	0.07	0.49	0.072	2.00	8.4	0.56
Congolese sedimentary dolomite hosted copper oxide (C3) head	KC1H	25	3.9	0.13	0.40	0.31	0.45	-0.029	4.45	13.0	0.52
Congolese sedimentary dolomite hosted copper oxide (C3) deslimed head	KC3HD	25	0.9	-	-	0.18	0.46	-0.008	3.94	6.0	0.94
Congolese sedimentary dolomite hosted copper oxide (C3) deslimed residue	KC3RD	25	10.3	0.13	0.40	0.16	0.39	-0.038	4.33	23.9	0.36
Congolese sedimentary dolomite hosted copper oxide (CC) head	KCCHU	25	2.5	-	-	0.19	0.43	-0.035	4.61	6.0	0.94
Congolese sedimentary dolomite hosted copper oxide (CC) deslimed head	KCCHD	25	4.2	-	-	0.14	0.44	-0.050	4.95	6.0	0.94
Congolese sedimentary dolomite hosted copper oxide (CC) residue	KCCR	25	3.1	-	-	0.17	0.42	0.000	0.00	13.6	0.61
Congolese sedimentary dolomite hosted copper oxide (CC) deslimed residue	KCCRD	25	3.1	0.13	0.47	-	-	0.000	0.00	13.6	0.61
Congolese sedimentary stratified hosted copper oxide (N1) head	KN1H	25	6.2	0.11	0.45	0.30	0.48	0.085	1.23	15.5	0.36
Congolese sedimentary stratified hosted copper oxide (N1) deslimed head	KN1HD	25	0.0	-	-	0.11	0.49	0.058	2.23	96.4	2.21
Congolese sedimentary stratified hosted copper oxide (N1) residue	KN1R	25	9.6	-	-	0.25	0.41	0.085	1.23	15.5	0.36
Congolese sedimentary stratified hosted copper oxide (N1) deslimed residue	KN1RD	25	2.3	-	-	0.15	0.45	0.058	2.23	96.4	2.21
Congolese sedimentary stratified hosted copper oxide (N2&4) deslimed head	KN24HD	25	0.0	-	-	0.33	0.46	-0.083	5.46	4827	3.87
Congolese sedimentary stratified hosted copper oxide (N2&4) deslimed residue	KN24RD	25	3.7	-	-	0.27	0.49	-0.083	5.46	4827	3.87
Congolese sedimentary stratified hosted copper oxide (N2&4) residue	KN24R	25	18.5	-	-	0.42	0.42	-0.028	3.42	32.1	0.30
Congolese sedimentary dolomite hosted heavy media separation floats (C1) head	KHMS1H	25	7.4	0.15	0.38	0.31	0.39	-	-	25.3	0.44
Congolese sedimentary dolomite hosted heavy media separation floats (C2) head	KHMS2H	25	7.4	0.15	0.37	-	-	-	-	25.3	0.44
Congolese sedimentary dolomite hosted heavy media separation floats (C5) residue	KHMS5R	25	18.0	0.15	0.36	0.36	0.36	-	-	38.0	0.32
Congolese sedimentary dolomite hosted heavy media separation floats (C6) residue	KHMS6R	25	13.5	0.18	0.37	0.23	0.38	-	-	34.9	0.37

Table A.1 (continued) List of samples used in compression and hydrodynamic column tests (Part I)

Sample description	Code	Topsize, mm	Silt + clay % -75µm	Columns		Compression tests		Polynomial		Power	
				Residual Moisture, m^3/m^3	Residual Porosity, m^3/m^3	Residual Moisture, m^3/m^3	Residual Porosity, m^3/m^3	A x 100	B x 100	a x 100	ʌ
Congolese sedimentary dolomite hosted copper oxide (KL1) head	KL1H	25	10.5	-	-	0.31	0.43	-	-	25.4	0.36
Congolese sedimentary dolomite hosted copper oxide (KL1) deslimed head	KL1HD	25	0.0	-	-	0.21	0.45	-0.050	4.90	10.6	0.72
Congolese sedimentary dolomite hosted copper oxide (KL1) deslimed residue	KL1RD	25	3.2	-	-	0.22	0.35	-0.065	5.15	8.3	0.37
Congolese sedimenatry dolomite hosted copper oxide (KL2) deslimed head	KL2HD	25	0.0	-	-	0.22	0.46	-0.021	4.18	10.3	0.71
Congolese sedimentary dolomite hosted copper oxide (KL2) residue	KL2R	25	17.1	-	-	0.43	0.37	-0.044	3.84	141	0.87
Congolese sedimentary dolomite hosted copper oxide (KL2) deslimed residue	KL2RD	25	2.5	-	-	0.23	0.42	-0.020	4.17	6.1	0.35
Spanish vein-type uranium ore (A1) head	A1H	30	6.0	-	-	0.16	0.40	-0.047	4.45	13.8	0.31
Spanish vein-type uranium ore (A1) head	A11H	50	6.5	-	-	0.14	0.43	0.0001	1.85	10.0	0.16
Spanish vein-type uranium ore (A1C13) residue	A1C13R	30	10.0	-	-	0.13	0.46	-0.048	4.57	16.9	0.20
Spanish vein-type uranium ore (A1C12) residue	A1C12R	25	14.5	-	-	0.27	0.36	-0.192	8.27	23	0.19
Spanish vein type uranium ore (A2) head	A2H	50	1.0	-	-	0.05	0.50	0.012	1.44	2.9	0.38
Spanish vein-type uranium ore (A2) head	A22H	30	3.0	-	-	0.11	0.44	-0.010	3.57	8.4	0.39
Spanish vein-type uranium ore (A2C19) residue	A2C19R	30	10.6	-	-	0.21	0.42	-0.020	13.9	17.5	0.20
Spanish vein-type uranium ore (A2C18) residue	A2C18R	25	6.0	-	-	0.16	0.44	-0.161	8.08	12.2	0.28
Spanish vein-type uranium ore (A3) head	A3H	50	4.8	-	-	0.08	0.53	0.010	1.66	7.6	0.18
Spanish vein-type uranium ore (A3) head	A33H	25	10.5	-	-	0.10	0.44	-0.163	7.87	17.6	0.20
Spanish vein-type uranium ore (A3) head	A333H	30	2.0	-	-	0.07	0.48	-0.007	3.49	7.3	0.46
Spanish vein-type uranium ore (A3C27) residue	A3C27R	25	11.0	-	-	0.25	-	-0.154	7.58	20.4	0.23
Spanish vein-type uranium ore (A3C24) residue	A3C24R	25	11.0	-	-	0.23	0.43	-0.148	7.38	19.6	0.23
Spanish vein-type uranium ore (A1C16) residue	A1C16R	40	12.0	-	-	0.21	-	-0.063	4.81	17.9	0.17
Spanish vein-type uranium ore (A2C20) residue	A2C20R	50	1.7	-	-	0.07	-	0.015	1.38	3.8	0.32
Spanish vein-type uranium ore (A2C21) residue	A2C21R	25	6.0	-	-	0.16	-	-0.152	7.96	12	0.27
Spanish vein-type uranium ore (A2C22) residue	A2C22R	30	10.0	-	-	0.22	-	-0.026	3.79	17	0.20
Spanish vein-type uranium ore (A2C23) residue	A2C23R	50	1.7	-	-	0.08	-	-0.033	4.04	3.35	0.28
Spanish vein-type uranium ore (A3C25) residue	A3C25R	30	3.0	-	-	0.14	0.47	-0.010	3.65	8.1	0.35
Spanish vein-type uranium ore (A3C26) residue	A3C26R	50	12.0	-	-	0.09	-	-0.005	2.05	16.3	0.13
Spanish vein-type uranium ore (A3C28) residue	A3C28R	30	3.0	-	-	0.12	-	-0.018	3.88	7.58	0.34
Spanish vein-type uranium ore (A3C29) residue	A3C29R	50	7.7	-	-	0.19	-	-0.001	1.86	12.3	0.19
Spanish vein-type uranium ore (RC2) head	RC2H	50	7.0	-	-	0.15	0.45	0.013	1.00	13.1	0.25
Spanish vein-type uranium ore (R1C1) residue	RP1C1R	50	35.0	-	-	0.40	0.33	-0.018	1.70	51.9	0.15
Spanish vein-type uranium ore (R1C2) residue	RP1C2R	50	37.0	-	-	0.47	0.38	-0.012	1.34	54.0	0.15
Spanish vein-type uranium ore (R1C4) residue	RP1C4R	50	27.0	-	-	0.68	-	-0.014	1.74	37.6	0.13
Spanish vein-type uranium ore (R2C6) residue	RP2C6R	40	15.0	0.09	0.39	0.29	0.33	-	-	29.8	0.31
Spanish vein-type uranium ore (R2C7) residue	RP2C7R	40	11.0	0.14	0.36	-	-	-	-	24.8	0.36
Spanish vein-type uranium ore (R3C9) residue	RP3C9R	40	17.0	0.16	0.40	-	-	-	-	30.6	0.28
Spanish vein-type uranium ore (R3C10) residue	RP3C10R	40	20.0	0.15	0.35	-	-	-	-	34.4	0.24
Spanish vein-type uranium ore (ZA) head	ZAH	50	8.5	-	-	0.10	-	0.013	1.17	11.7	0.12
Spanish vein-type uranium ore (ZA1) residue	ZA1R	50	28.0	-	-	0.29	0.39	-0.009	1.60	35.9	0.09
Spanish vein-type uranium ore (ZA2) residue	ZA2R	25	31.0	-	-	0.25	0.40	-0.134	6.08	40.3	0.10
Spanish vein-type uranium ore (ZC) head	ZCH	50	3.0	-	-	0.09	-	0.007	1.52	6.64	0.32
Spanish vein-type uranium ore (ZC1) residue	ZC1R	50	16.7	-	-	0.21	0.41	-0.032	2.87	24.9	0.15
Spanish vein-type uranium ore (ZC2) residue	ZC2R	25	16.0	-	-	0.25	0.42	-0.206	8.39	27.6	0.20
Spanish vein-type uranium ore (ZD) head	ZDH1	50	4.8	-	-	0.08	-	0.006	1.58	7.89	0.20
Spanish vein-type uranium ore (ZD) head	ZDH2	25	12.0	-	-	0.12	-	-0.153	7.63	20.4	0.21
Spanish vein-type uranium ore (ZD1) residue	ZD1R	50	18.0	-	-	0.22	0.39	-0.022	2.51	22.7	0.10
Spanish vein-type uranium ore (ZD2) residue	ZD2R	25	20.0	-	-	0.33	0.41	-0.170	7.61	25.8	0.10

Table A.1 (continued) List of samples used in compression and hydrodynamic column tests (Part I)

Sample description	Code	Topsize, mm	Silt + clay % -75µm	Columns		Compression tests		Polynomial		Power	
				Residual Moisture, m^3/m^3	Residual Porosity, m^3/m^3	Residual Moisture, m^3/m^3	Residual Porosity, m^3/m^3	A x 100	B x 100	a x 100	ʌ
Namibian sedimentary sandstone hosted copper lower oxide head	T2LOXH	25	15.0	-	-	0.32	0.49	0.084	-0.02	39.5	0.35
Namibian sedimentary sandstone hosted copper lower oxide head	T2LOX2H	25	15.0	-	-	0.34	0.46	0.084	-0.02	39.5	0.35
Namibian sedimentary sandstone hosted copper oxide cores head	T2OCH	12	10.0	-	-	0.28	0.46	-	-	31.8	0.43
Namibian sedimentary sandstone hosted copper oxide cores residue	T2OCR	12	12.0	-	-	0.26	0.43	-	-	35.3	0.39
Namibian sedimentary sandstone hosted copper oxide cores residue	T2OC2R	12	12.0	-	-	0.26	0.37	-	-	35.3	0.39
Namibian sedimentary sandstone hosted copper upper oxide residue	T2UOR	40	31.0	-	-	0.54	0.38	-0.003	0.75	68.2	0.28
Namibian sedimentary sandstone hosted copper lower oxide residue	T2LOXR	12	18.0	0.24	0.40	-	-	-	-	69.5	0.47
Namibian sedimentary sandstone hosted copper oxide blend head	T2OBH	25	6.5	-	-	0.36	0.50	0.046	1.26	34.7	0.57
Namibian sedimentary sandstone hosted copper oxide blend residue	T2OBR	25	19.0	0.29	0.38	0.44	0.37	-	-	72.7	0.45
Namibian sedimentary sandstone hosted copper oxide blend residue	T3OBR	50	17.0	-	-	0.32	0.34	-0.001	0.44	76.1	0.53
Namibian sedimentary sandstone hosted copper oxide blend residue	T3OB1R	40	15.0	0.22	0.35	0.32	0.38	0.003	0.31	65.3	0.48
Namibian sedimentary sandstone hosted copper oxide blend residue	T3OB2R	50	25.0	0.19	0.37	0.36	0.39	0.058	4.57	65.4	0.33
Namibian sedimentary sandstone hosted copper transition head	T2TRH	12	15.0	-	-	0.15	0.44	-0.383	12.1	25.6	0.22
Namibian sedimentary sandstone hosted copper transition head	T3TRH	20	1.5	-	-	0.18	0.44	0.086	3.26	27.9	0.96
Namibian sedimentary sandstone hosted copper transition head	T4TRH	22	12.5	0.13	0.40	0.28	0.40	-	-	33.1	0.34
Namibian sedimentary sandstone hosted copper transition residue	T2TRR	12	12.0	0.17	0.34	0.22	0.35	-	-	31.2	0.39
Namibian sedimentary sandstone hosted copper transition residue	T3TRR	20	8.0	0.13	0.33	0.26	0.34	-0.114	5.54	36.1	0.53
Namibian sedimentary sandstone hosted copper transition residue	T4TRR	22	20.4	0.18	0.37	0.24	0.35	-	-	42.8	0.24
Namibian sedimentary sandstone hosted copper sulphide transition blend head	T1STRH	12	15.0	-	-	0.17	0.46	0.075	5.98	23.8	0.19
Namibian sedimentary sandstone hosted copper sulphide transition blend head	T2STRBH	12	8.0	-	-	0.16	0.45	-0.176	8.98	26.1	0.45
Namibian sedimentary sandstone hosted copper sulphide transition blend head	T2STRB2H	12	11.0	-	-	0.16	0.43	-0.229	9.13	30.9	0.42
Namibian sedimentary sandstone hosted copper sulphide transition blend head	T2STRB3H	12	6.0	-	-	0.20	0.45	0.049	6.30	21.6	0.47
Namibian sedimentary sandstone hosted copper sulphide transition blend residue	T2STRB3R	12	12.0	0.18	0.30	0.22	0.34	-	-	32.8	0.39
Namibian sedimentary sandstone hosted copper sulphide transition blend residue	T2STRR	12	13.0	0.18	0.30	0.21	0.33	-	-	35.2	0.39
Namibian sedimentary sandstone hosted copper sulphide transition blend residue	T2STRB2R	12	13.0	0.18	0.31	0.25	0.38	-	-	35.9	0.40
Namibian sedimentary sandstone hosted copper oxide transition blend head	T2OTRH	12	6.0	-	-	0.30	0.46	0.133	3.42	35.2	0.62
Namibian sedimentary sandstone hosted copper oxide transition blend head	T3OTRH	25	3.0	-	-	0.26	0.42	0.024	4.35	28.0	0.79
Namibian sedimentary sandstone hosted copper oxide transition blend residue	T3OTRR	20	10.0	0.17	0.34	0.28	0.39	-0.102	4.87	40.6	0.50
Namibian sedimentary sandstone hosted copper oxide transition blend residue	T2OTRR	12	14.0	0.22	0.38	0.43	0.36	0.219	0.59	52.0	0.46
Namibian sedimentary sandstone hosted copper sulphide residue	T2SR	12	11.0	0.16	0.35	0.21	0.36	-	-	29.8	0.43
Zambian sedimentary hosted copper oxide head	MO1H	25	20.8	0.19	0.45	-	-	-0.088	4.68	66.5	0.42
Zambian sedimentary hosted copper oxide head	MO2H	12.5	20.1	0.21	0.44	-	-	-0.279	8.50	50.0	0.26
Zambian sedimentary hosted copper oxide deslimed residue	MORD	25	9.6	0.20	0.47	-	-	0.042	2.70	13.2	0.45
Zambian sedimentary hosted copper mixed head	MM1H	25	15.0	0.21	0.48	-	-	0.019	2.68	27.9	0.26
Zambian sedimentary hosted copper mixed head	MM2H	12.5	13.8	0.20	0.47	-	-	-0.194	8.72	35.9	0.33
Zambian sedimentary hosted copper mixed residue	MMR	12.5	34.6	0.24	0.39	-	-	-	-	62.1	0.18
Zambian sedimentary hosted copper sulphide head	MS1H	25	7.1	0.14	0.46	-	-	-0.049	4.68	22.5	0.38
Zambian sedimentary hosted copper sulphide head	MS2H	12.5	11.7	0.17	0.42	-	-	-0.211	8.98	34.9	0.35
Zambian sedimentary hosted copper sulphide residue	MS2R	12.5	24.4	0.20	0.59	-	-	-	-	51.1	0.24
Zambian sedimentary hosted copper stockpile deslimed head	MSTHD	40	0.0	0.24	0.48	-	-	-0.012	1.35	203	1.26
Zambian sedimentary hosted copper stockpile deslimed residue	MSTRD	40	0.0	0.18	0.44	-	-	-0.017	2.04	80.2	0.95

APPENDIX B

Table B. List of samples used in hydrodynamic column tests (Part II)

Sample	Code	Topsize mm	θ_s m^3/m^3	θ_{aep} m^3/m^3	θ_{max} m^3/m^3	θ_r m^3/m^3	K_s cm/s	K_g cm/s	n_p	m
Chilean copper porphory quartz sericite head	QS1H	12.5	0.46	0.26	0.31	0.12	0.28	0.25	3.00	0.90
Chilean copper porphyry quartz sericite head	QS2H	12.5	0.39	0.24	0.26	0.13	0.14	0.14	2.20	1.05
Chilean copper porphyry quartz sericite residue	QS1R	12.5	0.51	0.25	0.24	0.10	0.28	0.08	6.00	0.60
Chilean copper porphyry quartz sericite residue	QS2R	12.5	0.39	0.28	0.28	0.15	0.14	0.14	4.00	0.80
Chilean copper porphyry (BC) head	BC1H	12.5	0.50	0.35	0.33	0.12	0.11	0.28	1.70	1.24
Chilean copper porphyry (BC) head	BC2H	12.5	0.43	0.31	0.29	0.12	0.11	0.22	2.70	0.91
Chilean copper porphyry (BC) residue	BC1R	12.5	0.44	0.31	0.33	0.15	0.11	0.14	5.00	0.68
Chilean copper porphyry (BC) residue	BC2R	12.5	0.42	0.30	0.34	0.19	0.03	0.05	8.00	0.53
Chilean copper porphyry (BC) residue	BC3R	12.5	0.38	0.27	0.28	0.20	0.11	0.03	6.00	0.60
Chilean copper / gold porphyry oxide argillic residue	OA1R	20	0.41	0.26	0.29	0.14	0.26	0.06	3.80	0.80
Chilean copper / gold porphyry oxide argillic residue	OA2R	25	0.47	0.28	0.35	0.10	0.32	0.14	2.40	1.00
Chilean copper / gold porphyry supergene quartz sericite residue	SQS1R	20	0.43	0.27	0.29	0.16	0.28	0.14	4.10	0.77
Chilean copper / gold porphyry supergene quartz sericite residue	SQS2R	25	0.43	0.29	0.35	0.16	0.33	0.14	2.00	1.10
Chilean copper / gold porphyry mixed oxide supergene argilic quartz sericite residue	OSAQSR	25	0.45	0.29	0.29	0.16	0.26	0.11	3.80	0.80
Chilean copper / gold porphyry mixed supergene quartz sericite P residue	SQSP1R	25	0.44	0.25	0.25	0.13	0.29	0.14	3.50	0.80
Chilean copper / gold porphyry mixed supergene quartz sericite P residue	SQSP2R	20	0.44	0.27	0.27	0.18	0.29	0.14	5.00	0.70
Chilean copper / gold porphyry supergene phyllic alteration residue	SPAR	20	0.43	0.23	0.23	0.13	0.23	0.13	3.80	0.80
Congolese sedimentary dolomite hosted copper oxide (C3) head	KC1H	25	0.40	0.23	0.28	0.13	0.20	0.17	2.70	1.00
Congolese sedimentary dolomite hosted copper oxide (C1) deslimed residue	KC1RD	25	0.48	0.20	0.18	0.12	0.17	0.14	5.00	0.70
Congolese sedimentary dolomite hosted copper oxide (C2) head	KC2H	25	0.41	0.20	0.23	0.11	0.24	0.14	2.50	1.00
Congolese sedimentary dolomite hosted copper oxide (C2) deslimed residue	KC2RS	25	0.46	0.16	0.14	0.07	0.18	0.11	7.00	0.55
Congolese sedimentary dolomite hosted copper oxide (C3) deslimed residue	KC3RD	25	0.40	0.19	0.29	0.13	0.14	0.06	3.50	0.80
Congolese sedimentary dolomite hosted copper oxide (CC) deslimed residue	KCCRD	25	0.47	0.29	0.27	0.13	0.22	0.11	3.50	0.80
Congolese sedimentary stratified hosted copper oxide (N1) head	KN1H	25	0.45	0.22	0.35	0.11	0.21	0.56	1.50	1.35
Congolese sedimentary dolomite hosted heavy media separation floats (C1) head	KHMS1H	25	0.38	0.50	0.38	0.15	0.17	0.18	2.20	0.94
Congolese sedimentary dolomite hosted heavy media separation floats (C2) head	KHMS2H	25	0.37	#N/A	0.37	0.15	0.13	#N/A	2.00	1.74
Congolese sedimentary dolomite hosted heavy media separation floats (C5) residue	KHMS5R	25	0.36	0.36	0.36	0.15	0.17	0.04	4.00	0.76
Congolese sedimentary dolomite hosted heavy media separation floats (C6) residue	KHMS6R	25	0.37	0.25	0.36	0.18	0.09	0.07	2.00	1.15
Spanish vein-type uranium ore (R2C6) residue	RP2C6R	40	0.39	0.15	0.22	0.09	0.40	0.03	5.00	0.70
Spanish vein-type uranium ore (R2C7) residue	RP2C7R	40	0.36	0.23	0.23	0.14	0.13	0.08	8.00	0.55
Spanish vein-type uranium ore (R3C9) residue	RP3C9R	40	0.40	0.24	0.27	0.16	0.40	0.08	4.00	0.80
Spanish vein-type uranium ore (R3C10) residue	RP3C10R	40	0.35	0.23	0.27	0.15	0.20	0.06	4.00	0.80

Table B (Continued). List of samples used in hydrodynamic column tests (Part II)

Sample	Code	Topsize mm	θ_s m^3/m^3	θ_{aep} m^3/m^3	θ_{max} m^3/m^3	θ_r m^3/m^3	K_s cm/s	K_g cm/s	n_p	m
Namibian sedimentary sandstone hosted copper lower oxide residue	T2LOXR	12	0.40	0.30	0.38	0.24	0.04	0.01	2.00	1.15
Namibian sedimentary sandstone hosted copper oxide blend residue	T2OBR	25	0.38	#N/A	0.38	0.29	0.02	#N/A	4.00	0.67
Namibian sedimentary sandstone hosted copper oxide blend residue	T3OB1R	40	0.35	#N/A	0.32	0.22	0.02	#N/A	1.50	1.40
Namibian sedimentary sandstone hosted copper oxide blend residue	T3OB2R	50	0.37	0.25	0.29	0.19	0.06	0.01	6.00	0.65
Namibian sedimentary sandstone hosted copper transition head	T4TRH	22	0.40	0.24	0.30	0.13	0.16	0.05	6.00	0.60
Namibian sedimentary sandstone hosted copper transition residue	T2TRR	12	0.34	0.21	0.29	0.17	0.25	0.08	1.80	1.20
Namibian sedimentary sandstone hosted copper transition residue	T3TRR	20	0.33	0.22	0.24	0.13	0.40	0.06	10.00	0.48
Namibian sedimentary sandstone hosted copper transition residue	T4TRR	22	0.37	0.26	0.31	0.18	0.25	0.05	4.00	0.76
Namibian sedimentary sandstone hosted copper sulphide transition blend residue	T2STRB3R	12	0.30	0.22	0.23	0.18	0.40	0.04	11.00	0.45
Namibian sedimentary sandstone hosted copper sulphide transition blend residue	T2STRR	12	0.30	0.21	0.24	0.18	0.06	0.01	5.00	0.70
Namibian sedimentary sandstone hosted copper sulphide transition blend residue	T2STRB2R	12	0.31	0.22	0.24	0.18	0.05	0.00	3.50	0.85
Namibian sedimentary sandstone hosted copper oxide transition blend residue	T3OTRR	20	0.34	0.22	0.34	0.17	0.09	0.00	2.31	1.00
Namibian sedimentary sandstone hosted copper oxide transition blend residue	T2OTRR	12	0.38	0.29	0.36	0.22	0.07	0.01	1.80	1.20
Namibian sedimentary sandstone hosted copper sulphide residue	T2SR	12	0.35	0.23	0.27	0.16	0.30	0.03	3.00	0.86
Zambian sedimentary hosted copper oxide head	MO1H	25	0.45	0.35	0.38	0.19	0.06	0.03	11.00	0.45
Zambian sedimentary hosted copper oxide head	MO2H	12.5	0.44	0.30	0.41	0.21	0.04	0.02	11.00	0.50
Zambian sedimentary hosted copper oxide deslimed residue	MORD	25	0.47	0.33	0.39	0.20	0.03	0.01	8.00	0.50
Zambian sedimentary hosted copper mixed head	MM1H	25	0.48	0.34	0.41	0.21	0.16	0.17	3.50	0.80
Zambian sedimentary hosted copper mixed head	MM2H	12.5	0.47	0.35	0.44	0.20	0.07	0.14	11.00	0.50
Zambian sedimentary hosted copper mixed residue	MMR	12.5	0.39	0.34	0.39	0.24	0.12	0.02	1.10	0.75
Zambian sedimentary hosted copper sulphide head	MS1H	25	0.46	0.38	0.38	0.14	0.13	0.12	11.00	0.45
Zambian sedimentary hosted copper sulphide head	MS2H	12.5	0.42	0.31	0.39	0.17	0.07	0.04	7.00	0.55
Zambian sedimentary hosted copper sulphide residue	MS2R	12.5	0.41	0.28	0.31	0.20	0.18	0.07	9.00	0.50
Zambian sedimentary hosted copper stockpile deslimed head	MSTHD	40	0.48	0.40	0.48	0.24	0.03	0.00	5.00	0.65
Zambian sedimentary hosted copper stockpile deslimed residue	MSTRD	40	0.44	0.39	0.44	0.18	0.03	0.01	2.57	1.00
Copper porphyry coarse flotation tails	FTH	1.70	0.49	0.25	0.49	0.18	0.06	0.01	3.70	0.80
Copper porphyry coarse flotation tails	FTT1-5	1.70	0.45	0.22	0.44	0.17	0.03	0.00	2.60	1.00
Chilean copper porphyry	MO1	6	0.47	0.30	0.29	0.12	0.14	0.14	4.00	0.78
Chilean copper porphyry	MO2	20	0.47	0.21	0.24	0.07	0.15	0.17	3.00	0.88
Chilean copper porphyry	MO3	6	0.48	0.23	0.32	0.08	0.13	0.28	2.00	1.10
Namibian uranium ore	EB	9	0.36	0.33	0.33	0.15	0.02	0.01	3.20	0.85
Namibian copper porphyry	H-2.36	2.36	0.34	#N/A	0.32	0.20	0.01	#N/A	5.00	0.65
Namibian copper porphyry	H-3.35	3.35	0.45	0.30	0.34	0.12	0.07	0.01	7.00	0.60
Namibian copper porphyry	H-4.75	4.75	0.43	0.30	0.38	0.11	0.07	0.08	4.00	0.78

APPENDIX C

Table C.1. Summary of compression tests (in order of increasing -2 mm content)(Part III)

Sample Description	Code	Cc	Target Height	Topsize	-4.75 mm	-50+4.75 mm	-4.75+2 mm	-2+0.075 mm	-2 mm	-0.075 mm
			(m)	(mm)	(%)	(%)	(%)	(%)	(%)	(%)
Spanish vein-type uranium ore (A2) head	A2H	0.084	14.0	50	7	93	3	3	4	1
Congolese sedimentary dolomite hosted copper oxide (C2) deslimed residue	KC2RS	0.064	23.5	25	14	86	6	5	8	3
Congolese sedimentary stratified hosted copper oxide (N1) deslimed head	KN1HD	0.067	18.1	25	19	81	8	12	12	0
South American copper porphyry	MO2	0.030	7.2	20	21	79	8	10	12	2
Congolese sedimentary dolomite hosted copper oxide (C1) deslimed residue	KC1RD	0.067	23.2	25	20	80	7	8	13	5
Congolese sedimentary stratified hosted copper oxide (N1) deslimed residue	KN1RD	0.079	17.8	25	20	80	8	10	13	2
Congolese sedimentary dolomite hosted copper oxide (C2) head	KC2H	0.101	16.7	25	21	79	8	10	13	4
Congolese sedimentary dolomite hosted copper oxide (C1) deslimed head	KC1HD	0.087	17.0	25	24	76	10	14	14	0
Congolese sedimentary dolomite hosted copper oxide (C3) deslimed head	KC3HD	0.118	16.6	25	24	76	9	14	15	1
Spanish vein-type uranium ore (RC2) head	RC2H	0.089	7.3	50	23	77	7	9	16	7
Spanish vein-type uranium ore (A2C18) residue	A2C18R	0.095	9.5	25	32	68	16	10	16	6
Congolese sedimentary dolomite hosted copper oxide (CC) head	KCCHU	0.118	17.2	25	27	73	11	13	16	3
Congolese sedimentary dolomite hosted copper oxide (CC) deslimed head	KCCHD	0.068	17.6	25	30	70	13	13	18	4
Congolese sedimenatry dolomite hosted copper oxide (KL2) deslimed head	KL2HD	0.090	17.1	25	28	72	10	18	18	0
Congolese sedimentary dolomite hosted copper oxide (CC) residue scrubbed	KCCRD	0.034	6.7	25	35	65	15	17	20	3
Congolese sedimentary dolomite hosted copper oxide (CC) residue scrubbed	KCCRD	0.039	20.5	25	35	65	15	17	20	3
Congolese sedimentary dolomite hosted copper oxide (KL1) deslimed head	KL1HD	0.137	16.5	25	31	69	11	20	20	0
West African shear hosted orogenic gold sulphide ore with pyrite occurrence	BOBS	0.054	6.8	12.5	37	63	16	19	21	2
Spanish vein-type uranium ore (A2) head	A22H	0.093	12.0	25	40	60	19	11	21	11
Spanish vein-type uranium ore (A3) head	A33H	0.169	12.1	25	22	59	19	12	22	10
Spanish vein-type uranium ore (ZD1) residue	ZD1R	0.119	6.2	50	38	62	13	7	25	18
Zambian sedimentary hosted copper sulphide head	MS1H	0.135	6.3	25	35	65	10	18	25	7
Congolese sedimentary stratified hosted copper oxide (N2&4) deslimed head	KN24HD	0.130	16.6	25	39	61	13	26	26	0
Congolese sedimentary stratified hosted copper oxide (N2&4) deslimed residue	KN24RD	0.116	15.8	25	40	60	13	23	27	4
Spanish vein-type uranium ore (ZC1) residue	ZD1R	0.122	6.4	50	48	52	20	11	28	17
Spanish vein-type uranium ore (ZD2) residue	ZD2R	0.082	6.5	25	48	52	20	8	28	20
Chilean copper porphyry (BC) head	BC1H	0.074	7.3	12.5	45	55	17	22	28	6
Chilean copper porphyry (BC) head	BC2H	0.100	17.8	12.5	45	55	17	22	28	6
Namibian sedimentary sandstone hosted copper sulphide transition blend head	T1STRH	0.120	4.2	12	47	53	18	14	29	15
Namibian sedimentary sandstone hosted copper sulphide transition blend head	T2STRB3H	0.176	4.7	12	49	51	20	23	29	6
Namibian sedimentary sandstone hosted copper transition head	T3TRH	0.146	6.9	20	39	61	10	28	29	2
Congolese sedimentary dolomite hosted copper oxide (KL1) head	KL1H	0.178	16.1	25	42	58	12	20	30	11

Table C.1. Summary of compression tests (continued)(Part III)

Sample Description	Code	Cc	Target Height	Topsize	-4.75 mm	-50+4.75 mm	-4.75+2 mm	-2+0.075 mm	-2 mm	-0.075 mm
			(m)	(mm)	(%)	(%)	(%)	(%)	(%)	(%)
Namibian sedimentary sandstone hosted copper oxide head	T3OH	0.166	6.1	50	34	66	3	24	31	7
Namibian sedimentary sandstone hosted copper oxide head	T3OH	0.163	5.7	50	34	66	3	24	31	7
Namibian sedimentary sandstone hosted copper oxide transition blend head	T3OTRH	0.184	6.7	25	41	59	10	28	31	3
South American copper porphyry	POR1D	0.100	7.2	6.7	73	27	42	31	31	0
Spanish vein-type uranium ore (ZC2) residue	ZC2R	0.088	6.6	25	55	45	23	16	32	16
Chilean copper / gold porphyry mixed supergene quartz sericite P residue	SQSP1R	0.109	8.7	25	43	57	11	21	32	11
Namibian sedimentary sandstone hosted copper transition head	T2TRH	0.168	7.0	12	59	41	26	18	33	15
Namibian sedimentary sandstone hosted copper sulphide transition blend head	T2STRBH	0.136	7.0	12	56	44	21	27	35	8
Chilean copper / gold porphyry oxide argillic residue	OA2R	0.117	9.2	25	50	50	15	18	35	17
Chilean copper / gold porphyry supergene quartz sericite residue	SQS2R	0.187	8.3	25	55	45	20	25	35	10
Namibian sedimentary sandstone hosted copper sulphide residue	T2SR	0.134	17.8	12	56	44	20	25	36	11
Namibian sedimentary sandstone hosted copper sulphide residue	T2SR	0.097	6.3	12	56	44	20	25	36	11
South American copper porphyry	POR1	0.140	7.0	6.7	75	25	39	31	36	5
Congolese sedimentary dolomite hosted copper oxide HMS floats head	KHMS1H	0.146	6.3	25	50	50	14	29	36	7
Congolese sedimentary dolomite hosted copper oxide HMS floats head	KHMS1H	0.139	14.6	25	50	50	14	29	36	7
Chilean copper / gold porphyry mixed oxide supergene argillic quartz sericite residue	OSAQSR	0.112	8.4	25	48	52	11	20	37	17
Namibian sedimentary sandstone hosted copper oxide blend head	T3OTRHH	0.137	6.3	40	41	59	4	30	37	7
Namibian sedimentary sandstone hosted copper oxide blend head	T3OTRHH	0.152	6.2	40	41	59	4	30	37	7
Namibian sedimentary sandstone hosted copper oxide blend head	T3OTRHH	0.167	3.8	40	41	59	4	30	37	7
Namibian sedimentary sandstone hosted copper transition residue	T2TRR	0.095	6.2	12	50	50	13	25	37	12
Namibian sedimentary sandstone hosted copper transition residue	T2TRR	0.143	17.6	12	50	50	13	25	37	12
Namibian sedimentary sandstone hosted copper oxide head	T2UOH	0.216	2.4	40	42	58	4	23	38	15
Namibian sedimentary sandstone hosted copper oxide cores head	T2OCH	0.165	2.3	12	58	42	20	28	38	10
Chilean copper / gold porphyry mixed supergene quartz sericite P residue	SQSP2R	0.203	8.2	20	48	52	10	25	38	13
Spanish vein-type uranium ore (ZA1) residue	ZA1R	0.127	6.1	50	50	50	11	11	39	28
Namibian sedimentary sandstone hosted copper sulphide transition blend residue	T2STRB3R	0.139	6.1	12	56	44	17	27	39	12
Namibian sedimentary sandstone hosted copper sulphide transition blend residue	T2STRB3R	0.141	17.4	12	56	44	17	27	39	12
Chilean copper / gold porphyry supergene quartz sericite residue	SQS1R	0.148	8.5	20	53	47	13	23	40	17
Zambian sedimentary hosted copper mixed head	MM2H	0.231	6.2	12.5	58	42	18	26	40	14
Zambian sedimentary hosted copper sulphide head	MS2H	0.232	6.0	12.5	58	42	18	28	40	12
Namibian sedimentary sandstone hosted copper sulphide transition blend head	T2STRB2H	0.181	6.8	12	61	39	20	30	41	11

Table C.1. Summary of compression tests (continued)(Part III)

Sample Description	Code	Cc	Target Height	Topsize	-4.75 mm	-50+4.75 mm	-4.75+2 mm	-2+0.075 mm	-2 mm	-0.075 mm
			(m)	(mm)	(%)	(%)	(%)	(%)	(%)	(%)
Chilean copper / gold porphyry oxide argillic residue	OA1R	0.139	8.7	20	57	43	14	30	43	13
Namibian sedimentary sandstone hosted copper sulphide transition blend residue	T2STRR	0.153	6.1	12	62	38	19	30	43	13
Namibian sedimentary sandstone hosted copper sulphide transition blend residue	T2STRR	0.175	17.4	12	62	38	19	30	43	13
Congolese sedimentary (dolomite) hosted heavy media separation floats (6) residue	KHMS6R	0.159	15.1	25	63	37	20	30	43	14
Spanish vein-type uranium ore (ZA2) residue	ZA2R	0.122	6.3	25	58	42	15	12	43	31
Namibian sedimentary sandstone hosted copper sulphide transition blend residue	T2STRB2R	0.173	17.1	12	65	35	21	31	44	13
Namibian sedimentary sandstone hosted copper sulphide transition blend residue	T2STRB2R	0.158	6.0	12	65	35	21	31	44	13
Namibian sedimentary sandstone hosted copper oxide cores residue	T2OCR	0.186	6.1	12	59	41	15	32	44	12
Namibian sedimentary sandstone hosted copper oxide cores residue	T2OC2R	0.168	2.2	12	59	41	15	32	44	12
Congolese sedimentary (dolomite) hosted heavy media separation floats (5) residue	KHMS5R	0.154	18.1	25	62	38	17	27	45	18
Namibian sedimentary sandstone hosted copper lower oxide head	T2LOXH	0.158	2.6	25	50	50	4	31	46	15
Namibian sedimentary sandstone hosted copper transition residue	T3TRR	0.154	6.3	20	57	43	11	38	46	8
Namibian sedimentary sandstone hosted copper transition residue	T3TRR	0.202	17.6	20	57	43	11	38	46	8
Namibian sedimentary sandstone hosted copper oxide transition blend head	T2OTRH	0.145	2.5	12	59	41	13	40	46	6
Namibian sedimentary sandstone hosted copper oxide transition blend head	T2OTRH	0.228	4.9	12	59	41	13	40	46	6
Namibian sedimentary sandstone hosted copper transition residue	T4TRR	0.082	5.7	25	60	40	9	31	51	20
Namibian sedimentary sandstone hosted copper transition residue	T4TRR	0.075	5.6	25	60	40	9	31	51	20
Zambian sedimentary hosted copper oxide head	MOH	0.241	6.0	25	58	42	6	31	52	21
Namibian sedimentary sandstone hosted copper oxide transition blend residue	T3OTRR	0.188	17.2	20	63	37	11	42	52	10
Namibian sedimentary sandstone hosted copper oxide transition blend residue	T3OTRR	0.145	6.1	20	63	37	11	42	52	10
Zambian sedimentary hosted copper stockpile deslimed residue	MSTHD2	0.150	6.4	40	58	42	6	52	52	0
West African shear hosted orogenic gold oxide ore with pyrite occurrence	BOBO	0.320	6.2	12.5	66	34	13	35	53	18
Zambian sedimentary hosted copper sulphide residue	MS2R	0.246	5.9	12.5	70	30	13	33	57	24
Zambian sedimentary hosted copper oxide head	MO2H	0.243	5.9	12.5	68	32	10	38	58	20
Zambian sedimentary hosted copper stockpile deslimed head	MSTHD1	0.230	6.6	40	72	28	4	68	68	0
Zambian sedimentary hosted copper mixed residue	MMR	0.265	5.7	12.5	78	22	8	35	70	35
Namibian sedimentary sandstone hosted copper upper oxide	T2XOX	0.300	1.9	40	79	21	3	45	76	31
Zambian sedimentary hosted copper stockpile head	MSTH	0.270	4.7	40	85	15	2	34	83	49
Namibian sedimentary sandstone hosted copper lower oxide residue	T2LOXR	0.353	4.2	12	95	5	4	73	91	18
Namibian sedimentary sandstone hosted copper oxide blend residue	T2OBR	0.340	5.5	25	95	5	2	74	93	19
Namibian sedimentary sandstone hosted copper oxide blend residue	T2OBR	0.338	5.5	25	95	5	2	74	93	19
Namibian sedimentary sandstone hosted copper oxide blend residue	T2OBR	0.314	3.8	25	95	5	2	74	93	19
Namibian Cu porphyry	H-2.36	0.211	5.8	2.36	100	0	6	77	94	17

Table C.2. Summary of hydrodynamic column tests (arranged in order of increasing -4.75 mm content)(Part III)

Sample Description	Code	Topsize	Θaep	Θr	Θ steady state	Θs-Θmax	Θmax-Θr	1-Θs
		(mm)	(m^3/m^3)	(m^3/m^3)	(m^3/m^3)	(m^3/m^3)	(m^3/m^3)	(m^3/m^3)
Congolese sedimentary dolomite hosted copper oxide (C2) deslimed residue	KC2RS	25	0.16	0.07	0.10	0.32	0.07	0.54
Chilean copper porphory quartz sericite head	QS1H	12.5	0.26	0.12	0.13	0.15	0.19	0.54
Chilean copper porphyry quartz sericite head	QS2H	12.5	0.24	0.13	0.14	0.13	0.13	0.61
Congolese sedimentary dolomite hosted copper oxide (C2) deslimed head	KC2HD	25	0.16	0.07	0.10	0.32	0.07	0.54
Congolese sedimentary dolomite hosted copper oxide (C1) deslimed residue	KC1RD	25	0.20	0.12	0.13	0.29	0.07	0.52
Congolese sedimentary dolomite hosted copper oxide (C2) head	KC2H	25	0.20	0.11	0.12	0.19	0.12	0.59
South American copper porphyry	MO2	25	0.21	0.07	0.11	0.23	0.17	0.53
Congolese sedimentary stratified hosted copper oxide (N1) head	KN1H	25	0.22	0.11	0.13	0.10	0.24	0.55
Congolese sedimentary dolomite hosted copper oxide (C3) head	KC1H	25	0.23	0.13	0.14	0.12	0.15	0.60
Chilean copper porphyry quartz sericite residue	QS1R	12.5	0.25	0.10	0.12	0.27	0.14	0.49
Zambian sedimentary hosted copper mixed head	MM1H	25	0.34	0.21	0.26	0.07	0.20	0.52
Congolese sedimentary dolomite hosted copper oxide (CC) deslimed residue	KCCRD	25	0.29	0.13	0.14	0.21	0.14	0.53
Zambian sedimentary hosted copper sulphide head	MS1H	25	0.38	0.14	0.21	0.08	0.24	0.54
Congolese sedimentary dolomite hosted copper oxide (C3) deslimed residue	KC3RD	25	0.19	0.13	0.17	0.11	0.17	0.60
Chilean copper porphyry quartz sericite residue	QS2R	12.5	0.28	0.15	0.17	0.11	0.13	0.61
Chilean copper / gold porphyry mixed supergene quartz sericite P residue	SQSP1R	25	0.25	0.13	0.16	0.19	0.12	0.56
Chilean copper porphyry (BC) head	BC1H	12.5	0.35	0.12	0.13	0.17	0.21	0.50
Chilean copper porphyry (BC) head	BC2H	12.5	0.31	0.12	0.13	0.14	0.17	0.57
Spanish vein-type uranium ore (R3C9) residue	RP3C9R	40	0.24	0.16	0.19	0.12	0.12	0.60
Spanish vein-type uranium ore (R2C7) residue	RP2C7R	40	0.23	0.14	0.17	0.13	0.09	0.64
Spanish vein-type uranium ore (R3C10) residue	RP3C10R	40	0.23	0.15	0.19	0.08	0.12	0.65
Spanish vein-type uranium ore (R2C6) residue	RP2C6R	40	0.15	0.09	0.13	0.17	0.13	0.61
Chilean copper / gold porphyry mixed oxide supergene argillic quartz sericite residue	OSAQSR	25	0.29	0.16	0.20	0.16	0.13	0.55
Chilean copper / gold porphyry mixed supergene quartz sericite P residue	SQSP2R	20	0.27	0.18	0.20	0.17	0.09	0.56
Congolese sedimentary dolomite hosted heavy media separation floats (C1) head	KHMS1H	25	0.50	0.15	0.16	0	0.23	0.62
Congolese sedimentary dolomite hosted heavy media separation floats (C2) head	KHMS2H	25	-	0.15	0.15	0	0.22	0.63
Chilean copper / gold porphyry supergene phyllic alteration residue	SPAR	20	0.23	0.13	0.15	0.20	0.10	0.57
Chilean copper / gold porphyry oxide argillic residue	OA2R	25	0.28	0.10	0.14	0.11	0.25	0.53
Namibian sedimentary sandstone hosted copper transition residue	T2TRR	12	0.21	0.17	0.18	0.05	0.13	0.66
Namibian sedimentary sandstone hosted copper transition head	T4TRH	22	0.24	0.13	0.19	0.10	0.17	0.60
Chilean copper porphyry (BC) residue	BC1R	12.5	0.31	0.15	0.21	0.11	0.18	0.57
Chilean copper porphyry (BC) residue	BC2R	12.5	0.30	0.19	0.27	0.09	0.15	0.58
Chilean copper porphyry (BC) residue	BC3R	12.5	0.27	0.20	0.21	0.10	0.09	0.62
Chilean copper / gold porphyry supergene quartz sericite residue	SQS1R	20	0.27	0.16	0.20	0.14	0.13	0.57
Chilean copper / gold porphyry supergene quartz sericite residue	SQS2R	25	0.29	0.16	0.18	0.07	0.20	0.57
Zambian sedimentary hosted copper oxide deslimed residue	MORD	25	0.33	0.20	0.27	0.08	0.19	0.53
Namibian sedimentary sandstone hosted copper sulphide transition blend residue	T2STRB3R	12	0.22	0.18	0.19	0.08	0.05	0.70

Table C.2. Summary of hydrodynamic column tests (continued)(Part III)

Sample Description	Code	Topsize	Θaep	Θr	Θ steady state	Θs-Θmax	Θmax-Θr	1-Θs
		(mm)	(m^3/m^3)	(m^3/m^3)	(m^3/m^3)	(m^3/m^3)	(m^3/m^3)	(m^3/m^3)
Namibian sedimentary sandstone hosted copper sulphide residue	T2SR	12	0.23	0.16	0.17	0.08	0.11	0.65
Namibian sedimentary sandstone hosted copper transition residue	T3TRR	20	0.22	0.13	0.16	0.09	0.11	0.67
Chilean copper / gold porphyry oxide argillic residue	OA1R	20	0.26	0.14	0.17	0.12	0.15	0.59
Zambian sedimentary hosted copper oxide head	MO1H	25	0.35	0.19	0.28	0.07	0.19	0.55
Zambian sedimentary hosted copper mixed head	MM2H	12.5	0.35	0.20	0.24	0.03	0.24	0.53
Zambian sedimentary hosted copper sulphide head	MS2H	12.5	0.31	0.17	0.22	0.03	0.23	0.58
Zambian sedimentary hosted copper stockpile deslimed residue	MSTHD2	40	0.41	0.18	0.21	0	0.26	0.56
Namibian sedimentary sandstone hosted copper transition residue	T4TRR	22	0.26	0.18	0.21	0.06	0.13	0.63
Congolese sedimentary dolomite hosted heavy media separation floats (C5) residue	KHMS5R	25	0.36	0.15	0.18	0	0.21	0.64
Namibian sedimentary sandstone hosted copper sulphide transition blend residue	T2STRR	12	0.21	0.18	0.19	0.07	0.06	0.70
Congolese sedimentary dolomite hosted heavy media separation floats (C6) residue	KHMS6R	25	0.25	0.18	0.19	0.02	0.18	0.63
Namibian sedimentary sandstone hosted copper oxide transition blend residue	T3OTRR	20	0.22	0.17	0.19	0	0.17	0.66
Namibian sedimentary sandstone hosted copper sulphide transition blend residue	T2STRB2R	12	0.22	0.18	0.19	0.07	0.05	0.69
Zambian sedimentary hosted copper oxide head	MO2H	12.5	0.30	0.21	0.29	0.02	0.20	0.56
Namibian sedimentary sandstone hosted copper oxide transition blend residue	T2OTRR	12	0.29	0.22	0.23	0.02	0.14	0.62
Zambian sedimentary hosted copper sulphide residue	MS2R	12.5	0.28	0.20	0.24	0.10	0.12	0.59
Zambian sedimentary hosted copper stockpile deslimed head	MSTHD1	40	0.48	0.24	0.32	0	0.24	0.52
South American porphyry	POR1D	6.7	0.28	0.08	0.14	0.16	0.24	0.52
South American porphyry	POR1	6.7	0.29	0.12	0.17	0.08	0.28	0.53
Namibian sedimentary sandstone hosted copper oxide blend residue	T3OB2R	50	0.25	0.19	0.23	0.08	0.10	0.63
Zambian sedimentary hosted copper mixed residue	MMR	12.5	0.34	0.24	0.29	0	0.16	0.61
Namibian sedimentary sandstone hosted copper oxide blend residue	T3OB1R	40	-	0.19	0.22	0.03	0.13	0.65
South American porphyry	POR2	6.7	0.25	0.08	0.16	0.06	0.21	0.65
South American porphyry	POR2D2	6.7	0.28	0.05	0.12	0.16	0.23	0.57
South American porphyry	POR2D1	6.7	0.32	0.06	0.14	0.10	0.25	0.59
Zambian sedimentary hosted copper stockpile head	MSTH	40	0.41	0.17	0.30	0	0.24	0.59
Zambian sedimentary hosted copper stockpile head	MSCH	40	0.42	0.15	0.30	0	0.27	0.58
Namibian uraniferous alaskite	EB	9	0.33	0.15	0.19	0.02	0.18	0.65
Namibian sedimentary sandstone hosted copper oxide blend residue	T2OBR	25	-	0.29	0.30	0	0.09	0.62
Namibian sedimentary sandstone hosted copper lower oxide residue	T2LOXR	12	0.30	0.24	0.25	0.02	0.14	0.60
Namibian Cu porphyry	H-4.75	4.75	0.30	0.11	0.21	0.04	0.28	0.57
Namibian Cu porphyry	H-3.35	3.35	0.30	0.12	0.21	0.11	0.22	0.55
Namibian Cu porphyry	H-2.36	2.36	-	0.20	0.26	0.02	0.13	0.66
Deslimed coarse sand tails (1a)	FTH	1.7	0.25	0.18	0.25	0	0.31	0.51
Deslimed coarse sand tails (1)	FTT1-5	1.7	0.22	0.17	0.23	0.01	0.28	0.55
Deslimed coarse sand tails (2)	FTT1-5R	1.7	0.24	0.17	0.25	0.02	0.29	0.52
Deslimed coarse sand tails (3)	FTT4	1.7	0.21	0.17	0.20	0.04	0.24	0.55
Deslimed coarse sand tails (4)	FTT6	2.36	0.22	0.17	0.21	0.06	0.25	0.52
Deslimed coarse sand tails (5)	FTT7	2.36	0.21	0.16	0.20	0.05	0.23	0.55